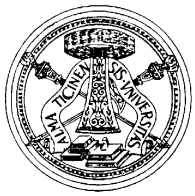

Dottorato di Ricerca in Ingegneria Civile
Graduate School in Civil Engineering
Sede: Facoltà di Ingegneria - Università di Pavia - via Ferrata 1 – 27100 Pavia – Italy

Dottorato di Ricerca in Ingegneria Civile XX Ciclo)

Application of PIV technique to the study of subaqueous debris flows

Ph.D. Thesis

Ing. Matteo Pagliardi

Advisers:
Prof. Paolo Ghilardi
Prof. Anders Elverhøi

Supervisor:
Prof. Mario Gallati

December 2007

Description of the Ph.D. course

Settore: **Field:**	Ingegneria Engineering
Sede Amministrativa non consortile: **Administrative location:**	Università degli Studi di Pavia University of Pavia
Durata del dottorato: **Duration:**	3 anni 3 years
Periodo formativo estero: **Period in external organization:**	come previsto dal regolamento del Dottorato di Ricerca as required by the school by-law
Numero minimo di corsi: **Minimum number of courses:**	6 6

Il dottorato di ricerca in Ingegneria Civile dell'Università degli Studi di Pavia è stato istituito nell'anno accademico 1994/95 (X Ciclo)).

Il corso consente al dottorando di scegliere tra due curricula: idraulico o strutturale. Egli svolge la propria attività di ricerca rispettivamente presso il Dipartimento di Ingegneria Idraulica e Ambientale o quello di Meccanica Strutturale.

Durante i primi due anni sono previsti almeno sei corsi, seguiti da rispettivi esami, che il dottorando è tenuto a sostenere. Il Collegio dei Docenti, composto da professori dei due Dipartimenti, organizza i corsi con lo scopo di fornire allo studente di dottorato opportunità di approfondimento su alcune delle discipline di base per entrambe le componenti, idraulica e strutturale. Corsi e seminari vengono tenuti da docenti di Università nazionali ed estere.

Il Collegio dei Docenti, cui spetta la pianificazione della didattica, si è orientato ad attivare ad anni alterni corsi sui seguenti temi:

- Meccanica dei solidi e dei fluidi;
- Metodi numerici per la meccanica dei solidi e dei fluidi;
- Rischio strutturale e ambientale;
- Metodi sperimentali per la meccanica dei solidi e dei fluidi;
- Intelligenza artificiale;

più corsi specifici di indirizzo.

Al termine dei corsi del primo anno il Collegio dei Docenti assegna al dottorando un tema di ricerca da sviluppare sotto forma di tesina entro la fine del secondo anno; il tema, non necessariamente legato all'argomento della tesi finale, è di norma coerente con il curriculum, scelto dal dottorando (idraulico o strutturale).

All'inizio del secondo anno il dottorando discute con il Coordinatore l'argomento della tesi di dottorato, la cui assegnazione definitiva viene deliberata dal Collegio dei Docenti.

Alla fine di ogni anno i dottorandi devono presentare una relazione particolareggiata (scritta e orale) sull'attività svolta. Sulla base di tale relazione il Collegio dei Docenti, "previa valutazione della assiduità e dell'operosità

dimostrata dall'iscritto", ne propone al Rettore l'esclusione dal corso o il passaggio all'anno successivo.

Il dottorando può svolgere attività di ricerca sia di tipo teorico che sperimentale, grazie ai laboratori di cui entrambi i Dipartimenti dispongono, nonché al Laboratorio Numerico di Ingegneria delle Infrastrutture.

Il “Laboratorio didattico sperimentale” del Dipartimento di Meccanica Strutturale offre:

- una tavola vibrante che consente di effettuare prove dinamiche su prototipi strutturali;
- opportuni sensori e un sistema di acquisizione dati per la misura della risposta strutturale;
- strumentazione per la progettazione di sistemi di controllo attivo e loro verifica sperimentale;
- strumentazione per la caratterizzazione dei materiali, attraverso prove statiche e dinamiche.

Il laboratorio del Dipartimento di Ingegneria Idraulica e Ambientale dispone di:

- un circuito in pressione che consente di effettuare simulazioni di moto vario;
- un tunnel idrodinamico per lo studio di problemi di cavitazione;
- canalette per lo studio delle correnti a pelo libero.

The Graduate School of Civil Engineering at the University of Pavia was established in the Academic Year of 1994/95 (X cycle).

The School allows the student to select one of the four offered curricula: Hidraulics, Environment, Seismics and Structure. Each student develops his research activity either at the Departement of Hidraulics and Environmental Engineering or at the Departement of Structural Mechanics. During the first two years, a minimum of six courses must be selected and their examinations successfully passed. The Faculty, represented by Professors of the two Departements or by internationally recognized scientists, organizes courses so as to provide the student with opportunities to deepen his basic knowledge. Courses and seminars are held by University Professors from all over the country and abroad.

The Faculty starts up courses, in alternate years, on the following subjects:

- solid and fluid mechanics;
- numerical methods for solid and fluid mechanics;
- structural and environmental risk;
- experimental methods for solid and fluid mechanics;
- artificial intelligence and other, more specific courses.

More specific courses are devoted to students curricula.

At the end of each course, for the first year the Faculty assigns the student a research argument to develop, in the form of report, by the end of the second year; the topic, not necessarily on the final doctorate thesis, should be consistent with the curriculum selected by the student. At the beginning of the second year the student discusses with his Coordinator the subject of the thesis and eventually, the Faculty assigns it. At the end of every year, the student has to present a complete report on his research activity, on the basis of which the Faculty proposes his term for the successive year or his admission to the final examination to the Rector. The student is supposed to develop either theoretical or experimental research activities, and therefore has access to the Department Experimental Laboratories, even to the Numerical Laboratory of Infrastructure Engineering.

The Experimental Teaching Laboratory of the Department of Structural Mechanics offers:

- a shaking table which permits one to conduct dynamic tests on structural prototypes;
- sensors and acquiring data system for the structural response measurements;
- instrumentation for the design of active control system and their experimental checks;
- an universal testing machine for material characterization through static and dynamic tests.

The Department of Hidraulics and Environmental Engineering offers:

- a pression circuit simulating various movements;
- a hydrodynamic tunnel studing cavitation problems;
- micro-channels studing free currents.

Recapiti - Addresses

Dipartimento di Meccanica Strutturale
via Ferrata 1 - 27100 Pavia - Italy
Tel. +39.0382.985450 - Fax +39.0382.988422

Dipartimento di Ingegneria Idraulica e Ambientale
via Ferrata 1 - 27100 Pavia - Italy
Tel. +39.0382.985300 - Fax +39.0382.985589

Coordinatore - Coordinator

CASCIATI Fabio - Professore Ordinario (ICAR/08)
Dipartimento di Meccanica Strutturale
via Ferrata 1 - 27100 Pavia – Italy
Tel. +39.0382.985458 - Fax +39.0382.988422
e-mail: fabio@dipmec.unipv.it

Collegio dei Docenti - Teaching staff

CAPODAGLIO Andrea Giuseppe Professore Associato - ICAR/03
CASCIATI Fabio Professore Ordinario - ICAR/08 (Coordinatore)
CAUVIN Aldo Professore Ordinario - ICAR/09*
CIAPONI Carlo Professore Straordinario - ICAR/01
FARAVELLI Lucia Professore Ordinario - ICAR/08
FUGAZZA Mario Professore Associato - ICAR/02
GOBETTI Armando Professore Associato - ICAR/08
MOISELLO Ugo Professore Ordinario - ICAR/02
PAPIRI Sergio Professore Associato - ICAR/02
SALA Roberto Professore Associato - ING - IND/08
MARCELLINI Alberto Dirigente di Ricerca, CNR - Milano

* Deceduto il 30 gennaio 2007

Previous Ph.D. Thesis

Battaini Marco (X Ciclo)	Sistemi strutturali controllati: progettazione e affidabilità
Mariani Claudia (X Ciclo)	Problemi di ottimizzazione per strutture bidimensionali anisotrope
Negri Antonella (X Ciclo)	Stima delle perdite idrologiche nei bacini di drenaggio urbani
Pisano Aurora Angela (XI Ciclo)	Structural System Identification: Advanced Approaches and Applications
Saltalippi Carla (XI Ciclo)	Preannuncio delle piene in tempo reale nei corsi d'acqua naturali
Barbieri Eugenio (XI Ciclo)	Termofluid dynamics and topology optimisation of an active thermal insulation structure
Barbolini Massimiliano (XII Ciclo)	Dense snow avalanche avalanches: computational models, hazard mapping and related uncertainties
Espa Paolo (XII Ciclo)	Moti atmosferici generati da forze di galleggiamento: simulazioni numeriche e studio su modello fisico
Petrini Lorenza (XII Ciclo)	Shape Memory Alloys: Modelling the Martensitic Phase Behaviour for Structural Engineering Exploitation
Podestà Stefano (XIII Ciclo)	Risposta sismica di antichi edifici religiosi in muratura: sviluppo di nuovi modelli per l'analisi di vulnerabilità
Sturla Daniele (XIII Ciclo)	Simulazioni lagrangiane di flussi rapidamente variati nell'approssimazione di acque poco profonde

Marazzi Francesco (XV Ciclo)	Semi-active control of civil structures: implementation aspects
Nascimbene Roberto (XV Ciclo)	Sail Modelling for Maximal Speed Optimum Design
Giudici Massimo (XVI Ciclo)	Progettazione in regime non lineare di strutture in CAP a cavi aderenti e non aderenti
Mutti Matteo (XVI Ciclo)	Stability analysis of stratified three-phase flows in pipes
Petaccia Gabriella (XVI Ciclo)	Propagazione di onde a fronte ripido per rottura di sbarramenti in alvei naturali
Casciati Sara (XVII Ciclo)	Damage Detection and Localization in the Space of the Observed Variables
D'Amico Tiziana (XVI Ciclo)	Ricerca e Sviluppo di Metodologie Diagnostiche per il Recupero di Edifici monumentali: Prove Vibro-acustiche sul Tufo
Domaneschi Marco (XVIII Ciclo)	Structural Control of Cable-stayed and Suspended Bridges
Barco Olga Janet (XVII Ciclo)	Modeling the quantity and quality of storm water runoff using SWMM
Boguniewicz Joanna (XVIII Ciclo)	Integration of monitoring and modelling in the surface water state evaluation process of a sub-Alpine lake watershed
Bornatici Laura (XVIII Ciclo)	L'impiego degli algoritmi generici per la risoluzione dei problemi di progetto di reti di distribuzione idrica
Collivignarelli Maria Cristina (XVIII Ciclo)	Trattamento di rifiuti liquidi mediante processi biologici aerobici termofili e mesofili e processi avanzati di ossidazione chimica in diversa sequenza

Ráduly Botond (XVIII Ciclo)	Artificial neural network applications in urban water quality modeling
Antoci Carla (XVIII Ciclo)	Simulazione numerica dell'interazione fluido-struttura con la tecnica SPH
Federica Cappabianca (XVIII Ciclo)	La valutazione del rischio valanghivo attraverso la modellazione dinamica
Gazzola Elisa (XVIII Ciclo)	Applicazione di processi biologici anaerobici al trattamento di acque reflue e fanghi di depurazione: aspetti tecnici ed energetici
Giuliano Fabio (XIX Ciclo)	Performance based design and ctructural control for cable suspension bridges
Callegari Arianna (XVIII Ciclo)	Applicazione di tecnologie di monitoraggio on-line per la gestione dei processi di trattamento reflui
Maranca Federica (XVIII Ciclo)	Valutazione del Ciclo) di vita (LCA): confronto tra sistemi di trasporto gas via gasdotto
Zanaboni Sabrina (XIX Ciclo)	Pre-trattamento di rifiuti liquidi industriali mediante ossidazione ad umido
Falappi Stefano (XIX Ciclo)	Simulazioni numeriche di flussi di fluidi viscosi e materiali granulari con la tecnica SHP"

Index

Abstract

Turbidity currents and subaqueous debris flows are one of the main processes of sediment transport on the Earth. They are responsible for the transfer of sediment from the continents to the oceans and the infilling of large sediment basins. They are therefore major geological phenomena, with a significant impact on a variety of issues.

Interest in this field has increased significantly in more recent years in conjunction with advances in seafloor and sub-seabed mapping augmented by further studies of ancient deposits on land. Due to their inaccessibility, observation of these types of deposits is not sufficient alone to yield comprehensive information on the flow dynamics, which is why experimental studies are needed.

The present work consists of a novel application of PIV techniques to subaqueous debris flows. A series of experiments were run at the St. Anthony Falls Laboratory, University of Minnesota, in a 10 m long chute contained within a tank that allows the chute to be completely submerged in water. The experiments were carried out using four synchronised high-speed cameras.

The development of the PIV technique for this type of flow, combined with advanced experimental apparatus, allowed the measurement of quantities that - up to now - have been observed only in a qualitative way. Detailed velocity profiles as a function of time and slurry properties have been measured and related to pressure and rheological characteristics. Moreover, experimental pressures and velocities have been used to implement a CFD model that provided important information about the pressure distribution around the debris flow front, as well as the hydroplaning.

A substantial limitation, which our approach shares with virtually all others in the case of dense particulate flows, is that only surface velocity fields can be measured and only the presence but not the precise nature of 3D effects can be inferred from the measurements. However, the application of the PIV technique to debris flows is promising and the results represent a starting point for a deeper understanding of the dominant processes in such flows, as well as for the development of a new mathematical model.

This thesis starts with an outline of the submarine debris flow process(?) (Chap. 1). A complete description of the experimental setup, of the measurement of the mixtures' rheological characteristics and of the scaling problem, is given in Chapter 2. The developed PIV technique and its application to the experiments which were carried out is reported in Chapter 3. The last two chapters of this thesis contain a critical analysis of the experimental outcomes. In particular, Chapter 4 presents and points out the most relevant characteristic features of debris flow as measured with high speed cameras. Chapter 5 focuses on pressure measurement, and calculation using the CFD model. The collected data have been surveyed and compared to datasets reported in the literature.

The observations that were obtained in the experiments provide significant information and input for future modelling of the phenomenon.

Chapter 1

1 Introduction and background

1.1 Subaqueous debris flows and turbidity currents

Turbidity currents and subaqueous debris flows are one of the main processes of sediment transport on the Earth (Figure 1.1). They are responsible for the transfer of sediment from the continents to the oceans and the infilling of large sediment basins. They are therefore major geological phenomena, with a significant impact on a variety of issues.

Perhaps the most important economic impact derives from the fact that the porous rock and sand of many oil reservoirs were deposited by turbidity currents (Wesser, 1977; Hampton et al., 1996). The essential properties of reservoir rocks are their porosity and permeability (Hobson and Tiratsoo, 1981). Porosity provides the storage space for the oil, while permeability is needed to allow the movement of fluids through the rocks.

Debris flows and turbidity currents can be initiated by the failure of unstable sediment accumulated on the edge of a submarine shelf or at the head of an existing canyon (McGregor and Bennett, 1979), generating a submarine

landslide. Upon reaching the abyssal plain they spread out and deposit sediment on the ocean floor, reducing the flow's buoyancy and its rate of advance.

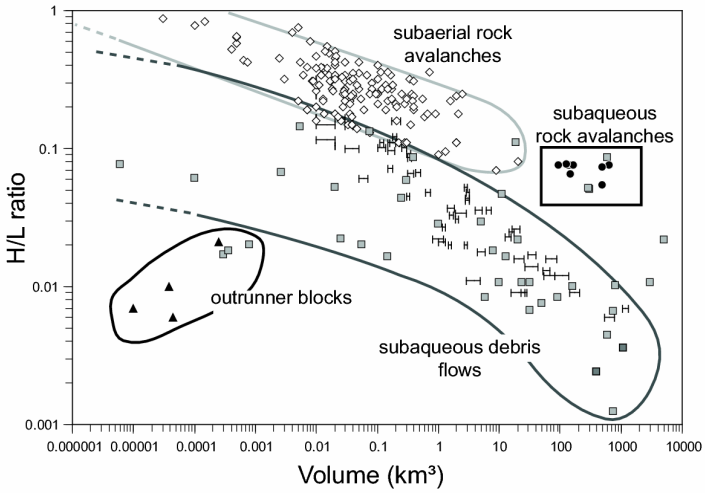

Figure 1.1. Diagram showing the distribution of subaqueous and subaerial landslide deposits, where the abscissa gives the volume of the landslide and the ordinate scale is the ratio H/L between the fall height of the landslide, H, and the horizontal run-out, L. Many cases of subaqueous debris flows have been found where the run-out ratio (H/L) is in the order of r~0.01 or less (Hampton et al., 1996; Elverhøi et al., 2002). Image from De Blasio et al. (2006).

Turbidity currents deposits have long been considered more important than debris flows as an agent for transporting sand to the continental margin and the abyssal plains. However, experimental works of Hampton (1970, 1972) showed convincingly that submarine debris flows have the potential for transporting large sediment masses over considerable distances[1]. Moreover they may play a

[1] Recently, the intensified search for deep-water hydrocarbon reservoirs with vastly improved surveying techniques, demonstrated the importance of debris flows as a major sediment mass transfer mechanism for the case of the Norwegian Barents Sea margin, where deep sea fans largely consisting of debris flows are found to be comparable in sediment volume to some of the

more important role in generating turbidity currents than hitherto recognised. Turbidity currents in the oceans (Figure 1.2) may be generated as a final phase of a sequence from land-sliding through debris flows to turbidity currents (Hampton, 1972). The transition from subaqueous debris flow to turbidity-current involves large dilution of debris flow material, reducing the density from about 2000 kg m^{-3} to 1.1 kg m^{-3}. How this dilution occurs has long been the subject of speculation, laboratory experiments and theoretical work (Kuenen, 1948, 1950, 1051; Hampton, 1972; Mohrig and Maar, 2003; Felix and Peakall, 2006).

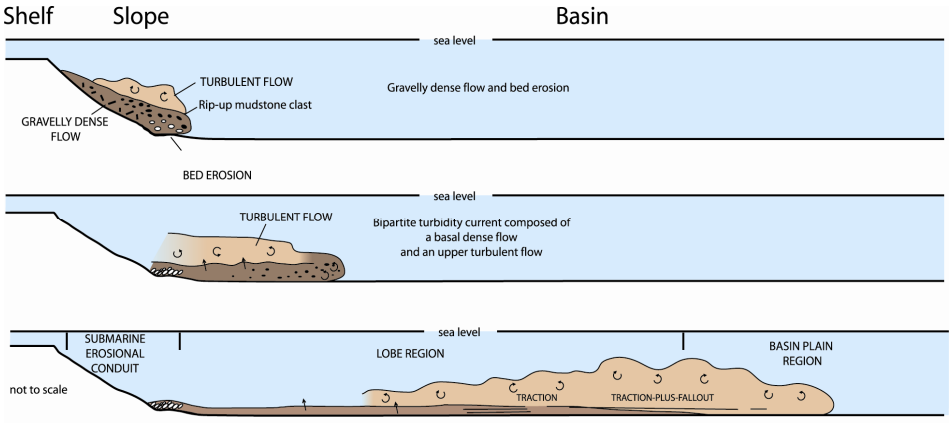

Figure 1.2 Main erosional and depositional processes associated with the down-slope evolution of a turbidity current. Modified from Mutti et al. (2003).

Submarine debris flows can often display very long run-out distances of up to 150 km or more, even on very gentle slopes, i.e. less than 1°. The long run-out distance on these low angle fans is a hydrodynamic enigma. In spite of increased viscous drag and reduced effective gravity due to the buoyancy,

world's turbidite fans (Elverhøi et al., 1998). Similar debris flows are also found on other glaciated margins (Aksu and Hiscott, 1992).

subaqueous debris flows have often been inferred to have attained significantly higher velocities and longer run-out distances than their subaerial counterparts (Elverhøi et al., 2000).

Promising sources of crude oil and natural gas occurs in correspondence with extended submarine sand bodies acting as reservoir rocks. Being able to predict the position of these sedimentary units would be highly advantageous for petroleum exploration. Although sand bodies are traditionally regarded as the product of turbidity currents, it has been recently argued that sandy debris flows may also contribute substantially to the deposition.

Information on the basic physics of the processes responsible and on the rheology of sand-clay-water mixtures will increase our understanding of the factors reshaping the sea bottom. This has considerable potential for oil exploration studies, as well as its application for gravitational mass transport.

1.2 Dynamics of subaqueous debris flows

The interest in this field has increased significantly in more recent years in conjunction with advances in seafloor and sub-seabed mapping augmented by further studies of ancient deposits on land. Observation of the deposits is not sufficient alone to yield complete information on the flow dynamics, which is why experimental studies are needed.

Several researchers have performed experiments during the last few years in order to understand the dynamics of gravity mass flows. A resume of those experiments is reported in the following pages, with a special focus on the interpretative model.

1.2.1 The role of debris flows in generating turbidity currents

Kuenen and Migliorini (1950) were among the first to perform laboratory flume experiments. They used mixtures of water, sand, clay and gravel and investigated the settling velocities of sand and the influence of salinity.

Hampton (1972) was the first to investigate the role of debris flows in generating turbidity currents. In particular, he examined the sequence from landsliding through debris flow to turbidity current, with the goal of describing the mechanisms by which turbidity currents can be generated. His experiments showed that subaqueous debris flow material mixed with the surrounding water through erosion of material from the front of the flow. Conditions that cause mixing at the front were illustrated by analysing flow around a sphere half, with boundary layer separation.

The problem has been treated in detail by Mohrig and Marr (2003) with experiments that focused specifically on these phenomena. They used a backscatter imaging technique to better resolve the internal boundary separating any turbulent mixing zone near the front of a flow from unmodified parent material. Their experiments address two questions: what fraction of sediment from the original dense flow is contributing into an overriding turbidity current, and to what degree is the original dense flow diluted through the ingestion of ambient seawater during the movement down slope? Three mechanisms of producing turbidity currents from parent mass flows were identified. All of them take place at the very fronts or heads of the parent debris flows because this is where large dynamic stresses develop (Mohrig et al., 1998; Marr et al., 2001; Mohrig and Marr, 2003).

The problem of turbidity current transformation into debris flow was recently studied by Felix and Peakall (2006), who looked at the efficiency of the transformation[2]. The experimental work was carried out using three different

[2] Efficient transformation means that most or all of the debris flow material is incorporated into the turbidity current, whereas for inefficient transformation most of the debris flow material remains as debris flow and little ends up in the turbidity current.

type of mixtures (non-cohesive silica flour, cohesive kaolinite and kaolinite-silica flour) at different concentrations. Ten multiplexed UDPV (Ultrasonic Doppler Velocimetry Profilers) were used to measure the flow field with a spatial resolution of 9 cm. an Ultrasonic High Concentration Meter (UHCM) was used to measure the concentration. They found that the extent of transformation depends on flow viscosity and density. Transformation of the less-dense flows is efficient with all or most material ending up in the resulting turbidity current.

1.2.2 Hydroplaning

The astonishingly long run-outs of subaqueous debris flows and the mismatch between their static shear strength measured in the laboratory and the dynamical shear stress during flow have attracted special interest (Locat et al., 2001; De Blasio et al., 2006). This high mobility is remarkable, considering that the characteristic slope angles in the submarine environment are very small, almost always less than 5° and often less than 1° (De Blasio et al., 2004b).

The key enigma connected to these flows - the extremely long run-out - is highlighted by Huang and Garcia (1998, 1999), who applied a viscoplastic model to subaerial and subaqueous laboratory debris flows of the same initial composition. They achieved very good agreement between measured and predicted run-out distances and deposit distribution in the subaerial case, but the model failed completely in the subaqueous case.

Hampton (1972) observed that, due to the combined action of dynamic pressure (Eq. [1.1]) at the snout and of dynamic underpressure above the head, at certain velocities the debris flow front is no longer capable of maintaining contact with the bed and a thin layer of water penetrates underneath the head and lubricates it. For a body moving in an fluid the relative fluid velocity at the front is zero. Here the pressure is highest with respect to the rest of the body (dynamic pressure, equation [1.1]).

$$P_D = \frac{1}{2}\rho_w U^2 \qquad [1.1]$$

where U is the average velocity and ρ_w is the water density. If the force due to the pressure becomes larger than the weight (Eq. [1.2]) the head starts to lift.

$$(\rho_d - \rho_w) g \cos\theta \, D < P_s \qquad [1.2]$$

where ρ_d is the debris flow density, D is the debris flow depth and θ is the bottom slope. Equations [1.1] and [1.2] can be rewritten in terms of densimetric Froude number (Eq. [1.3]).

$$Fr_d = \frac{U}{\sqrt{\frac{(\rho_d - \rho_w)}{\rho_w} gD\cos\theta}} = 1 \qquad [1.3]$$

A critical velocity can be found (Eq. [1.4]).

$$U_{crit} = \left[\frac{g\cos\theta(\rho_d - \rho_w) D}{\rho_w} \right]^{1/2} \qquad [1.4]$$

Previous experimental work (Harbiz et al., 2003) showed that debris flow heads hydroplane for densimetric Froude number in excess of about 0.3. The front velocity associated with Fr_d=*0.3* thus defines a critical condition for the onset of hydroplaning. At values of Fr_d higher than 0.3 the debris flow head becomes significantly deformed. The deformation of the front - that can help the normal pressure to lift the snout - combined with the reduced pressure above the head discussed by Hampton (1972), may explain why hydroplaning occurs for values of Fr_d than are clearly less unity (Harbitz et al., 2003).

For hydroplaning to occur, the flowing slurry must not devolve into a turbulent suspension. At the same time, the slurry must be sufficiently mobile to reach the critical velocity for the onset of hydroplaning. If these conditions are fulfilled, hydroplaning occurs when the flowing slurry cannot displace the ambient fluid fast enough.

In the field, where most debris flows are unconfined, side escape of lubricating fluid may be expected. This notwithstanding, Marr et al. (2001) and Toniolo et al. (2004) demonstrated experimentally that unconfined subaqueous debris flows hydroplane with about the same ease as their confined siblings. In addition, at the normally large dimensions of field-scale submarine flows, the main part of the lubricating fluid must travel a relatively long distance in order to escape from the sides. For both confined and unconfined flows the possibility of water percolation into the overriding debris flow should also be considered. If the debris material is extremely impermeable (high clay content) the confined lubricating film, once established, can be expected to be capable of maintaining the hydroplaning of the debris material. On the other hand, sandier or more granular flows show clear evidence of water percolation, loss of excess pore pressure, and break-up (Harbitz et al. 2003, Marr et al., 2001).

During hydroplaning the debris flow head experiences reduced frictional forces while the main body of the flow does not. A large velocity difference may develop between the head and the body of the flow, that implies a very significant amount of stretching. Hence, as the head accelerates and moves away from the body a neck forms that becomes progressively thinner; with the reduced cross-section, the tensile stresses increase. Furthermore, the stretching leads to the formation of cracks through which ambient water can penetrate, leading to additional local softening of the material.

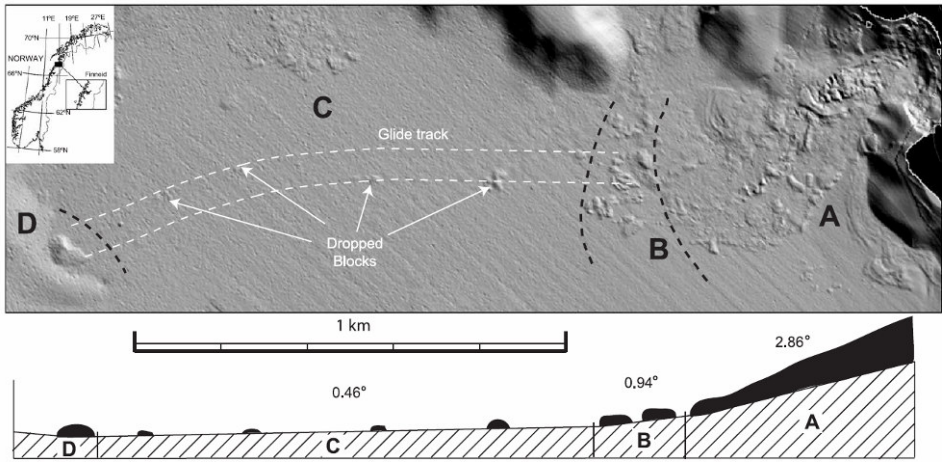

Figure 1.3. Finneidfjord slide with slide morphology divided into zones. Zone A: Main lobe. Zone B: Zone with scattered blocks. Zone C: Glide zone. Zone D: Main out-runner block. Average bottom slopes along the slide and glide path are shown in the lower panel (image taken from Ilstad et al., 2004).

Under certain conditions, the head may detach completely from the body and form an out-runner block (Elverhøi et al., 2005), a process termed ‘‘autoacephalation’’ (Parker, 2000). Examples of such out-runner blocks have previously been identified in laboratory experiments (Hampton, 1972), and in the field by bathymetric surveys (Prior et al., 1984) and from seismic data (Nissen et al., 1999). In Figure 1.3 the example of the Finneidfjord slide, where out-runner blocks travelled ahead of and outside the main lobe (Ilstad et al., 2004a), is presented.

1.2.3 Submarine debris flows models

Improved field studies, laboratory experiments and rheological measurements have driven several researchers to propose models for the dynamics of submarine debris flows during the last decades.

The first model was probably that of Morgenstern (1967), who proposed a one-dimensional analytical solution for the movement of submarine landslides. Morgenstern's model was based on soil mechanics principles, with pore-water pressure as the major element responsible for the very low apparent friction coefficient. Later, Hutchinson (1986) proposed a one-dimensional model also based on the plastic behaviour of the failed mass, although he added a pore pressure dissipation term, based on consolidation theory. In both models the one-dimensional approach required that the failed mass moves as a plug with no internal velocity gradient. Observations of debris flows indicate clearly that shearing takes place in the failing mass, mainly as laminar flows. This aspect was considered by Hampton (1972), Edgers and Karlsrud (1982), all of whom modelled submarine debris flows as a fluid with mixture properties similar to those of a Bingham viscous fluid.

With the recent granular flow studies on dry sand (Hutter and Savage, 1988; Savage and Dai, 1992; Wildemuth and Williams, 1985), saturated sandy mixtures or debris flows (Takahashi, 1991; Ravenne and Beghig, 1983; Davies, 1986; Pierson and Costa, 1987; Chen, 1988; Mizuyama and Yazawa, 1987; Hungr, 1988; Major, 1993; Chen et al., 1993; Coussot and Piau, 1994), and snow avalanches (Irgens, 1988), it became clear that the mechanics of these mass movements are complex and that constitutive equations for sediment deformation must include both plastic and viscous parameters.

Such an approach was proposed by Norem (Norem et al., 1990) for submarine landslides (Eq. [1.5]).

$$\tau = \tau_y + \sigma\left(1 - r_p\right)\tan\phi' + \mu\,\rho_d\left(\frac{dv}{dy}\right)^r \qquad [1.5]$$

where τ is the total shear strength, τ_y is the yield strength, s is the normal stress, r_p is the pore pressure ratio $p/\gamma D$, ϕ' is the friction angle, μ is the Bingham viscosity and ρ is the density of the mixture.

This model do not take into account hydrodynamic drag forces acting on the moving mass. To evaluate these drag forces, Norem (Norem et al., 1990), proposed an equation developed by Schlichting (1968) that describes turbulent flows over a rough surface. The non-dimensional shear stress at any point x along the plane is defined in Eq. [1.6].

$$\frac{\tau}{\rho_w U^2} = \frac{1}{2}\left[2.87 + 1.58\left(\frac{x}{k}\right)\right]^{-2} \qquad [1.6]$$

where ρ_w is the water density, U is the slide velocity and k is the roughness length. If we assume U to be constant, the averaged shear stress over the length L is given in Eq. [1.7].

$$\frac{\tau}{\rho_w U^2} = \frac{1}{2}\left[1.89 + 1.62\left(\frac{x}{L}\right)\right]^{-2} \qquad [1.7]$$

Norem applied his model to the Sokkelvik submarine landslide in Norway, and estimated the resistance to flow resulting from the drag force on the surface as about 1/3 of the shear resistance at the base of the slide.

Field and laboratory data suggest that the rheology of a muddy debris flow can be approximately described by linear (Bingham) or nonlinear (Herschel-Bulkley) viscoplastic models (Johnson, 1970; O'Brien and Julien, 1988; Wan and Wang, 1994; Locat, 1997). In the Herschel-Bulkley rheology the relationship between the shear stress τ and the strain rate γ can be expressed as (Eq. [1.8]).

$$\tau = \tau_y + \mu\,\gamma^n \qquad [1.8]$$

where *n* is an exponent usually less than 1. For the limiting case of *n=1* Eq.[1.8] reduces to the Bingham model.

The Bingham rheology can be essentially generalised by the bilinear rheology (Imran et Al., 2001) that in the formulation of Locat (1997) takes the form of Eq. [1.9].

$$\tau = \left[\tau_{ya} + \mu_h |\gamma| - \frac{\tau_{ya}\,\gamma_0}{|\gamma| + \gamma_0} \right] \qquad [1.9]$$

where

$$\gamma_0 = \frac{\tau_{ya}}{\mu_l - \mu_h} \qquad [1.10]$$

The model uses two viscosities that must be of substantially different magnitudes in order to be meaningful. At sufficiently high strain rates, the flow behaves as a Bingham fluid with a low viscosity μ_h and an ''apparent'' yield strength τ_{ya}. At very low strain rates, however, the flow behaves as a Newtonian fluid with a high viscosity μ_h. In this a way there is no need for a specific yield strength τ_y below which flow deformation ceases.

Imram (Imram et al. 2001) presented a 1D numerical model for subaqueous debris flows model that incorporates the Herschel-Bulkley and the bilinear rheologies of viscoplastic fluids[3]. In their model the conservation of mass and momentum equations of single-phase laminar debris flow are layer-integrated using the slender flow approximation. They are then expressed in a Lagrangian framework and solved numerically using an explicit finite difference scheme.

The model has a number of limitations. A 1D layer-integrated model is not sufficient to describe the lateral spreading of debris flows. The model does not include the resistive drag that may arise at the interface between the debris flow

[3] The Bingham model is integrated into the Herschel-Bulkley rheological model for the case of $n = 1$.

and the water. Nor is the model capable of describing sandy debris flows (Shanmugam, 1996) that contain very little fines; models for such flows must include a description of the interaction between variations in pore pressure and frictional resistance (Iverson, 1997). Moreover, the model is limited to muddy debris flows in the laminar regime and is insufficient to describe the flow of a turbulent mud slurry (Imram et al., 2001).

Although the viscoplastic concept seems valid for clay-rich subaqueous debris flows, the very long run-out distances on gentle slopes are not adequately understood and have been variously attributed to flow characterised by a low coefficient of friction, a low viscosity, and/or a low yield strength, as well as the maintenance of a sufficient flow height to ensure mobility for canalised flows (Harbitz et al., 2003, Schwab et al., 1996). However, recent laboratory experiments have demonstrated that the mobility of subaqueous debris flows may be enhanced by hydroplaning (§ 1.2.2).

A model capable of reproducing this phenomenon was presented by De Blasio et al. (2004a). In this model, the flow behaves essentially as in the Imram model (Imram et al., 2001) if the velocity is subcritical (§ 1.2.2). When the critical velocity is reached, a thin wedge of water penetrates beneath the flow and the stress is reduced considerably. In particular when hydroplaning occurs the stress in the mud is supposed to not exceed the yield strength and the flow may be treated as a hydroplaning plug (i.e. the shear layer thickness becomes essentially zero). The hydro-planning plug is characterised by a constant velocity for the whole cross-section of the debris flow. During hydroplaning the stress at the bottom of the mudflow is equal to the stress at the top of the water layer τ_w. The hydroplaning plug model is obtained by equation [1.11].

$$\frac{d\overline{u}}{dt} = -Rg_y \frac{\partial}{\partial x}\left(D + D_w\right) - \frac{\tau_t - \tau_w}{D\rho_d} + Rg_x + f_p \qquad [1.11]$$

where $R = 1 - \left(\rho_w / \rho_d\right)$ is the non-dimensional reduced density of the debris flow (Eq.[2.1]), D_w is the thickness of the water layer, g_x and g_y are respectively the x and y components of the gravitational acceleration and τ_t is the stress at

the top of the mud layer. For hydroplaning flows, drag forces were found to be very important. These forces can be basically divided into frictional drag (Eq. [1.12]) and the pressure drag term (Eq. [1.13]).

$$\tau_t = -\frac{1}{2}\rho_w C_f u_p^2 \qquad [1.12]$$

$$f_p = -\frac{1}{2}\frac{\rho_w}{\rho_d}\frac{C_p}{D}\left|\frac{\partial D}{\partial x}\right| u_p^2 \qquad [1.13]$$

where C_f is the frictional drag coefficient and C_p is the pressure coefficient.

1.3 The goal: getting inside the dynamics of debris flows

In order to improve models for predicting sediment properties and geometrical distribution, there is a need for a better understanding of the hydrodynamic aspects of the flow regime both within the flow as well as in the ambient water masses.

In this direction the present work has a twofold aim. The first is to develop a PIV technique in order to apply it to the subaqueous debris flows. Subsequently experiments with a advanced experimental setup, comprehensive of four high speed digital camera for the PIV application, will be carried out. Hence this thesis will focus on the basic physics of how a sedimentary body of mixed composition (clay-silt-sand) may evolve during down-slope movement, and on the role of pressure distribution and rheology.

The experimental collected data will be surveyed and compared to the ones reported in literature. A critical process of data reduction will allow to get the most relevant flow properties for different chute sections and mixtures.

Chapter 2

2 Laboratory experiments

A series of dedicated experiments of sand-clay-water mixtures have been performed during the summer and autumn of 2006 in a flume at the St Anthony Falls Laboratory in Minneapolis, USA. The SAFL was chosen by those responsible for the project because a 9 m submergible chute was already installed. Moreover, a team of expert technicians and co-workers (working students) was available there during both the setting up and running of the experiments. Each experiment required the preparation of more than 350 kg of slurry and the simultaneous use of six cameras and four pressure sensors. Four people were needed for each run which lasted approximately five hours.

All the experiments described in this work were carried out by the writer and Hedda Breien (PhD student from the University of Oslo). In particular Hedda Breien was in charge of experiments coordination, while the writer had the responsibility of the camera and the pressure acquisition system, including their design and installation. Moreover the writer created and used a new PIV technique ad hoc for those experiments. A complete description of this technique and its application is given in Chapter 3. The work was planned

during two preliminary meetings, the first in Pavia (March 2006) and the second at the SAFL (May 2006), and carried out from July to September 2006.

The present chapter gives a detailed description of the experimental set-up (§2.2), including the scaling technique adopted (§ 2.1) and the rheological characteristics of the mixtures and the related problems (§ 2.3).

2.1 Scale effect

The experiments were conducted at a scale that was much smaller than those characteristic of the field. Proper scaling involves using an appropriate geometric scaling technique as well as maintaining similarity in the proper dimensionless parameters. For subaqueous debris flow modelling, distorted geometric scaling is used to accomplish the former. This is commonly used in river modelling and involves scaling down the horizontal and vertical dimensions of the system by differing amounts, λ_h and λ_v, respectively (Graf, 1971). This makes it possible for the thick submarine debris flows found at field scale on relatively shallow slopes to be modelled in the laboratory by thin subaqueous flows on steeper slopes.

The identification of appropriate dimensionless parameters for scaling debris flows is nontrivial (Iverson, 1997). Inertial interaction of grains, shear-rate dependency of rheology, and transient changes in sediment concentration are just few of the complicating issues (Major and Pierson, 1992; Coussot and Meunier, 1996; Iverson, 1997, Marr et al., 2001). In the narrowly defined case of subaqueous debris flows with a Bingham rheology, however, strict similarity of bulk properties requires similitude in only four nondimensional numbers (Mohrig et al., 2003): the Reynolds number Re, the densimetric Froude number Fr, the dimensionless yield strength τ_y^*, and the fraction excess density of the debris flow slurry *R*.

$$\mathrm{Re} = \frac{UH}{\upsilon_d} \quad [2.1]$$

$$R = \frac{(\rho_d - \rho_w)}{\rho_d} \quad [2.2]$$

$$Fr = \frac{U}{\sqrt{RgH}} \quad [2.3]$$

$$\tau_y^* = \frac{\tau_y}{\rho_d U^2} \quad [2.4]$$

In these equations, U is flow velocity, H is flow thickness, ν_d is the debris slurry cinematic viscosity, ρ_d is the debris slurry density, and ρ_w is the density of the water the debris flow moves through. The vertical (horizontal) scale ratio λ_v (λ_h) is defined here as the ratio of any vertical (horizontal) length in the model (e.g. laboratory) to the corresponding vertical (horizontal) length in the prototype (e.g. field). For simplicity, it is assumed here that the values of ρ_w and ρ_d do not differ between model and prototype, ensuring similarity in R. An application of the principles of distorted modelling yields the following scaling (equations from [2.5] to [2.10]); where L_r denotes run-out length, S denotes bed slope and subscripts m and p denote model and prototype.

$$(L_r)_m = \lambda_h (L_r)_p \quad [2.5]$$

$$(H)_m = \lambda_h (H)_p \quad [2.6]$$

$$(S)_m = \frac{\lambda_h}{\lambda_v} (S_r)_p \quad [2.7]$$

$$(U)_m = \lambda_v^{1/2} (U)_p \quad [2.8]$$

$$(\tau_y)_m = \lambda_v (\tau_y)_p \qquad [2.9]$$

$$(\nu_d)_m = \lambda_v^{3/2} (\nu_d)_p \qquad [2.10]$$

Some fairly typical model values for L (chute length), H (maximum value for a deposit), S , U, and τ_y for the experiments reported here are, L=10 m, H=0.04 m, S=0.105, U=1 m/s, and τ_y=20 Pa, respectively.

Assuming, λ_v=1/250 and λ_h=1/2500, the model values translate into the respective prototype values of 22500 m, 10 m, 0.01 (0.6 deg), 15.8 m/s, and 5000 Pa. Although these values do not apply to any specific submarine debris flow, they do correspond to the correct order of magnitude for a variety of field cases for which estimates have been made (e.g., Prior and Coleman,1979; Edgers and Karlsrud, 1981; Hampton et al., 1996).

The scalable information for Bingham-type debris flows is limited to the gross features of the flow dynamics and deposit. Results concerning the grain structure of the deposits may not readily scale up, if only because the ratio of characteristic grain size to deposit thickness can be expected to differ vastly between model and prototype. With this in mind, caution is advised in translating the observed grain-scale structures to field scale. Also, flows that are transitional, such as the weakly coherent flows, may deviate sufficiently from the Bingham approximation to require a different scaling (Iverson, 1997).

It has to be noted that experiments were conduced with tap water. In the field salt water leads to the flocking of clay particles that form aggregates. This may introduce some errors with respect to the relationship between experiments and the real phenomenon.

2.2 Experimental set-up

The design and set-up of the experiments was an important part of the present research. In the present chapter there is a complete description of the laboratory and the experimental apparatus.

2.2.1 Chute

The experiments were performed in a flume inside a 10 m long, 3 m high and 0.6 m wide tank (hence referred to as "the fish tank"). The fish tank (Figure 2.1) can be filled completely with water and has transparent Plexiglas walls. A 0.2 m broad Plexiglas flume is submerged in the tank and can be adjusted to the desired sliding angles by means of wires. One slope break is possible. For our experiments the whole inner flume was tilted to an angle of 6^{o}. To ensure a rough bed in the flume, a granular roof tarp was installed. The roughness of the tarp was about 1 mm and made the desired shear layer at the bed possible, preventing unwanted slip.

On top of the flume is mounted a head tank (Figure 2.2). To run an experiment, the sediments are filled into the head tank which is emptied by a manually operated gate mechanism. The sediments run down the inner flume and fall into the large tank at the end.

The fish tank can be filled completely with water within 3-4 hours when all hoses are in use, and emptied within a few minutes. At the end of each experiment river water can be used to clean it faster. Three valves are installed in the bottom of the tank and a sedimentation basin is built beside the tank.

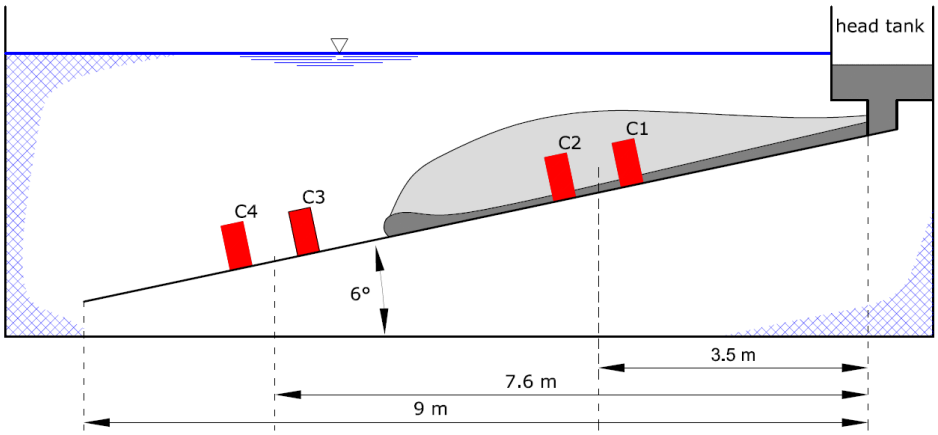

Figure 2.1 Side and upper view of the chute and the fishtank.

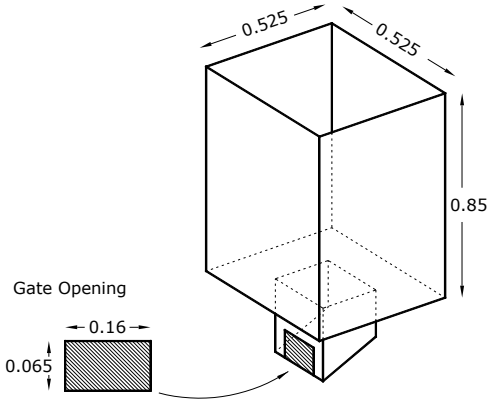

Figure 2.2 Head tank scheme, measures are in metres.

2.2.2 Pressure sensors

Measurements of both fluid pressure and total bed normal stress were performed simultaneously at the chute base. Sensors were placed in two cross-sections along the flow channel, 3.5 and 7.6 m from the head gate (Figure 2.1). Total pressures were measured with a Honeywell ABH006PGC1B transducer mounted flush with the bed. Transducers used for pore-fluid pressure were Druck PTX1400. Measurements of the pore-fluid pressure were done through a 10 mm diameter porous stone mounted flush with the bed. An alloy adaptor was made to assemble the porous stone and the Druck sensor (Figure 2.3). This adaptor allows - thanks to a bleeder hole - the porous stone to be purged and the air to be removed from the system.

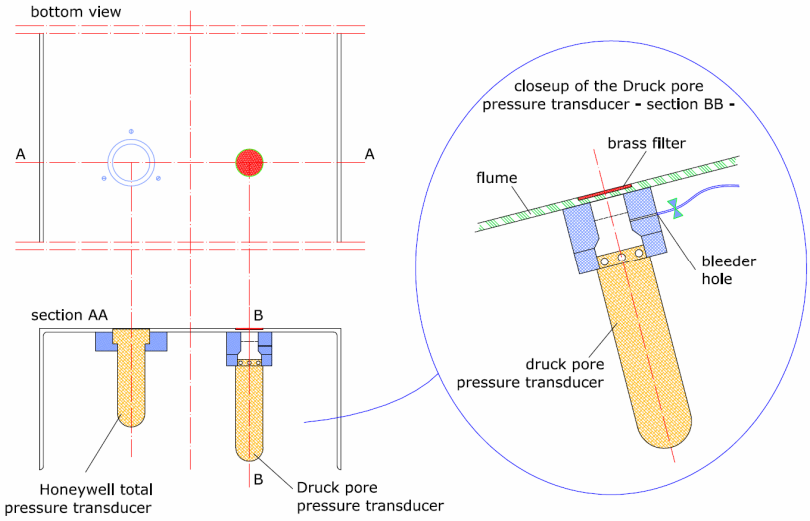

Figure 2.3 Scheme of the pressure transducer mounted behind the bottom of the chute.

All transducers measure pressure with reference to ambient air pressure and may be affected by barometric changes. Therefore, calibration was done prior to

each experiment series. A ruler with increments in tenths of centimetres, mounted on the side of the tank, was used as a reference for the calibrations. The calibration procedure consists of gradually filling the fish tank, reading the water level on the ruler at several steps and measuring the output voltage of the sensors. The voltage signal read by the DAQ system is averaged over two thousand points in order to get rid of the noise. Water level is related to output voltage at the end of the procedure using a linear equation, since the sensors are linear over their operating range.

2.2.3 Acquisition system

The data acquisition system (hence referred as DAQ) used for the experiments is the DAQCard-AI-16E-4 made by National Instruments. The resolution of the card is 12 bits, and the sampling rate was set to 1000Hz.

A National Instruments SC-2345 terminal box was used. It gets 5 volt power from the computer, so no external power supply is needed. Analog input signal connections were made using a SCC-FT01 module for each of the channels. The SCC-FT01 is a feed-through module that connects directly to the analog input (AI) and analog output (AO) channels of the DAQCard-AI-16E-4 data acquisition device. The modules are mounted and connected inside the SC-2345 terminal box.

The excitation voltage for the pressure sensors was created from an external 12 volt supply. From that supply 10 volts was created for the Druck sensors, and 5 volts for the Honeywell sensors.

The DAQ system and cameras are triggered by a TTL voltages derived from the frame grabber. When the gate is opened, a switch connected to the head tank handle closes the trigger circuit of the DAQ system. Similarly the TTL signal was acquired by the camera system.

The software used in the data acquisition was LABview made by National Instruments.

2.2.4 High speed cameras

Four Silicon Video 9M001C high speed digital cameras, coupled with two PIXCI board cameras have been used. Each frame grabber can manage two cameras. They provide power to the cameras, sends and receives cameras control signals, generates the programmable pixel clock, and receives video data. No dedicated power supply or power cable are required.

The cameras are based on MT9M001 CMOS sensors from Micron, a progressive scan[4] sensor, capable of a resolution of 1280 x 1024 pixels at 43 frames per second and 10 bit colour depth[5].

Frame Rate Examples (Pixel Clock Frequency 48 MHz)	
Frame Resolution	Frame Rate
1280 x 1024	30 fps
774 x 580	77 fps
640 x 480	107 fps
342 x 256	290 fps
1280 x 4	1049 fps

The experiments were recorded with a resolution of 600x200 pixels (vertical x horizontal) at a frame rate of 240 frames per second. The choice was based on some considerations concerning PIV technique, flow velocity, tracer particles and camera characteristics. The flow height to record was fixed at about 0.1m. In order to obtain a good PIV each particle has to be contained in at least 2 pixels. In the experiment as a tracer coal slag particles, a siliceous material produced as a residue from burning coal, with average diameter of 500μm (§

[4] Progressive or non-interlaced scanning is any method for displaying, storing or transmitting moving images in which the lines of each frame are drawn in sequence. This is in contrast to the interlacing used in traditional television systems. This is a fundamental characteristic that cameras used in quantitative imaging techniques must have.

[5] Colour depth, also known as bits per pixel (bpp), is a computer graphics term describing the number of bits used to represent the colour of a single pixel in a bitmapped image.

2.3.1) have been used. The vertical resolution was fixed to 600 pixels (3 pixels per particle). The maximum displacement in pixel has to be smaller than 32. Since the flow velocity is about 1 m/s (from previous experiments), we imposed a frame rate of 240 frames/second in order to have a displacement between two consecutive frames of about 25 pixels. Once frame rate and vertical resolution have been set to 240 fps and 600 pixels respectively, the maximum horizontal resolution the camera allows is 200 pixels.

The SV9M001 cameras offer asynchronous capture. This makes possible to use a trigger signal to start the images recording. We used this characteristic to synchronize the cameras with the DAQ system.

The cameras were placed at respectively 4.120 – 4.620 – 7.307 – 7.807 metres downstream of the gate (Figure 2.1). In this way we had two pairs of cameras. The distance between the cameras in each pair is 0.5 metres and the distance between the pairs is about 3.2 metres. We decided one these locations in order to study velocity and velocity field variations on a small scale (between two cameras of the same pair, 0.5 m) and on a bigger scale, i.e. between the two pairs.

For each experiment every camera recorded 4000 frames (about 16.6 seconds) starting from the trigger signal. The recorded images are stored in frame files in bitmap (.bmp) format.

The cameras are controlled by the XCAP Imaging Application software. It provides a “Capture & Adjust Dialog” for selecting pixel clock frequency, integration/exposure time, capture resolution, gain, offset, trigger control, and more. In addition a “Colour Camera Dialog” provides automatic white balance as well as manual adjustment of red, green, and blue gain. The colour gains were accurately calibrated in order to avoid problems of green dominance due to halogen lighting (greenB=0; blue=6; red=4.2; greenR=2.7).

2.3 Mixtures

The slurries were composed of sand, coal slag, kaolin and tap water. They have been prepared with five (5) different compositions by varying the clay and sand contents. Mixture composition and mixing procedure are described in paragraph 2.3.1 and rheology measurements in paragraph 2.3.2, while the rheological characteristics are discussed in paragraph 2.3.3.

2.3.1 Mixtures composition and mixing procedure

The debris flows were composed of coarse red flint sand, industrial kaolin (Snowbrite) and coal slag (Black Diamond). Kaolin was chosen as it is a less reactive clay, with density 2.75 g/cm^3. The diameter and density of the sand and the coal slag are 1 mm and 2.65 g/cm^3, and 500 μm and 2.6 g/cm^3, respectively. The sand is light reddish brown, whilst the coal slag is black and easily distinguishable from the sand. Every run contained 5% coal slag by weight for easier particle tracking.

Sand-clay-water mixtures of varying concentrations have been used. A complete range from low (5%) to high (25%) clay concentrations was tested (with a 5% clay increment between each slurry composition), whilst the water content was kept constant at 28 weight per cent. This provided a range spanning from completely viscoplastic to more granular behaviour. Trial mixtures with clay concentrations of less than 5% did not fulfil the requirement for an homogeneous material, as the sand grains settled out rapidly and resulted in a two-phase debris flow. In the following the different slurries are differentiated and referred to by their clay concentration.

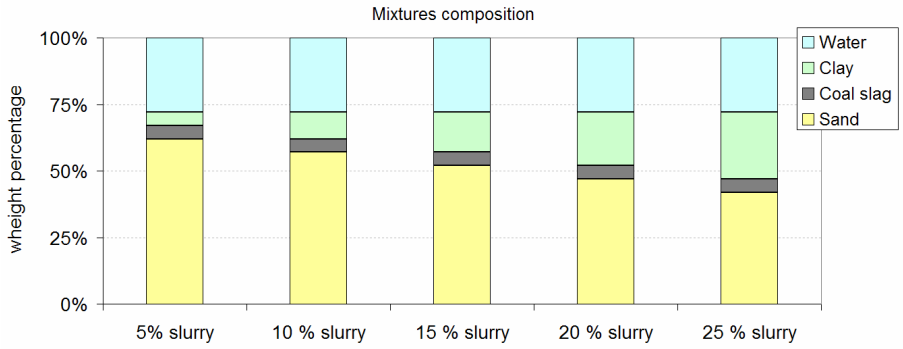

Figure 2.4 Mixtures composition.

Before each run, clay, sand, Black Diamond and water were weighed and put in buckets. Clay and water were then mixed in a hopper (cement mixer) before sand and coal slag were added incrementally, with the hopper running for half a minute in between. When all sediment had been added, the hopper was left to run for 30 minutes to produce an homogeneous, remoulded sediment. A visual check of the mixture was always performed. Thereafter the mixture was loaded into the flume headtank. It was important that the mixing and loading time remained the same in all the experiments. In fact it was seen that the rheology of the mixture is both time and motion dependent (§ 2.3.3).

In the head tank the sediment was stirred (manually) to prevent settling and ensure an homogeneous mixture until the experiment was ready to be run.

2.3.2 Rheometrical measurements

Sand-clay-water mixtures analogous to the ones used in the laboratory runs at SAFL were tested in a ball rheometer (Appendix B) at the Department of Chemistry, University of Oslo. Direct measurement of the slurries was not possible during the experiments at SAFL. The Oslo mixtures where prepared in a comparable way as to those used in the flume runs. Dependency of the rheology on clay concentration, water concentration and time was tested.

Figure 2.5 presents an example of flow curve measurements for the case of 15% clay mixture. The measurements were conducted for shear rates from 0.1 s^{-1} up to 100 s^{-1}. The rates were increased stepwise[6] and thereafter decreased in the opposite direction. For each shear rate increments up to 0,5 s^{-1}, 50 measurements where taken; for the other shear rates 40 measurements were taken.

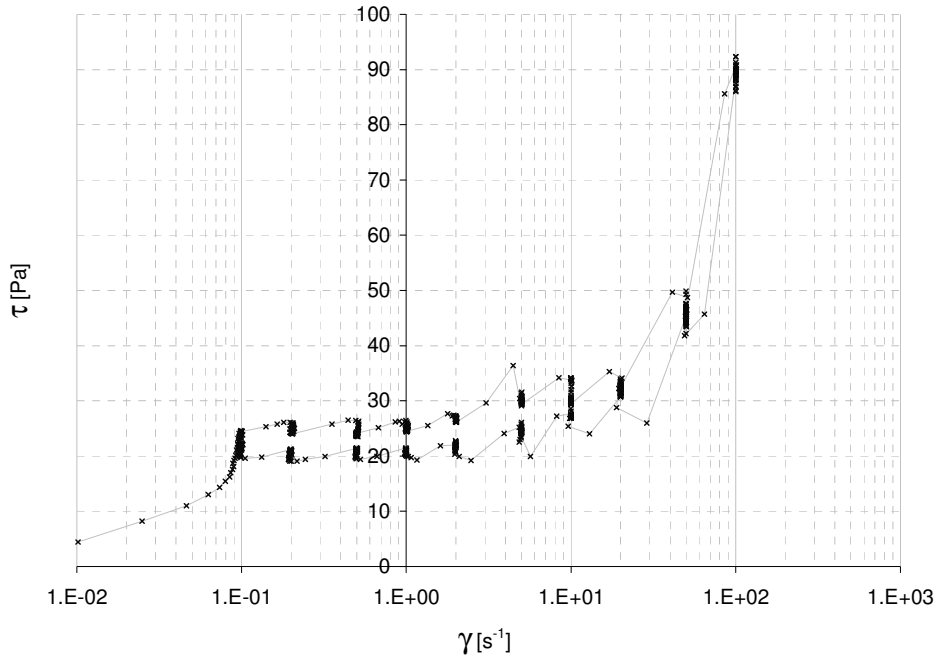

Figure 2.5 Flow curve for the 15% clay mixture. A complete cycle is reported (the upper part corresponds to the shear rate increasing).

The sphere requires time to accelerate up to the desired shear rate requires some time. A stress undershoot appears at the beginning of the measurements at low shear rates, while stress overshoot occurs at higher shear rates (example in

[6] The following shear rates were considered: 0,1 s^{-1}, 0,2 s^{-1}, 0,5 s^{-1}, 1 s^{-1}, 2 s^{-1}, 5 s^{-1}, 10 s^{-1}, 20 s^{-1}, 50 s^{-1}, 100 s^{-1}

Figure 2.5). In the shear rate vs. shear stress diagrams, hysteresis loops are observed. They reflect the difference in material response with flow history. In fact clay-water mixtures are well know as typical thixotropic materials[7] (Coussot, 1997).

Low clay content slurries (especially the 5 % ones) do not really stabilise and the shear stress becomes progressively smaller (at a constant shear rate), due to settling of sand particles. This is a major complicating factor in debris flow dynamics, discussed in detail in §2.3.4.

2.3.3 Rheology

Average shear stresses and shear rates were calculated from the collected data in order to obtain average flow curves for the different slurries (Figure 2.5).

Only the increasing shear rates were used. Shear stresses corresponding to shear rates higher than 20 s^{-1} were not used either, because at larger shear rates the flow can no longer be considered laminar and the BRS then lacks one of its basic hypotheses (§ 2.3.2). Moreover we did not take into account shear stresses corresponding to shear rates lower than 1 s^{-1}; looking at the flow curves in Figure 2.5, a minimum is present at about $\gamma = 1$. For lower values of γ the flow curve has to be considered unstable (Coussot, 1997).

The viscosity is shear thinning, as are most clay-water suspensions, according to Coussot (1997). The slurries behave as expected when it comes to viscosity, shear and yield stress as functions of clay concentration. The higher the clay concentration, the higher are viscosity and shear stress.

Among all the rheological models in literature, the Herschel and Bulkley model (Eq. [1.8]) was found to be the most appropriate to interpret the experimental data.

[7] In the general sense of viscosity change during the time.

$$\tau = \tau_y + \mu\, \gamma^n \qquad [2.11]$$

where τ_y is the critical shear stress, μ is the viscosity-parameter and n is the Herschel-Bulkley index. The parameters obtained from the fitting are reported in Table 2.1, while Figure 2.6 shows the experimental and the calculated flow curves.

Table 2.1 Parameters of the Herschel–Bulkley models. Ty is in Pascal.

Clay content	τ_y *[Pa]*	μ *[Pa·s]*	*n* *[-]*	R^2 *[-]*
5%	2.55	4.78	0.27	0.919
10%	6.30	6.77	0.19	0.927
15%	15.54	7.32	0.26	0.991
20%	38.31	11.32	0.31	0.997
25%	94.17	4.39	0.56	0.989

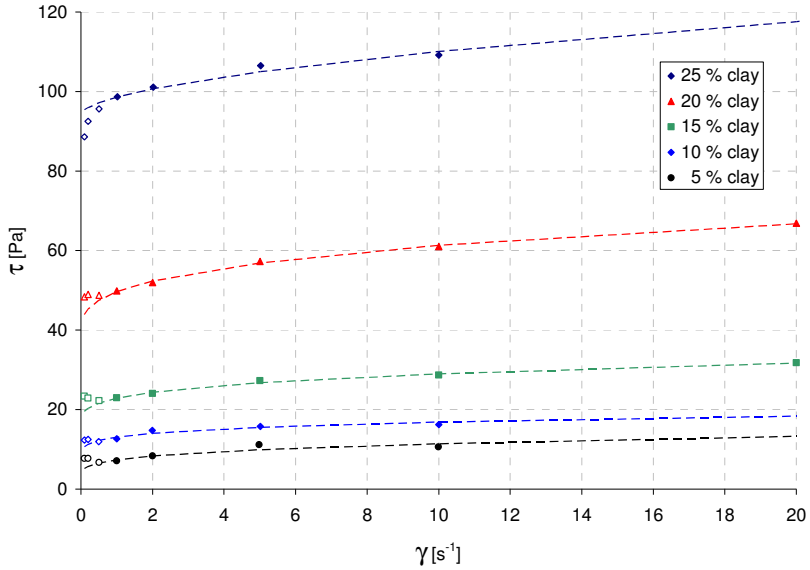

Figure 2.6 Average shear stresses as function of the shear rates. Dashed lines are the fittings obtained with the general Herschel–Bulkley function. The experimental data plotted with an empty symbol have been not taken into account for the data fitting.

For low clay content the Herschel–Bulkley index *n* is very low and the flow curve almost horizontal, corresponding to a more granular behaviour. In fact, the shear stress for an unconfined granular material is shear rate independent. On the other hand at high clay contents *n* lies in the range of 0.3-0.5, as expected for a clay-rich debris flow.

A direct measure of the yield stress was not possible. We approximated it with the shear stress level corresponding to a shear rate of 0.01 s^{-1}, according to Coussot et al. (1993). This should provide a theoretical yield stress very close to the real one, with an uncertainty sufficiently small to be negligible for conventional practical applications (Coussot, 1997). Figure 2.6 shows that the calculated yield stress increases exponentially as a function of the mixture's

clay content, in agreement with the result of other authors (Coussot and Piau, 1994; Coussot, 1995).

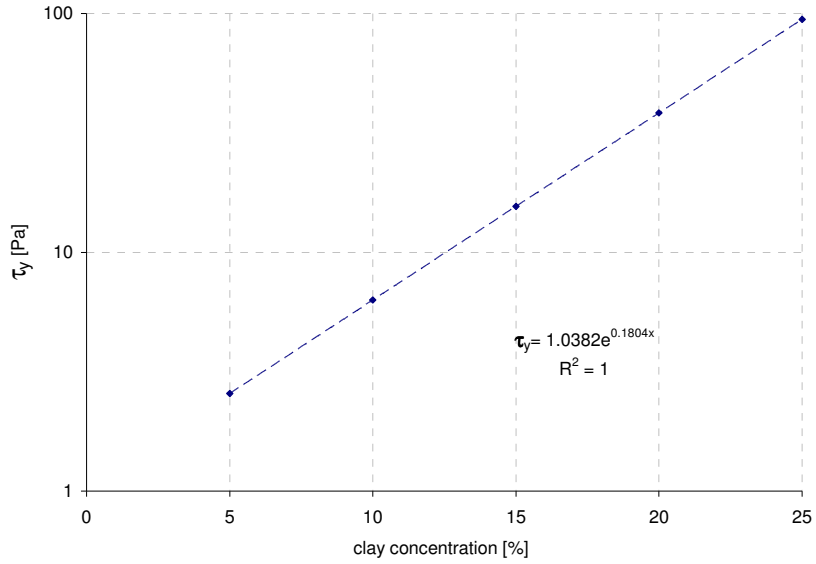

Figure 2.7 Yield stress as a function of clay content in the mixture. Dashed line represents an exponential interpolation of the data. Plot in semi-logarithmic diagram.

Rheological measurements of the same slurry after different times (10 min, 30 min, 45 min, 100 min, 220 min, 340 min, 24 hours, 6 days, 6 days + 6 hours, 7 days) show that viscosity and shear stress clearly increase with time (Figure 2.8). Clay mixture, as has already been pointed out, are a thixotropic fluid. In this case has been demonstrated that the viscosity is dependent, not only on the clay content, but also on the "shear rate history", that cause the flocs ropture.

For that reason it has been important to control that the mixing ad loading time was the same in each experiment.

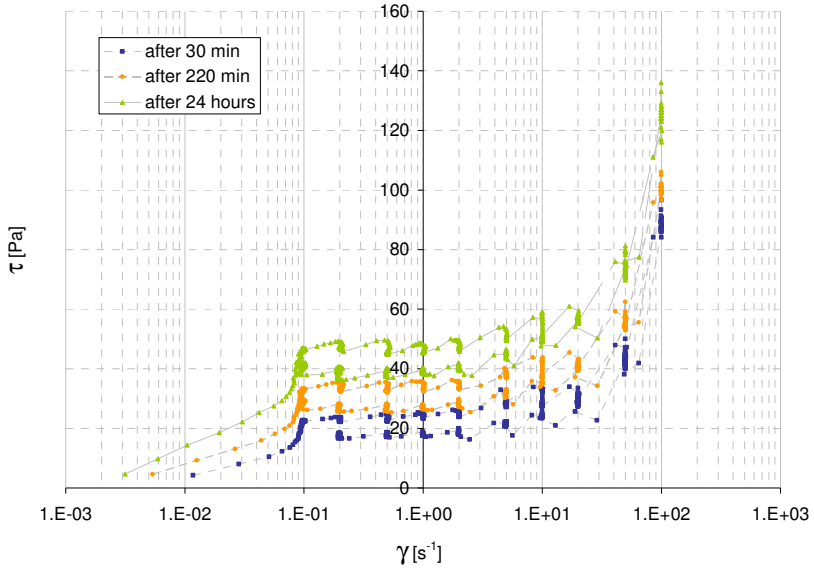

Figure 2.8 Time dependences of the rheology. With different colours have been represented flow curves of the same slurry after different time from the initial mixing (30 min, 200 min, 24 hours).

2.3.4 Discussion

Identification of an appropriate rheology has long been regarded as the key to successful interpretation, modelling and prediction of debris-flow behaviour. Debates about the most suitable rheological formula have persisted for several decades. At the same time, field observations and video recordings of debris flows have provided clear evidence that rheologies vary with time, position and feedbacks that depend on evolving debris-flow dynamics (Iverson, 2001).

Predictions of debris flow motion - because of the evolving behaviour of debris flows - is too complex to be represented by any rheological equation that uniquely relates stress and strain rate. Moreover, behaviour can vary if debris composition changes as a result of grain size segregation and gain or loss of

solid and fluid constituents in transit. An example is given by De Blasio et al. (2005). In simulating the giant Storegga slide (west coast of Norway) they found that the shear resistance of the soil was substantially decreased during the flow. According to the authors this is due to the combination of shear wetting (water incorporation into the sediment) and hydroplaning. Models that employ a fixed rheology cannot yield accurate interpretations of these phenomena.

Rheometrical measurements of yield strength and rate dependent shear resistance have limited relevance to debris-flow mechanics. For subaerial debris flows an alternative to fixed-rheology models is provided by a Coulomb mixture theory model (Iverson, 1997; Iverson, 2001), which can represent variable interactions of solid and fluid constituents in heterogeneous debris flow surges with high friction, coarse-grained heads and low friction, liquefied tails. In the case of subaqueous debris flows rheology plays a different role, since a large amount of the energy dissipated during the flow is connected with the drag. This topic will form dominant part of the present work and will be discussed in depth in chap (§ 5.3.3).

Chapter 3

3 Application of PIV technique to the study of subaqueous debris flows

Quantitative imaging (QI) techniques are a class of optically-based laboratory measurement techniques employed in experimental fluid mechanics. This chapter presents an overview of QI techniques, with particular focus on particle image velocimetry (PIV) and its application to debris flow experiments.

Section 3.1 presents a brief introduction to QI techniques and gives a basic overview of the fundamentals of particle image velocimetry, while section 3.2 shows how the PIV technique has been applied in the experiments reported in this thesis.

3.1 Introduction to Particle Image Velocimetry

In the last two decades, thanks the great advances in computing and image capture technologies, quantitative imaging techniques have become the methods of choice when attempting to interrogate laboratory flows.

An important aspect of the emerging dominance of QI techniques is their ability to capture the proprieties of the whole field: $\vec{u}(x,z)$ (velocity field), $\vec{w}_y(x,z)$ (vorticity field), $\overrightarrow{\overline{u'w'}}(x,z)$ (Reynolds stress field) and $\vec{\varepsilon}(x,z)$ (turbulent dissipation field). Researchers interested in spatial gradients have traditionally attempted to employ single-point measurement technologies at two or more spatial locations but on different experimental runs, while QI techniques are capable to capture a spatial field under the identical free surface conditions allowing accurate instantaneous gradients to be determined from a single run. It should be noted that there has recently been a growing use of three dimensional scalar QI techniques; these are generally based on scanning a laser light sheet through a volume.

3.1.1 The principles of Quantitative Imaging techniques

QI techniques can be broken into several fundamentally different types according to the function of the seeding, viz.: flow seeded with discrete particles, flow seeded with continuous tracers and unseeded flows. The differences are briefly summarised in the following.

In the first group, particles-based techniques, the instantaneous fluid velocities can be measured at successive instant in time recording the position of images produced by small tracer particles suspended in the fluid. These techniques fall into two broad categories, with different development paths: PIV, where the velocity is extracted by looking at the movement of a group of particle images, and PTV, where the velocity is extracted by looking at the movement of a single particle image.

- *Particle streak velocimetry (PSV)* - Techniques where the image exposure time is long relative to the time a particle occupies a point in the space. The result is images of particle streaks, where the length of the streaks can be measured to calculate the velocity.

- *Laser speckle velocimetry (LSV)* - Employs a sufficiently high seeding for a frame to capture predominantly overlapping and interfering particles images, which can be thought of as an intensity texture of speckle field[8]. The velocity is extracted by correlating (auto- or cross-correlation analysis) the speckle pattern in a small subregion with that in another subregion.
- *Particle image velocimetry (PIV)* - The seeding density is moderate, such that the nearest neighbour distance of particle is in the order of a few particle diameters, ensuring that all small subregions have several distinct discretely imaged particles within them, and relatively few particles that overlap. The velocity field can be extracted by tracking via auto- or cross-correlation analysis.
- *Particle tracking velocimetry (PTV)* - The seeding density is sufficiently low that a frame captures predominantly non-overlapping or interfering particle images and the velocity can be extracted by tracking the motion of individual particles over known time.

LSV and PIV are essentially different operating modes of the same technique. The velocity field is generally determined on an interrogation grid and each velocity vector is the average velocity of many particles contained in a small volume of fluid. This is in contrast to PTV and PSV, where velocity vectors are determined from the individual particle images or from streaks produced by a single particle at random locations.

The tracerless techniques rely on measuring either the concentration or displacement of a chemical tracer substance added to the flow.

- *Laser induced fluorescence (LIF)* - The flow is seeded with a dilute fluorescent chemical tracer that will fluoresce proportionally with its local concentration.

[8] The speckle field is intended as a image where the particles are not singularly recognisable, but they form a well defined texture.

- *Scalar image velocimetry (SIV)* - The gradient in intensity information (differences of colour gradient in the image) recorded in images is treated like speckle in LSV and correlation-based analysis is used to extract velocity field information.

Attention will now focus on PIV techniques and their applications. When we talk about PIV we refer generally to a seeded flow with particles that can be considered passive tracers, illuminated with a light source, generally a laser, that is shaped with optical components into a light sheet. The light sheet is quasi two dimensional in the sense that it is thin in the direction orthogonal to the plane of motion. An imaging device, usually a high speed camera, collects the images of the particles as they pass through the light sheet. Computer-controlled timing signals sent simultaneously to the digital camera and the light source are usually employed to synchronise the system and collect images at the desired instant.

There are two general ways in which particle images can be collected: the single exposure of multiple images, where the velocities are calculated by auto-correlation, and the multi-exposure of single images where the fundamental technique is cross-correlation analysis. As the multi-exposure of single images and cross-correlation techniques are the ones used in this thesis-work, the discussion we will restricted to those cases.

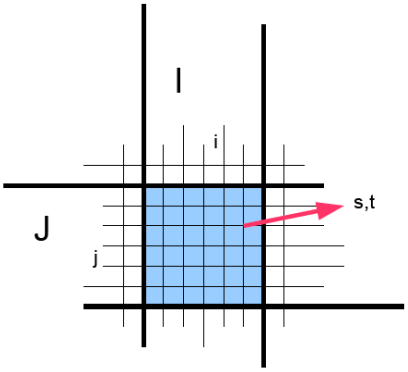

Figure 3.1 Example of a subwindows and the indexing system

3.1.2 PIV and the cross-correlation

Let's assume we have collected an image pair (I' and I'') where the second image was captured a a know time, Δt, after the first image. Subsequently we divide both images into smaller non-overlapping square subwindows (or interrogation cells) with side length usually equal to $N = 2^n$, where n is integer. We then compare each subwindow in the first image with the corresponding subwindow in the second image. We shall hereafter let $I'_{I,J}$ denote subwindows I,J in the first image and $I''_{I,J}$ the corresponding subwindow in the second image.

We now aim to see if it is possible to identify a displacement of the pattern in $I'_{I,J}$. To do this we can evaluate the squared Euclidean distance $D_{I,J}$ between the two subwindows I,J (see Eq. [3.1]).

$$D_{I,J}(s,t) = \sum_{i=0}^{N}\sum_{j=0}^{N}\left[I'_{I,J}(i,j) - I''_{I,J}(i+s, j+t)\right]^2 \qquad [3.1]$$

where the subscript *i,j* indicates the pixel location within subwindow $I_{I,J}$ and *s,t* is the two dimensional cyclic lag at which the squared Euclidean distance is being computed.

This means that for every possible overlap of the subwindows, we calculate the sum of the squared distance between them, in other words we are looking for the position where the subwindows are the "least-unlike".

If we expand the square parenthesis on the right hand side of the formula we get the equation [3.2].

$$D_{I,J}(s,t) = \sum_{i=0}^{N}\sum_{j=0}^{N}\Big[\left(I'_{I,J}(i,j)\right)^2 - 2\cdot\left(I'_{I,J}(i,j)\right)\cdot\left(I''_{I,J}(i+s,j+t)\right) + \left(I''_{I,J}(i+s,j+t)\right)^2\Big] \qquad [3.2]$$

We should notice that the first term, $\left(I'_{I,J}(i,j)\right)^2$, is merely a constant since it does not depend on *s* and *t*. The last term, $\left(I''_{I,J}(i+s,j+t)\right)^2$, is dependent just on the second image. Therefore, only the middle term actually deals with both the images I' and I'' and as a matter of fact it is usually referred to as cross-correlation (Eq. [3.3]).

$$R_{I,J}(s,t) = \sum_{i=0}^{N-1}\sum_{j=0}^{N-1} I'_{I,J}(i,j) I''_{I,J}(i+s,j+t) \qquad [3.3]$$

Using the Wiener-Kinchin theorem, R can be calculated in the spectral domain [3.4], (Raffael et al, 1998; Gonzales & Woods, 1992).

$$R_{I,J}(s,t) = FFT^{-1}\left[FFT^{*}\left\{ I'_{I,J}(i,j) \right\} FFT\left\{ I''_{I,J}(i+s, j+t) \right\} \right] \qquad [3.4]$$

where *FFT* and FFT^{-1} are the Fourier and the inverse Fourier transform operators and the star denotes a complex conjugate. The advantage of using Eq.[3.4] instead of Eq.[3.3] is that computation via *FFT* is faster than the direct computation, but it also requires the interrogation cell size to be $N = 2^n$, where *n* is an integer.

The calculated correlation plane, $R(s,t)$, contains a peak corresponding to the displacement $(\hat{s},\hat{t})$ for which the subwindows are the "last-unlike"; therefore $(\hat{s},\hat{t})$ is the average displacement of the tracer particles in the considered subwindows over the time Δt.

In many cases it may be advantageous to be able to evaluate the degree of correlation between two subwindows. The maximum value in the correlation plane is a relatively important parameter to estimate since it is a direct measure of the degree of match between the subwindow patterns. The ratio between the highest peak and the rest of the correlation plane will furthermore provide information on the quality of the match compared to the noise. In order to evaluate these quantities we need to normalise the correlation in equation [3.3]. One function that calculates a normalised correlation is the *full correlation coefficient* or *covariance function*, defined as in equation [3.5].

$$\hat{R}_{I,J}(s,t) = \frac{\frac{1}{N^2} \cdot \sum_{i=0}^{N-1}\sum_{j=0}^{N-1}\left[I'_{I,J}(i,j) - \overline{I}'_{I,J} \right]\left[I''_{I,J}(i+s, j+t) - \overline{I}''_{I,J} \right]}{\left[\sum_{i=0}^{N-1}\sum_{j=0}^{N-1}\left[I'_{I,J}(i,j) - \overline{I}'_{I,J} \right]^2 \sum_{i=0}^{N-1}\sum_{j=0}^{N-1}\left[I''_{I,J}(i+s, j+t) - \overline{I}''_{I,J} \right]^2 \right]^{1/2}} \qquad [3.5]$$

where $\overline{I}'_{I,J} = mean\left(\overline{I}'_{I,J}(i,j)\right)$ and $\overline{I}''_{I,J} = mean\left(\overline{I}''_{I,J}(i,j)\right)$. The denominator can be easily calculated by the use of Fourier transform (Eq.[3.4]) and is usually approximated by $N^2\sigma\left(I'_{I,J}\right)\sigma\left(I''_{I,J}\right)$ where $\sigma\left(I'_{I,J}\right)$ denotes standard deviation, defined as Eq.[3.6], and is calculated prior to $\hat{R}(s,t)$.

$$\sigma\left(I'_{I,J}\right) = \left[\frac{1}{N^2-1}\sum_{i=0}^{N-1}\sum_{j=0}^{N-1}\left(I'_{I,J}(i,j) - \overline{I}'_{I,J}\right)^2\right]^{1/2} \qquad [3.6]$$

In this way we can use the peak height in the correlation plane as a measure of how good the correlation was. A value close to 1 will indicate a very high degree of match between our windows, while a value of 0 will indicate the opposite. The underlying assumption for this approximation is that our pattern is evenly distributed, meaning that the standard deviation $\sigma\left(I_{I,J}\right)$ does not change if we vary *s* and *t*. Another advantage in the use of the normalised correlation is that the last term of equation [3.2] does not have to be non-constant in the passage from Eq.[3.1] to Eq.[3.3].

In situations where the mean displacement field is unknown *a priori*, an iterative interrogation procedure can be used to increase both the quality and accuracy of the PIV measurement. The reasoning behind such an interrogation procedure is quite simple: by offsetting the second interrogation window I'' by the local mean integer displacement, one can dramatically improve the accuracy of the correlation calculation (Cowen and Monismith, 1997; Westerweel et al., 1997; Raffel et al.,1998).

The local window shift is usually adaptively determined in the following way: the computation starts by using an initial interrogation cell size I_i which is larger than the final size I_f by a factor of 2 or 4, or possibly higher. In the initial pass the window shift is zero for the whole image. The calculated displacement field of the initial pass is post-processed (§ 3.1.3) and a complete replacement of all disabled vectors is operated. In the next pass, the

interrogation cell size is halved, and the interrogation windows are shifted about the centre according to the estimated displacement of the previous pass. When the displacement field has been determined for the locally shifted interrogation areas, the applied shifts are added to obtain the true particle displacements and the displacement field is post-processed as above and is used to shift the interrogation windows of the next pass, where the cell size is again halved. This is repeated until the final cell size is reached.

The advantage of using an initial pass with a larger interrogation cell size is that the estimated displacements are much more reliable for the larger cell size, due to the higher particle image density. Another benefit is that larger particle displacements may be used, which implies an increased dynamic range of the measurements. The maximum displacement that can be measured for fixed interrogation areas using FFT-based correlation Eq.[3.4] is $N_i/2$, where N_i indicates the dimension of the initial interrogation window. Even though the theoretical upper limit for the particle displacement is $N_i/2$, the practical limit for reliable measurements is $N_i/4$ (the "quarter rule"), Keane and Adrian (1990), and the optimum particle displacement would be of the same order as the final interrogation cell size.

3.1.3 Data filtering and sub-pixel displacement estimation

Once the correlation function $\hat{R}_{I,J}(s,t)$ is found, the integer location of the highest peak $(\hat{s},\hat{t})$ in the correlation plane gives an estimation of the most likely average particle displacement within the interrogation area.

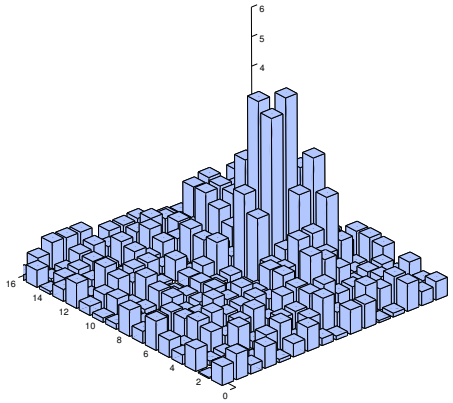

Figure 3.2 Example of the correlation plane $\hat{R}_{I,J}(s,t)$.

For non-zero particle image diameters the width of the correlation peak is greater than one pixel, therefore to get a more accurate sub-pixel estimation of the peak location, it is possible to interpolate between the correlation values closest to the peak. The three most commonly used estimators are *Centre of Mass*, *Parabolic* and *Gaussian* fit.

Since QI techniques generally satisfy the condition for narrow covariance peaks, three-point sub-pixel estimators are generally sufficient. Let us define R_0 as the highest value of the correlation plane, and R_{-1} and R_{+1} the values of the two nearest pixels in the vertical (or horizontal) direction. The fractional part ε of the displacement can be calculated as follows (Eq. [3.7], [3.8] and [3.9]).

$$\varepsilon = \frac{R_{+1} - R_{-1}}{R_{+1} + R_0 + R_{-1}} \qquad \textit{Centre of Mass} \qquad [3.7]$$

$$\varepsilon = \frac{R_{+1} - R_{-1}}{2\left(R_{+1} - 2R_0 + R_{-1}\right)} \qquad \textit{Parabolic} \qquad [3.8]$$

$$\varepsilon = \frac{\ln R_{-1} - \ln R_{+1}}{2\left(\ln R_{-1} - 2\ln R_0 + \ln R_{+1}\right)} \qquad \textit{Gaussian} \qquad [3.9]$$

Even if all the steps in the image acquisition and processing sequence are optimised, there is a finite probability that the highest correlation peak does not correspond to the true displacement. One then obtains a spurious or false vector. Reasons for the occurrence of spurious vectors include a locally low particle image density, or disturbing background noise from reflections.

There are three fundamental approaches to test the validity of an individual vector (Westerweel, 1993; Westerweel, 1994; Nogueira et al., 1997):

- *Signal quality tests* - look at specific properties of the images, such as the magnitude of the correlation peak relative to the magnitude of the background noise in the correlation plane, to test the validity of a vector.
- *Spatial consistency tests* - compare each vector with certain properties calculated from the local neighbourhood of vectors (local filtering), or the entire vector field (global filtering).
- *Temporal consistency tests* - are similar to spatial consistency tests with the exception that the vector whose quality is being tested is compared either with a statistic applied locally in time (e.g., acceleration) or globally in time (e.g., its distance from the mean relative to the standard deviation).

3.2 Application of PIV techniques to SAFL experiments

As described above (§ 3.1.1), particle image velocimetry is an optical method used to measure velocities and related properties in fluids. Usually the fluid is seeded with particles which are generally assumed to faithfully follow the flow dynamics. It is the motion of these seeding particles that is used to calculate velocity information. Typical PIV apparatus consists of a camera (normally a digital one), a high power laser, an optical arrangement to convert the laser output light to a light sheet, and the fluid/gas under investigation.

The development of new image acquisition technologies, together with their becoming far less expensive, allowed a rapid diffusion of the PIV techniques into other fields than the fluid dynamics of water or gases. One of those fields is granular flow dynamics. Spinewine et al. (2003) developed a three dimensional PIV technique, based on Voronoï triangles, to study the motion of granular flows. Pouliquen (2004) and the Groupement De Recherche Milieux Divisés (2004) made extensive use of this measurement method to characterise the behaviour of dense assemblies of dry grains. Similar applications can be found in Biancardi et al. (2005a, 2005b) and in Barbolini et al. (2005). All these techniques are based on direct recognition of the particles; no seeding is necessary.

It was these experiments that led to the idea of applying the PIV technique to subaqueous debris flows[9]. Moreover was chose to associate this technique with an advanced experimental apparatus (§ 2), comprising four synchronised high speed digital cameras. This gave us the capability to undertake a really comprehensive characterisation of the flow dynamics.

[9] Previous researcher carried out some experiments of submarine debris flow using high speed cameras (Ilstad et al., 2004b), but the particles velocities measurements were carried out manually.

The following paragraphs describe the four stages of image and data analysis that were applied in the experiments:

- *Image acquisition*
- *Interrogation*
- *Data validation*
- *Data analysis*.

3.2.1 Image acquisition

The first step is to acquire the images. This is probably the most important step, too, as without high quality imaging good results are unattainable. It is possible to repeat the calculations with a different algorithm and parameters, but it would be extremely time consuming and expensive to have to repeat the experiments.

The choice of the cameras, especially with respect to resolution and frame rate, is described in detail in Chapter 2.2.4. High speed videos consist of 4000 images recorded with and acquisition frequency of 240 Hz and a resolution of 600 x 200 pixels. In order to save calculation time and avoid a collection of useless data, velocities are only calculated for the first 1000 frames (4.16 seconds) from the start of the debris flow. After this time the phenomena can be considered to be over.

3.2.2 Interrogation and peak finding

There are many non-commercial PIV programs in existence today whit excellent capabilities for research purpose, with many options for users at different levels. The three which are probably the most widely available and

used are URAPIV, MatPIV and Mpiv; all of them are distributed as Matlab toolbox.

URAPIV has been developed by a group of researchers at the Faculty of Civil and Environmental Engineering of the Technion (Israel Institute of Technology). Mpiv was written in Matlab by Nobuhito Mori and Kuang-An Chang and consists of two main programs, one for image processing and the other for post-processing, and several external functions. MatPIV was written by J. Kristian Sveen, Department of Applied Mathematics and Theoretical Physics, University of Cambridge (Sveen and Cowen, 2003; Sveen, 2004) has been under development since 1998 and today has around 350 registered users in addition to an unknown number of unregistered ones.

After a short evaluation of these programs, MatPIV appeared to be by far the largest and most versatile. It is supplied with source code under the terms of the GNU general public license manager which means that personal modifications to the code are allowed.

MatPIV consists of 37 Matlab files, is capable of performing PIV calculations with different algorithms and includes four different filters in order to remove the so-called spurious vectors.

We applied an iterative interrogation procedure at every couple of consecutive images; this helped us to improve both the quality and the accuracy of the PIV measurement (§ 3.1.2). To implement that procedure we wrote a script in Matlab that would open two consecutive images of the recorded video, apply MatPIV to them, filter, and write the results in a mat file.

The dimensions of the initial interrogation windows it are function of the maximum displacement of the particles between two consecutive frames. The maximum displacement that can be measured is Ni/2, where Ni indicates the dimension of the initial interrogation windows. The maximum velocity recorded in our experiments is less than 1 m/s, corresponding to a displacement between two consecutive frames of about 37.5 pixels. Therefore we chose to start the computation using an initial 64x64 pixels interrogation cell size, and continued the calculation with an adaptive windows scheme. This process assumes that, after each step, the interrogation windows are shifted about the centre,

according to the estimated displacement of the previous step, appropriately filtered by a median-filter.

The minimum velocity that can be measured is about 0.025 m/s, corresponding to a pixel displacement. In order to increase the precision of the method we estimated the sub-pixel displacement by Gussian peak-fit (§ 3.1.3).

3.2.3 Data validation

After having performed the calculation it is necessary to filter the velocity in order to remove the so-called spurious vectors. This has been done using a sequence of four different filters.

- *Signal to noise ratio*: The output from MatPIV includes the signal to noise (SnR) ratio. All the vectors with a SnR lower than the threshold are replaced with an NaN (not a number). A threshold equal to 1.3 has been used in agreement with Keane and Adrian (1992).
- *Peak height filter*: removes all the vectors where the normalised peak height is lower than 0.5. All the invalid vectors are replaced with an NaN.
- *Global histogram operator*: the global histogram operator is a filter that removes vectors significantly larger or smaller than the majority of vectors. In particular we have chosen to create an acceptance region three times larger the velocity standard deviation in x and y directions.
- *Local filter*: we compare each vector belonging to the velocity field to the eight vectors surrounding it. A vector was rejected if larger than the average plus twice the standard deviation or smaller than the average minus twice the standard deviation.

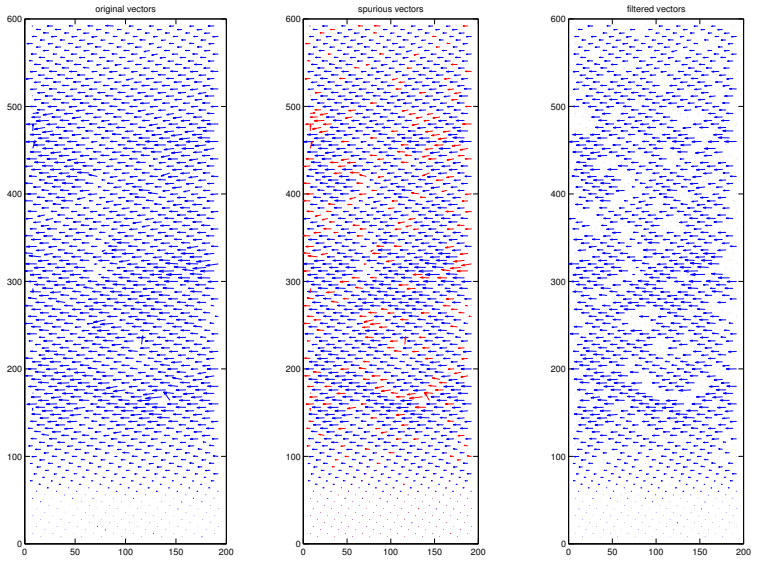

Figure 3.3 Detection of spurious vectors

It has to be noted that the filtering process can bias the results. In particular the *local filter* can act as a low pass filter with a non negligible effect on the derivative quantities of the motion field.

For this reason the parameters that regulate the filters have been properly calibrated in order to reduce the effect on the final result. It has to be noted that in this work

After the filtering process the spurious vectors are substituted with NaNs. The last step consists in overlapping those NaNs. First, we sort all the spurious vectors based on the number of spurious neighbours. Then we start interpolating the vectors that have as few neighbouring outliers as possible, looping until no NaN are left. The result of the process is show in Figure 3.4.

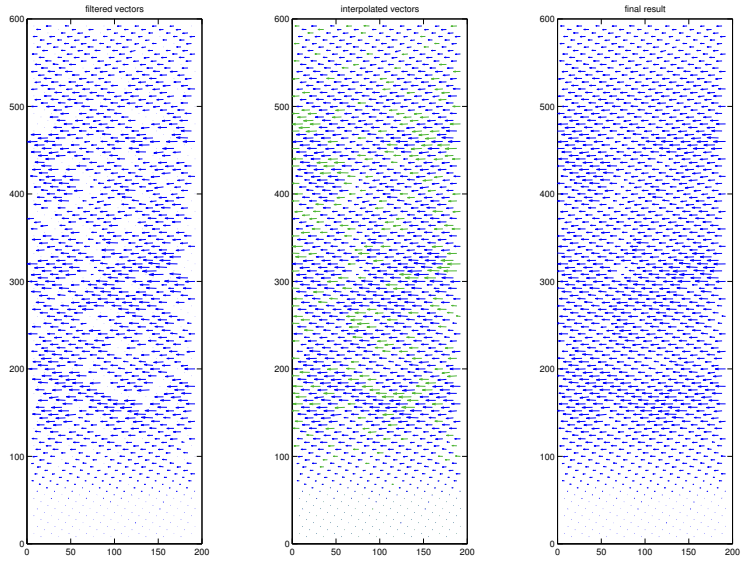

Figure 3.4 Vectors interpolation procedure.

Chapter 4

4 Image data analysis

The aim of this chapter is to describe and highlight the most relevant characteristic features of debris flows as measured with high speed cameras. The collected data have been surveyed and compared to data reported in literature.

A critical process of data reduction enabled the most relevant flow properties to be obtained for different chute sections and sediment mixtures. The chapter is divided into two parts. The first part focuses on velocities, velocity profiles and all the data connected with the high speed cameras, while the second concerns the deposition and its dependence on mixture rheology.

For easier comprehension, some images taken during the experiments are presented in the following pages. In particular Figure 4.1 shows the whole debris flow wave recorded with a digital SLR camera, while Figure 4.3 is a collage of frames taken with the high speed camera. It is important to note that the high speed cameras record only the debris flow layer and not the whole wave.

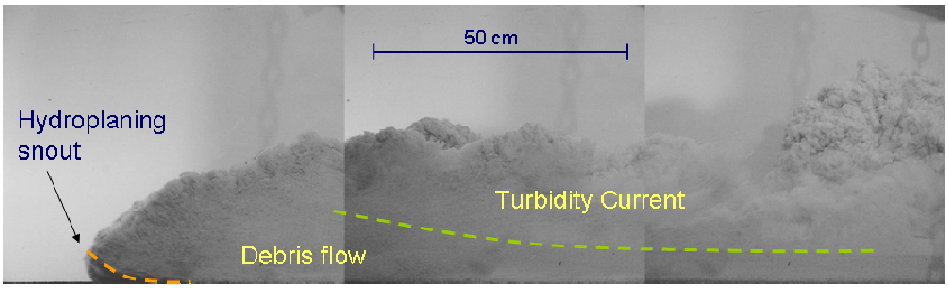

Figure 4.1 Example of debris flow wave (15% clay). The picture is the composite of three consecutive photos taken with a SLR camera.

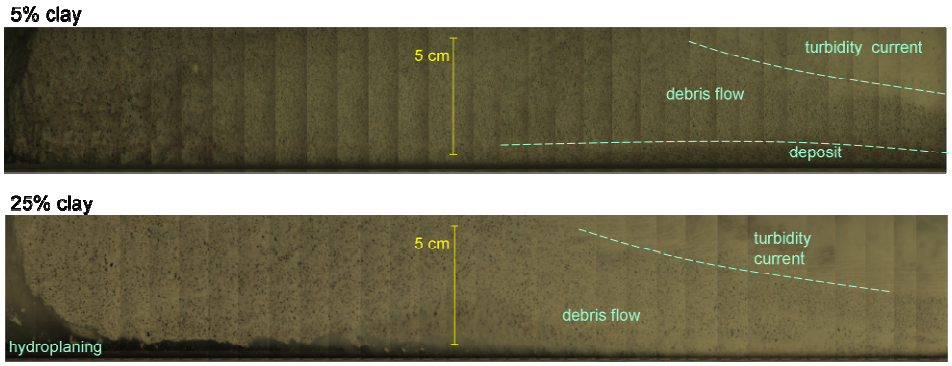

Figure 4.2 Composition of frames from high speed cameras. Figs. A) and B) refer respectively to the 5% and 25% clay slurries. The high speed cameras record the basal layer of the wave that corresponds to the debris flow.

4.1 Velocities and velocity profiles

The velocity measurements were carried out using four high speed cameras located at 3.60, 4.10, 7.30 and 7.80 metres downstream from the gate. The cameras were synchronised with the gate opening. For more details see Chapter 3.

4.1.1 Front velocity

High speed camera sequences consist of 4000 images, commencing as the gate opens. The frame in which the debris flow is first captured by camera *CN* is defined $FR(1)_{CN}$.

The ability to single out $FR(1)_{CN}$ provides a two-fold advantage. It both allows a saving in calculation time - PIV is applied starting from $FR(1)_{CN}$ - and yields the debris flow front position versus time (Figure 4.3).

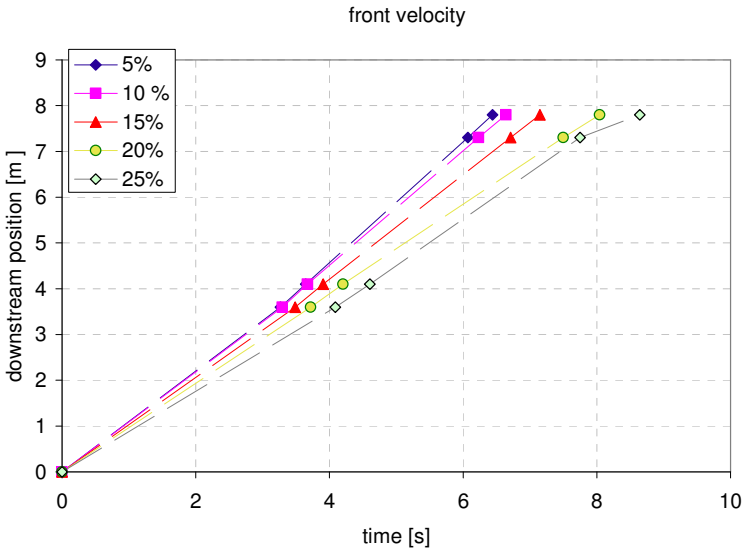

Figure 4.3 Front position versus time. Reported data are an average of two experiments for each concentration.

Time zero (Figure 4.3) corresponds to the gate opening. As shown in Figure 4.3 and Figure 4.4, in each case there is an acceleration phase up to the first camera. After the acceleration phase, different types of behaviour of the front velocity can be recognised.

The front velocity remains almost constant for the most sandy mixture, while in all the other cases the velocity shows a peak between the first and the second

camera (3.6 - 4.1 meters downstream the gate) and than diminishes downstream (Figure 4.4).

It has to be noted that the velocity after the second camera (4.1 meters downstream the gate) diminishes very slightly, about 3% of the average velocity. This means that the front velocity is stationary, at least as a first approximation.

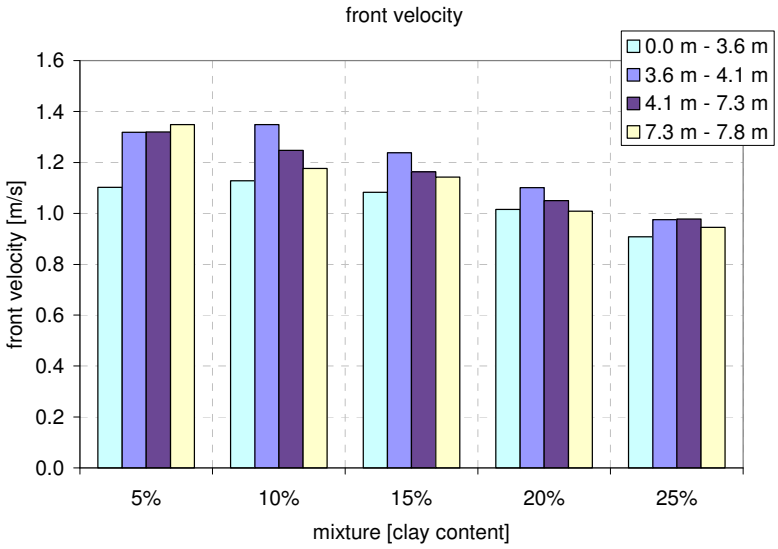

Figure 4.4 Front velocity. Reported data are an average of two experiments for each concentration.

Figure 4.4 shows that the front velocity depends on the clay content. The front of the sandiest mixture moves 30% faster than the clay-rich ones.

The differences in front velocities were expected to be larger because of the differences in rheological properties (§ 2.3.3). In the range of flow rates considered here, the shear stress of the 25% clay slurry is almost six times greater than that measured for the 5% and 10% clay mixtures.

This is in agreement with the findings of Mohrig et al. (1998). When varying the viscosity of the slurry (but using a constant clay content), they found that

rheology played only a secondary role for subaqueous flows compared to subaerial flows. However, calculating the velocity between the two camera pairs (C1 and C2, C3 and C4) reveals a more complex behaviour of the subaqueous flows, probably related to frontal hydroplaning (Figure 4.5).

In marked contrast to this, using the same mixture and the same experimental setup in the subaerial environment, Breien et al. (2007) found that the front velocity decreased significantly (up to 50 %) as a function of the clay content. This evidence demonstrates that the effect of the ambient fluid is fundamental on the dynamics of debris flows.

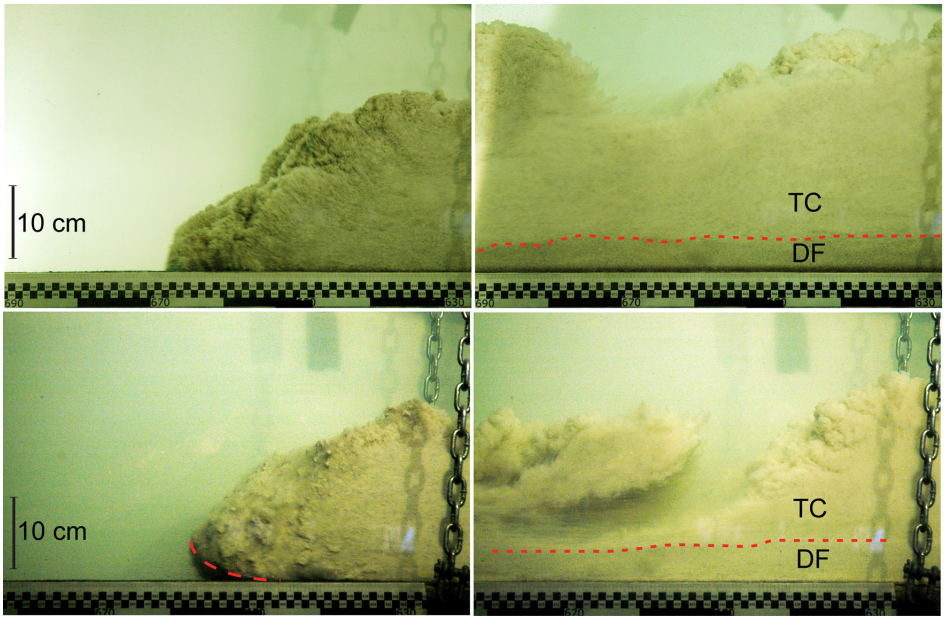

Figure 4.5 Images taken during the experiments with a standard SLR digital camera. The upper one refers to the 5% slurry, the lower one to the 25% slurry.

4.1.2 Velocity field

The first thousand frames after the passage of the front - i.e. after the *starting frame* - have been analysed with the procedure described in detail in Chapter 3. The result is the flow field $u_{i,j;k}$; $v_{i,j;k}$, where *u* and *v* are the horizontal and vertical velocity respectively; the subscript *i* denotes the row and goes from 1 to 147 while the subscript *j* denotes the columns and goes from 1 to 47. The distance between each row and each column is 0.444 mm. Figure 4.6-a shows an example of flow field.

The first characteristics that can be extracted from the velocity field are *streamlines*[10] and *magnitude*, i.e. the modulus of the velocity vector at each point (Equation [4.1]).

$$m_{i,j} = \left(u_{i,j}^2 + v_{i,j}^2\right)^{1/2} \qquad [4.1]$$

Instantaneous velocity data in a 2D domain allows the computation of any quantity based on spatial derivatives. Vorticity is reported here as an example. Vorticity (Eq. [4.2]) can be related to the amount of "circulation" or "rotation" (or more strictly, the local angular rate of rotation) in a fluid:

$$w = \frac{\partial v}{\partial x} - \frac{\partial u}{\partial y} \qquad [4.2]$$

Several numerical schemes exist for performing this calculation. In the present case the least squares operator (Eq. [4.3]) was used. It reduces the effect of fluctuations and this is one reason why this method is often used with PIV measurements.

[10] A streamline is a path traced out by an ideal mass-less particle as it moves with the flow; in every point along the path the velocity vector is tangent to the path.

$$w_{i,j} = \frac{1}{12\Delta X}\left(-v_{i+2,j} + 8v_{i+1,j} - 8v_{i-1,j} + v_{i-2,j}\right) - \frac{1}{12\Delta Y}\left(-u_{i,j+2} + 8u_{i,j+1} - 8u_{i,j-1} + u_{i,j-2}\right) \quad [4.3]$$

While computing the derivatives it is necessary to be careful since the velocity gradients measured by PIV are grid dependent and also subject to low-pass filtering and noise.

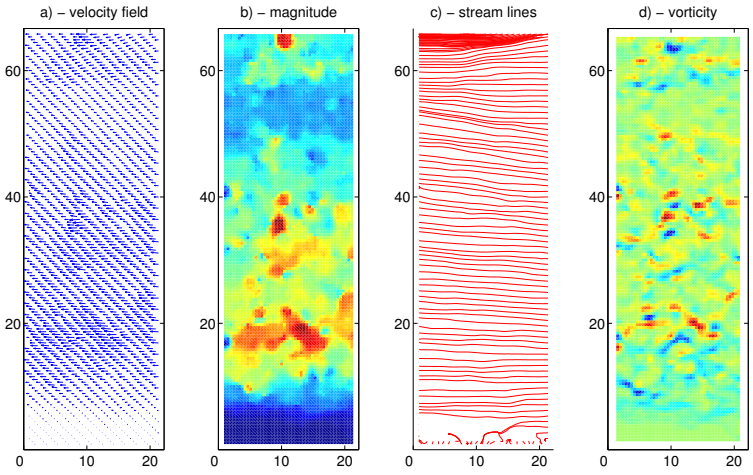

Figure 4.6 Examples of velocity field, velocity magnitude, steamlines and vorticity. Values are in millimetres.

4.1.3 Velocity profile

Instantaneous velocity data in a 2D domain are very useful for an immediate visualisation of velocity field and allow the computation of any quantity based on spatial derivatives. On the other hand the elaborated images contain an

enormous amount of data - more than 50000 frames have been processed - that need to be reduced in order to have a global vision of the flow characteristics and to be able to compare the various experiments. To do this a set of instantaneous velocity fields can be used for ensemble averaging. Conventional statistic quantities such as mean velocities can be computed for each Cartesian component.

Debris flows are not stationary processes; velocities vary in space (along the chute) and in time (between frames). When calculating averages it is necessary to take this into account. The frames are very narrow compared to the debris flow length, thus it is possible to consider velocity variations along a frame as negligible. It is also necessary, in order to calculate averaged values, to define the correct temporal domain that allows the process to be considered stationary, i.e. a time length in which velocity variations are negligible.

We based the computation of this time length on the time autocorrelation function of the velocity for different mixtures compositions. Autocorrelation (Eq. [4.4]) is a mathematical tool frequently used in time domain signals. More precisely, it is the cross-correlation of a signal with itself. Informally, it is a measure of how well a signal matches a time-shifted version of itself, as a function of the magnitude of the time shift. In other words, this function explains how the velocity at a fixed position and time t are related to velocity in the same position at a previous time $t-\tau$ (for a time lag $\tau=0$ the autocorrelation function is equal to one).

$$R_{uu}(n)=\frac{\sum_{n}\overline{u}_{i,j;k}u_{i,j;k+n}}{\sum_{n}\overline{u}^{2}_{i,j;k}} \qquad [4.4]$$

Figure 4.7 shows the normalised autocorrelation function for the cases with 5% and 25% clay content.

The calculation has been performed for the most critical part of the flow - the front - where velocity variations are more evident. For both the slurries the

autocorrelation value goes up to 0.1 in about 0.1 second, corresponding to 24 frames.

In this work the limit of $R_{uu} = 0.4$ has been fixed in order that two velocities can be considered correlated (Fabio De Blasio, pers. comm.). This value corresponds to a time shift of 0.05 second.

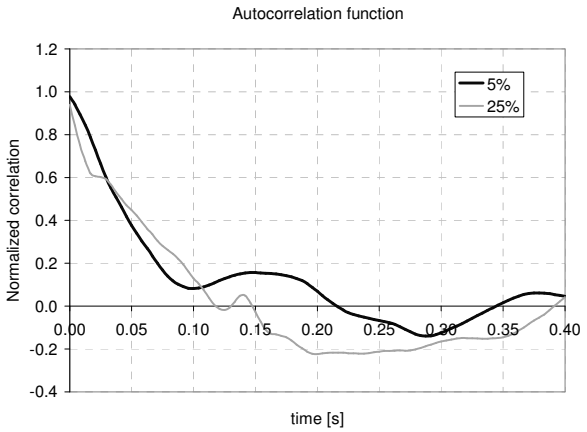

Figure 4.7 Time autocorrelation function for the 5% and 25% clay slurries.

Since autocorrelation is a symmetrical function, velocity profiles averaged over 25 frames (equation [4.5]) have been calculated.

$$\overline{U}_{i;\hat{k}} = \frac{1}{25} \sum_{k=\hat{k}-12}^{\hat{k}+12} \overline{u}_{i;k} \qquad [4.5]$$

$$\overline{V}_{i;\hat{k}} = \frac{1}{25} \sum_{k=\hat{k}-12}^{\hat{k}+12} \overline{v}_{i;k} \qquad [4.6]$$

where

$$\overline{u}_{i;k} = \frac{1}{47}\sum_{j=1}^{47} u_{i,j;k} \qquad [4.7]$$

$$\overline{v}_{i;k} = \frac{1}{47}\sum_{j=1}^{47} v_{i,j;k} \qquad [4.8]$$

For $\overline{U}_{i;\hat{k}}$ and $\overline{V}_{i;\hat{k}}$ the standard deviation in the temporal domain is defined as (Eq. [4.9] and Eq. [4.10]).

$$\sigma\left(\overline{U}_{i;\hat{k}}\right) = \left[\frac{1}{24}\sum_{k=\hat{k}-12}^{\hat{k}+12}\left(\overline{u}_{i;k} - \overline{U}_{i;\hat{k}}\right)^2\right]^{1/2} \qquad [4.9]$$

$$\sigma\left(\overline{V}_{i;\hat{k}}\right) = \left[\frac{1}{24}\sum_{k=\hat{k}-12}^{\hat{k}+12}\left(\overline{v}_{i;k} - \overline{V}_{i;\hat{k}}\right)^2\right]^{1/2} \qquad [4.10]$$

Figure 4.8 and Figure 4.9 show the velocity profile evolution versus time for two different slurries (5% and 25% clay content). Profiles start with the debris flow front. They have been taken over a time distance of 0.52 seconds (i.e. there are 125 frames between each plot). Each of the plotted profile is the average of 25 measured profiles, corresponding to a time interval of 0.1 seconds. These two figures refer to measurements taken 7.3 metres downstream from the gate (third camera section) and beside every velocity profile corresponding images[11] have been printed. Vertical velocities are one order of magnitude lower than horizontal ones, hence the attention is focused on the only horizontal velocities.

[11] The term "corresponding images" is intended to denote one of the pairs of images used in the PIV algorithm.

The shear rate for the sandiest slurry (5% clay) is very low - about 5 s^{-1} - and takes about 10 mm. A plug layer develops over the shear layer. There is no sharp separation between debris flow and the overlying turbidity current.

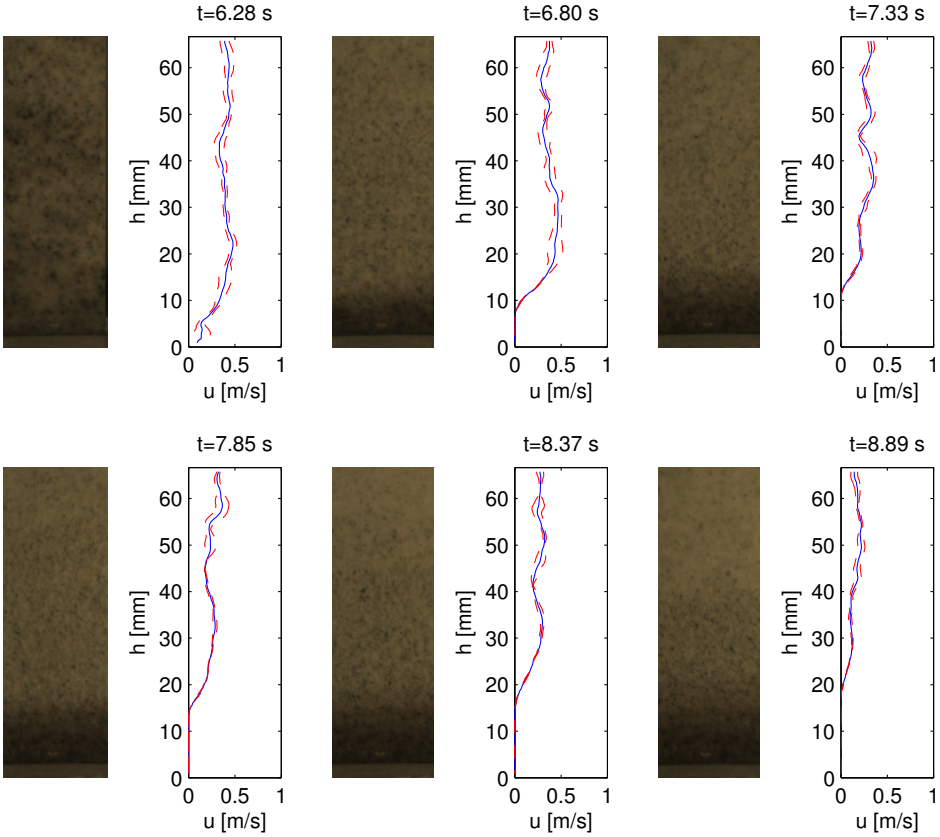

Figure 4.8 Velocity profiles at various time instants taken by the third camera downstream. The plot refers to a 5% clay content experiment (R1_060829_5c). The dashed red line is the standard deviation.

The 25% slurry behaves completely differently. At the flow base there is a layer a few millimetres high with a strong shear rate (~20 s^{-1}). Above the shear layer an essentially rigid block moves with null shear rate. Standard deviation of this part is also null, which means that no velocity variations in time take place

during the considered interval ([4.9]). After the frontal block has passed, the debris flow height diminishes (about 45 mm at t=8.52 s; 40 mm at t=9.04 s) and a turbidity current develops above the debris flow. The PIV technique is not able to measure the velocity in the turbidity current itself because there are not enough tracer particles.

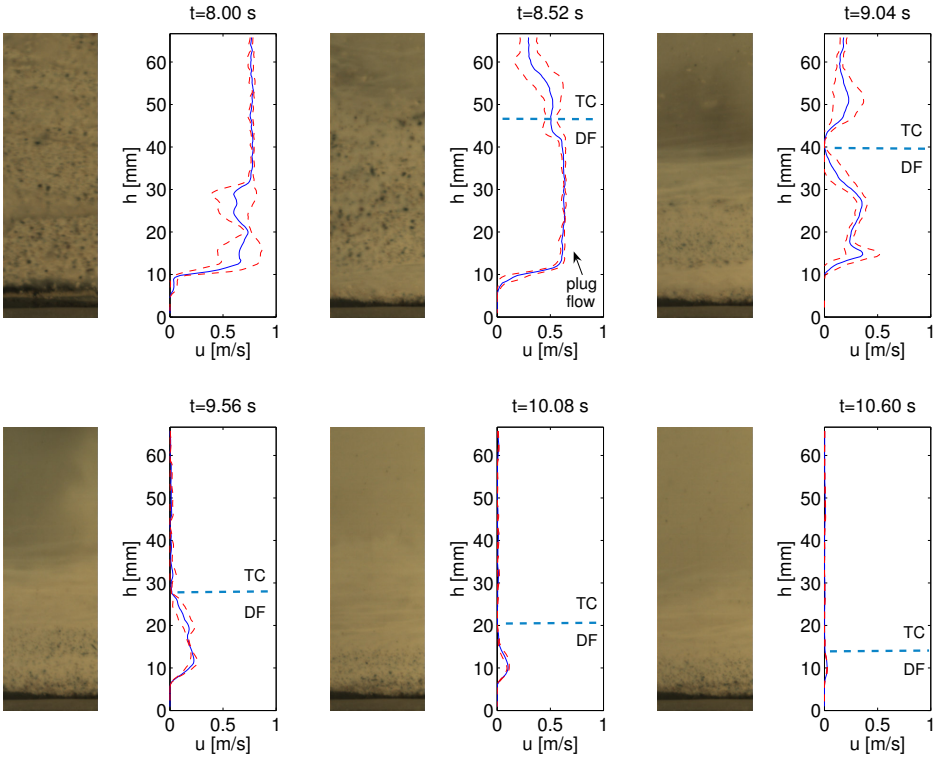

Figure 4.9 Velocity profiles at various time instants taken by the third camera downstream. The plot refers to a 25% clay content experiment (R1_060831_25c). The dashed red line is the standard deviation. An indication of the boundary between debris flow (DF) and turbidity current is shown.

The observed behaviour is compatible with the measured rheologies. The flow is characterised by an un-sheared region or plug layer, where the shear stress does not exceed the yield strength. This region is more consistent in the high clay content mixtures, characterised by a larger value of τ_y (§2.3.3), while it is weak in the case of low clay content. Below the plug layer there is a shear layer where the stress is sufficient to generate a shear flow.

The study of velocity profiles also yields information concerning the deposition layer. The height of the zero velocity zone above the bottom corresponds to the thickness of the deposited bed. In particular, for the 5% clay case it reaches 20 mm at t=8.89, while in the 25% case there is almost no deposition. A more detailed study of deposition is given in section 4.2.

In Figure 4.10 and Figure 4.11 the averaged horizontal velocities $\overline{u}_{i;k}$ [4.7] have been plotted versus flow height and time. The colour shade is proportional to the velocity value. The same colour scale is used in all the images. The figures (Figure 4.10 and Figure 4.11) allow us to have a complete representation of velocity profile variations versus time. A comparison between different experiments is thus immediate.

For the low clay content case the flow looks homogenous. Hence it is possible to distinguish a faster frontal part of the flow and then a slower one, characterised by a gradually diminishing velocity. This contrasts with the clay rich mixture, where the head moves like a rigid body. During the first second there is no variation (reduction) of velocity, after which it very quickly diminishes to a value close to zero. Immediately above the debris flow head a strong turbulence develops. This turbulence is at the base of the formation of the overriding turbidity current. More details can be found in Section 5.2.

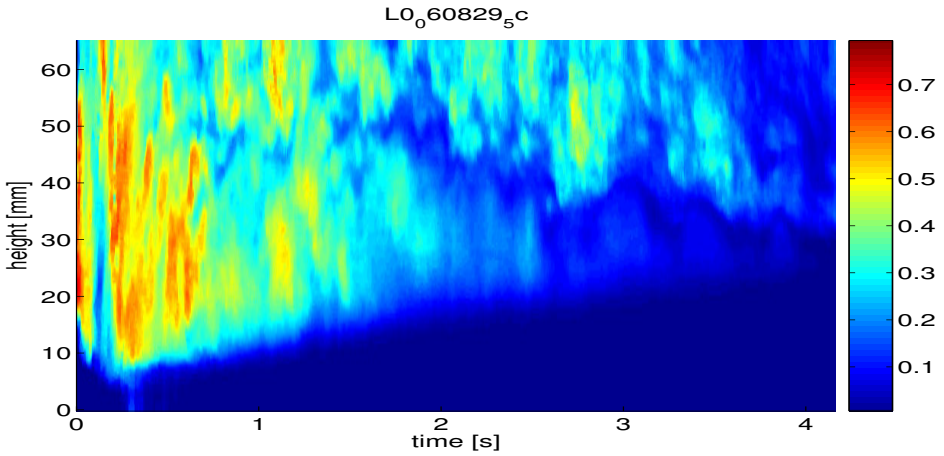

Figure 4.10 Velocity versus time, 5% clay mixture, second camera downstream.

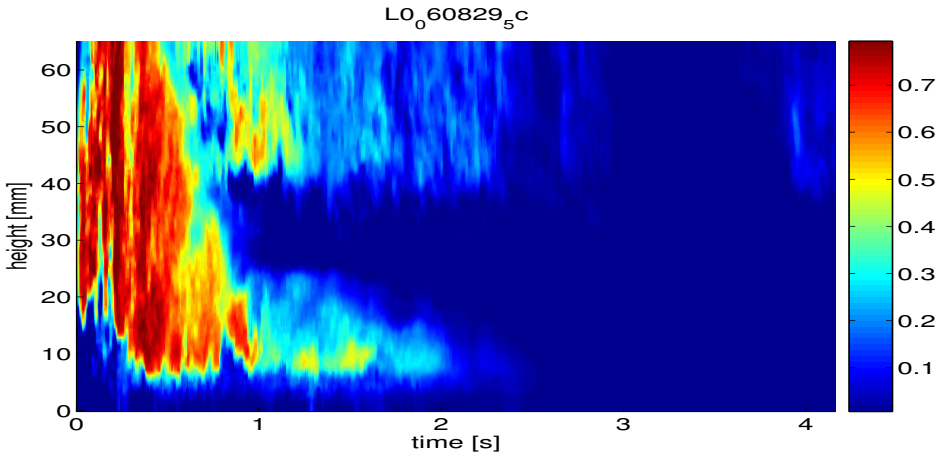

Figure 4.11 Velocity versus time, 25% clay mixture, second camera downstream.

In all the experiment results it is possible to see a kink in the velocity profile; as Figure 4.11 shows, this is more evident for higher clay content mixtures. The kink is not due to a chute defect because it can easily be found in all the measurements sections (the four camera position described in Section 2.2.1).

Moreover the velocity field comparison with the associated images shows that the kink corresponds to the boundary between debris flow and turbidity current.

A Herschel-Buckley fluid flowing in a square-section channel may show death zones (Johnson, 1970) in correspondence of the corners. The same phenomenon probably occurs at the debris flow/turbidity current boundary. This means that the measured velocity in this region will not be representative of the velocity in the middle of the channel section, where the velocity is unlikely to be zero.

Similar velocity profiles were measured by Felix and Peakall (2006). They used ten multiplexed Ultrasonic Doppler Velocimetry Profiling (UDVP) probes (Best et al., 2001) placed in the middle of the chute. A diminishing velocity magnitude was observed corresponding to the boundary between debris flow and turbidity current. It should be noted that the spatial resolution of the UDVP is only a tenth of that used in PIV, which means that the Doppler is not able to give a detailed view of the kink in the velocity profile.

In order to measure velocity in the middle of the channel with a large enough spatial resolution it would be necessary to use a laser sheet and tracer particles with the same refraction index as the ambient fluid. Some researchers (Groupement de Recherche MIDI, O. Pouliquen, F. Radjai and D. Bideau) are working towards this, but at present it is not possible to use this technique to reproduce fluids with complicated rheologies, such as in the case considered here.

4.1.4 Average flow velocity

The average velocity of the flow $\overline{U}_k$ (Equation [4.11]) allows a quick comparison between the experiments.

$$\overline{U}_k = \frac{1}{n_f} \sum_{i=1}^{n_f} \overline{u}_{i;k} \qquad [4.11]$$

Where n_f is the number of cells (PIV subwindows) occupied by the flow. In particular, a cell is considered occupied by the flow if the velocity of the cell is larger than a threshold velocity equal to 1/100 of the average velocity of the flow. Otherwise the cell is part of the deposit layer. A sensitivity analysis was carried out on the values of the threshold velocity, using values from 1/25 up to 1/250 of the average flow velocity. It can be demonstrated that threshold velocity is not really sensitive to such variations. The definition of n_f is really important in the calculation of the average velocity because in some cases the deposited layer can occupy up to 1/3 of the velocity field.

Figure 4.12 shows the average velocity versus time for each slurry concentration and for each camera. Every colour refers to a different camera. Time is in seconds and *t=0* corresponds to the gate opening. The average velocity lines start in the instant corresponding to the debris flow front reaching the corresponding camera section (§ 4.1.1).

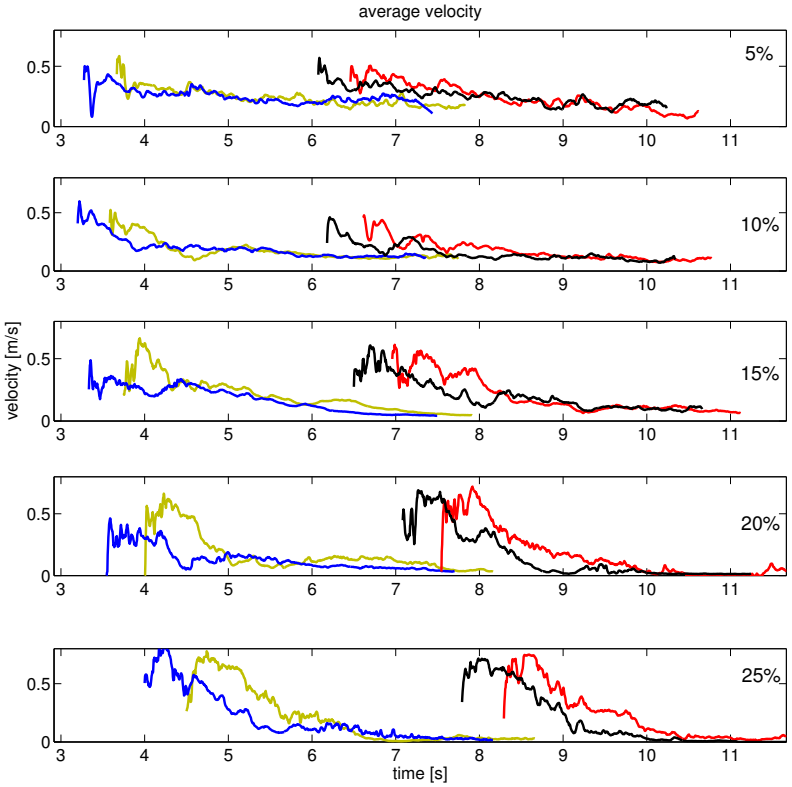

Figure 4.12 Average velocity of the flow versus time. Each color refers to a different camera (blue=3.60 m; green=4.10 m, black=7.30 m and red=7.80 m). For more details on the cameras see Chapter 3.

In all the experiments average velocity reaches its maximum values in the frontal parts of the flow and subsequently decreases. In the more sandy mixtures velocity diminishes smoothly, while it decreases very sharply for high clay content slurries. In particular, if the clay concentration is greater than 15%, it is possible to observe a strong difference in velocity between the “head” and the “body” of the flow.

This large velocity difference implies a significant amount of stretching, with the strain rate in the flow direction. By mass conservation, stretching in the longitudinal direction must be accompanied by constriction in the bed-normal one, and possibly also in the spanwise direction as long as the flowing body does not fracture (Elverhøi et al., 2005).

The stretching phenomenon have been experimentally observed by different authors (Elverhøi et al., 2005; Issler et al., 2004; Ilstad et al., 2004a; Ilstad et al., 2004b), however it has so far not been studied in detail. Bed-normal constriction was observed in the narrow channel (confined experiments) and both modes - bed-normal and spanwise direction - in the wide channels (unconfined experiments).

In the present work, thanks to the combination of the PIV technique and the four high speed cameras covering four different sections, it has been possible to have a measure of stretching versus time, downstream position and clay concentration.

The stretching $\dot{\varepsilon}(x,t)$ can be defined as (Eq.[4.12]):

$$\varepsilon_x(x,t) = \frac{\partial u}{\partial x}(x,t) = \lim_{\Delta x \to 0} \frac{u(x+\Delta x,t) - u(x,t)}{\Delta x} \qquad [4.12]$$

This quantity is not directly measurable. In order to estimate it, cameras of each pair have been placed at a distance Δx that allows for an appreciable velocity difference $u(x+\Delta x,t) - u(x,t)$. Equation [4.12] in its discretised form is:

$$\varepsilon_x\left(\frac{x_d + x_u}{2}, t\right) \approx \frac{u(x_d,t) - u(x_u,t)}{x_d - x_u} \qquad [4.13]$$

where x_d and x_u are two successive downstream positions. The velocity difference between the left and right parts of a single velocity field are negligible. Hence it has been necessary to use a pair of cameras at a distance

much larger than a frame width. Defined x_d and x_u are the abscissa of each pair of cameras and the distance $x_d - x_u$ is equal to 0.5 m.

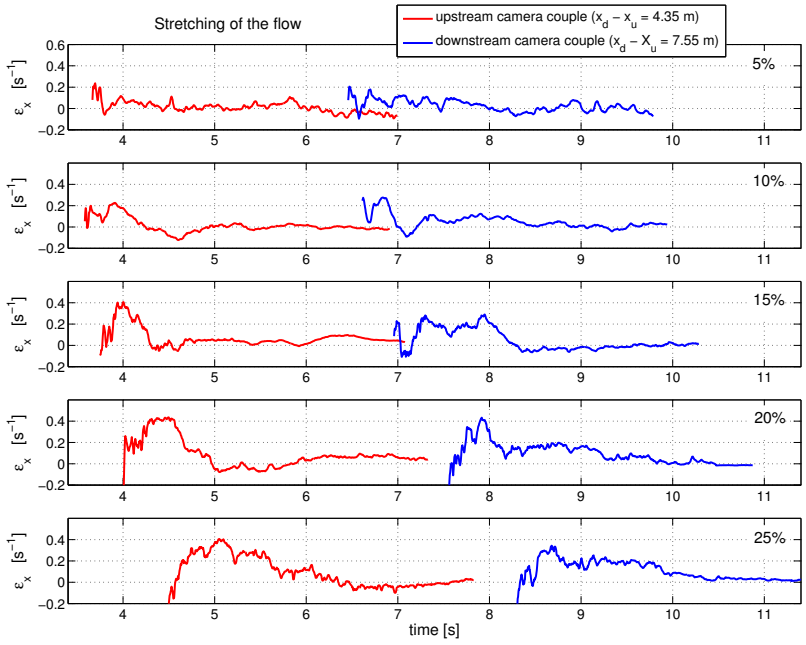

Figure 4.13 Stretching of the flow calculated for the upstream and downstream cameras pairs. Every graph refers to a different mixture.

Figure 4.13 plots stretching versus time, calculated for the two pairs of cameras; positive values of $\varepsilon_x(x,t)$ correspond to a wave lengthening. In all cases the larger values of stretching are concentrated in the first 1.5 seconds, after which they decrease. The maximum stretching rate has been recorded for high clay content slurries, with peaks of 0.4 s^{-1}. For the sandy mixtures the stretching exhibits lower values - it is still almost zero after one second - and a more constant trend. The trend of $\varepsilon_x(x,t)$ as a function of the clay concentration is given in Figure 4.14, where the average value of the stretching

- calculated for both the pairs of cameras - is plotted as a function of the clay content.

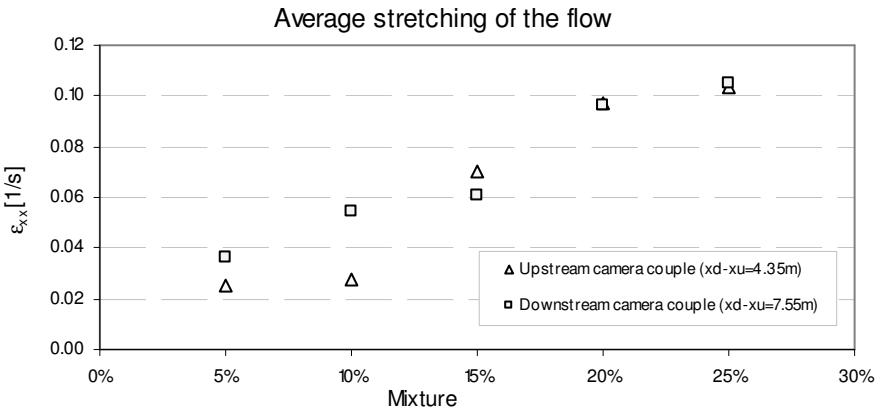

Figure 4.14 Average values of the stretching for the different mixtures.

It is possible to observe that the stretching increases linearly with the clay content up to 20%. It seems then to remain constant. The stretching values are very similar for the upstream and downstream cameras pairs, except in the case of 10% clay content (but that could be a measurement error).

Stretching in the longitudinal direction is accompanied by constriction in the bed-normal one and possibly also in the spanwise direction (Elverhøi et al., 2005). The constriction increases the strain in the longitudinal direction as long as the flowing body does not fracture and water is able to penetrate into the flow. Under those conditions, the head may detach completely from the body and form an out-runner block (Elverhøi et al., 2005).

The measurement data shows that the stretching, and thus the probability of head detaching, increases as a function of the clay concentration.

4.2 Deposition

The deposition is one of the main aspects of the phenomenon. It influences the rheology - because of the consequent changes in the composition of the material remaining in the flow - and hence the run-out length. Moreover, an understanding of the deposition process provides a possibility for predicting deposit composition as sorting, providing important information about the nature of the turbidites[12].

4.2.1 Deposition measurements

At the end of each experiment two or more samples of the deposit were taken in two sections, in order to analyse the deposit composition and granulometric distribution in detail. The samples were frozen using a wedge filled with dry ice and methanol and afterwards fixed with epoxy resin. The study of the samples, carried out by Hedda Breien, is still in progress and comparisons with measurements from images will be published in a future paper.

Velocity field measurements enable the deposited layer to be evaluated in different sections as a function of mixture composition. In particular, a cell is considered occupied by the flow if the velocity of the cell is lower than a threshold velocity equal to 1/100 of the average velocity of the flow. A

[12] The essential properties of reservoir rocks are their porosity and permeability (Hobson and Tiratsoo, 1981). The porosity provides the storage space for the oil, while the permeability is needed to allow the movement of fluids through the rocks. Consequently, grain size is one of the most important factors affecting the quality of a turbidite reservoir rock, with coarser-grained sedimentary rocks (sandstones) forming the most typical reservoir rocks. Sorting is also an important factor governing reservoir quality. A well-sorted reservoir rock results in an increase in the size of pore spaces.

sensitivity analysis was carried out on the values of the threshold velocity and these demonstrated that deposited layer depth is not really sensitive to threshold velocity variations (§ 4.1.4).

The use of an automatic procedure for image analysis to identify the deposited layer allows precise measurements of the bed layer as a function of time (Figure 4.15). It provides direct information on deposition rate as a function of the clay content but also useful data for developing and testing models.

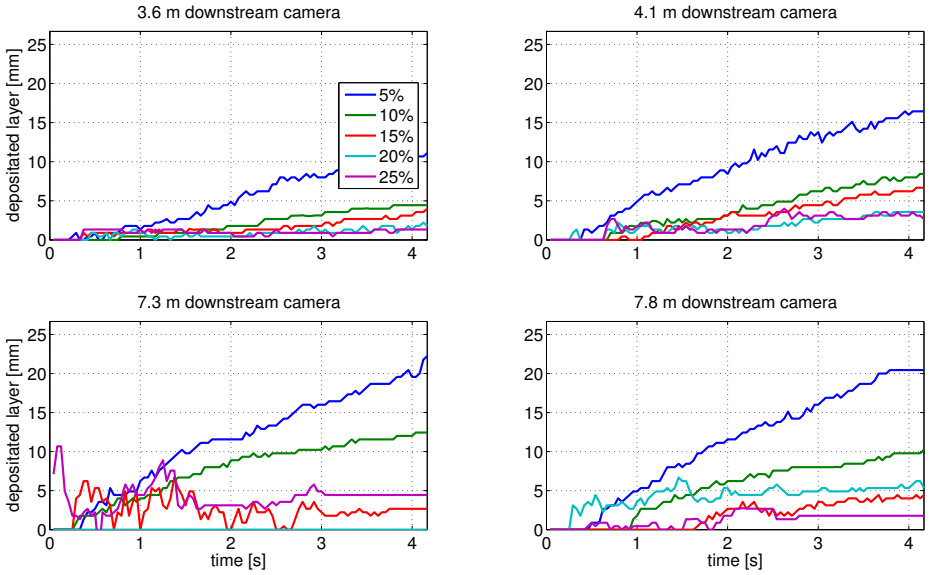

Figure 4.15 Deposited layer as a function of time for different mixtures and cross-sections.

The deposition rate is a clearly function of the clay content (Figure 4.15). The more sandy mixtures exhibit a higher deposition rate. Increasing the clay content, the deposit height is smaller, and it is almost zero for the case of 20% and 25% clay content slurries.

4.2.2 Data analysis

The idealised problem of a solid particle of volume Ω falling at a constant velocity v_f through a static homogeneous fluid has been analysed by Coussot (1997). The particle velocity can be computed by writing the balance of the resistance to motion F exerted by the surrounding fluid with the force of gravity minus the force of buoyancy. Assuming a hydrostatic pressure distribution, the buoyancy force is equal to the weight of the displaced fluid. The force balance can be written as (Eq. [B.1]).

$$F = \left(\rho_s - \rho_f\right) g\ \Omega \qquad [4.14]$$

Where ρ_f and ρ_s are respectively the interstitial fluid and the sand density.

For a single sphere slowly falling through an infinite volume of a static Newtonian fluid, the resistance due to fluid flow around the sphere is given by Stokes' law (Appendix B).

$$F = F_0 = 3\pi\mu_0 Dv \qquad [4.15]$$

It is shown from equations [B.1] e [4.15] that the stationary settling velocity of the ideal sphere is:

$$V = \frac{\left(\rho_s - \rho_f\right)gD^2}{18\ \mu_0} \qquad [4.16]$$

Equation [4.16] must be modified as soon as the fluid volume around the sphere can no longer be considered infinite. In particular F (Eq.[4.15]) is noticeably larger than F_0 if the solid volume fraction exceeds 0.01.

The settling velocity (Eq. [4.16]) is in inverse relation to the viscosity[13], and hence also to the clay content (§ 2.3.3). The difference of the deposited layer as a function of the clay content can be clearly observed in Figure 4.16 where the height of the final deposit is reported.

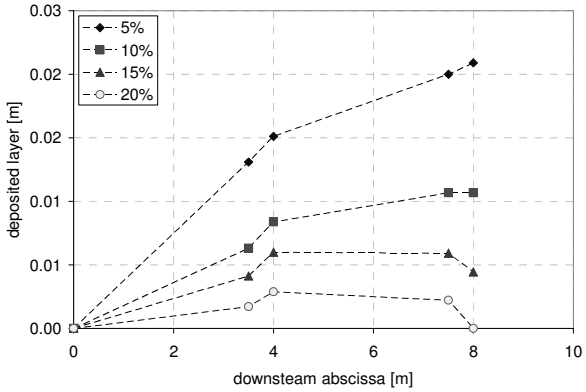

Figure 4.16 Longitudinal profile of the deposited layer

4.2.3 Deposit composition

A qualitative analysis of the deposit images (high speed cameras) shows a relation between mixture and deposit composition. In the case of the more sandy mixture, most of the clay is diluted in the water forming a turbidity current. On the other hand, whit higher clay contents, only a part of the clay is transferred from the parent flow to its associated turbidity current, while the rest is deposited with the sand. Hence the transformation of debris flows into turbidity currents depends on flow viscosity and density. Experiments carried out in the present work agree with Felix and Peakall (2006) in considering more efficient the transformation of less-dense flows.

[13] Note that the rheological measurements refer to the whole mixture, while in the present case the viscosity μ_0 of the sole clay should be considered.

Analysis of the samples, which is still in progress, and comparison of the results with the images, will give a more precise insight into the phenomena and allow quantitative measurements of the deposited clay and sand.

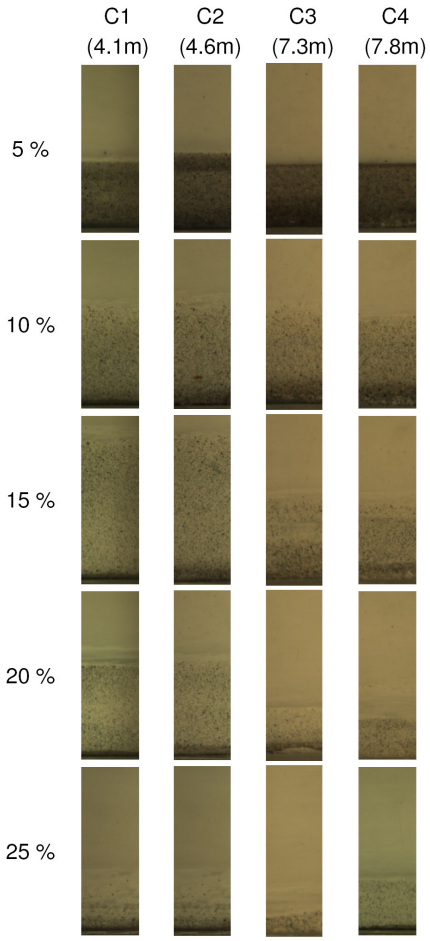

Figure 4.17 Images of the final deposit for different compositions and cross-sections.

4.3 Discussion

The measurement data showed that very different types of flow behaviour can be distingueshed as a function of the clay content of the slurries. Table 4.1 and Figure 4.18 summarise the main differences identified from analysis of the experiments.

Table 4.1 Main differences between high and low clay content slurries

	Low clay content	***High clay content***
Velocity profile	Shear layer with a thin plug flow on the top.	Thin shear layer at the base and plug-flow on the top.
Deposition	Deposition rate is in inverse relation to the viscosity. There is a large deposition of sand starting close to the gate.	The mixture remains compact, almost no deposition has been recorded.
Stretching	A low stretching rate has been measured. The average velocity along the wave diminishes gradually.	High degree of stretching has been measured behind the debris flow head (this is connected with the out-runner block detachment).

These observations drive to hint for Table 4.1 flow modelling. In low clay content mixtures, shear effects are prevalent. Models that take into account the visco-plastic nature of the slurry should be able to interpret it correctly. The rheology used in visco-plastic models has to be variable as a function of the deposition rate in order to take into account the rheology changes due to the mixture composition variations. On the other hand, the velocity profile in high clay content slurries presents a constant value (Figure 4.18), i.e. the debris flows

behave like a plug except at the base, where a lubricating layer - that causes hydroplaning - forms. For those flows, the hydro-dynamical forces on the debris flow surface will be dominant. The phenomenon is probably interpretable like a rigid body moving in a viscous fluid. Similar observations can be made concerning out-runner blocks.

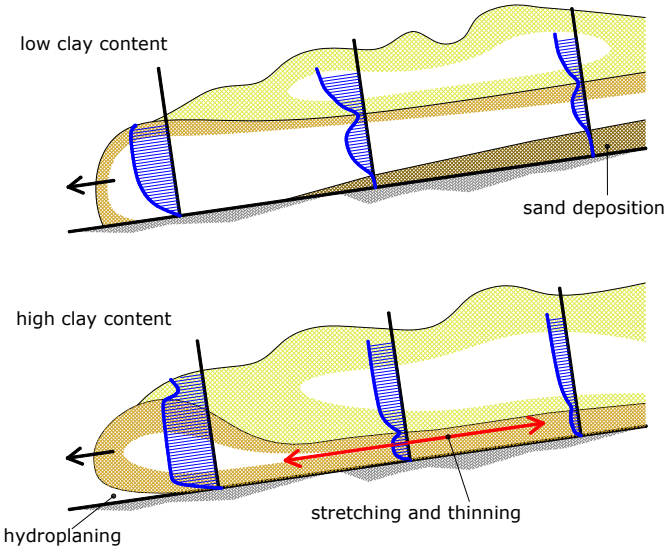

Figure 4.18 Summarising schematic showing the dynamical characteristics of the debris flow measured during the experiments.

The experiments also provide some insight into the transport capacity of the different slurries. The sand in low clay content mixtures is sedimented faster than the clay in the clay rich ones. This has an important effects on the deposited layer. Whit the low clay content mixtures, deposition starts close to the release area[14], so consequently only a limited amount of the initial sand is able to reach the end of the chute. In high clay content slurries, the sand remains trapped within the mixture and a considerable amount of sand reaches the end

[14] The head tank in the experiments, the shelf in the real scale phenomenon.

of the chute. This fundamental difference will similarly affect sediment transport from the shelf to the oceans, as shown in Figure 4.19.

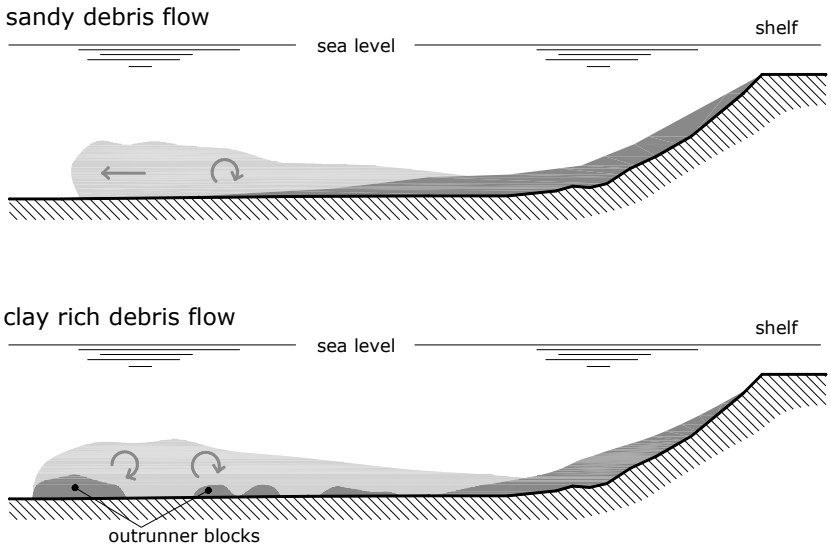

Figure 4.19 Possible effect of the debris flow composition on the sediment transport.

Further analysis of the deposit samples collected during the experiments (4.2.1) and the combining of the results with PIV measurements will give more details about the composition of the deposit and about the debris flow efficiency.

Chapter 5

5 Pressures analysis and CFD computation

In the study of submarine debris flows, measurement and analysis of pressure fields is of considerable importance. In fact pressure measurements can supply information about the flow regime, stresses at the bed, and hydroplaning.

5.1 Introduction

Despite uncertainties in interpreting the various experimental studies, pore pressures within the flow as well as at the base are regarded as crucial for predicting flow behaviour (Norem et al.,1990; Ilstad, 2003). Based on his comprehensive studies of coarse-grained subaerial debris flows, Iverson (1997) developed a model in which high pore pressure causes sediment liquefaction and thereby strongly reduces internal friction and increases sediment mobility and run-out. Others have suggested an almost spontaneous formation of excess pore pressures which then dissipate during the flow event (Hutchinson and Bhandari, 1971; Hutchinson, 1986).

Ilstad et al. (2004c) performed a set of laboratory experiments on subaqueous debris flows where both total-stress and pore-pressure transducers were mounted in the bed. Different sediment mixtures were used in the experiments. The pressure measurements confirmed earlier studies suggesting

that the front of the subaqueous clayey debris flow hydroplanes on a thin layer of water with low bed friction. The fronts of sandy debris flows displayed a fluidized head where bed friction also is minimal. Figure 5.1 shows a synthesis of the different situations recorded during those experiments (Ilstad et al.,2004c).

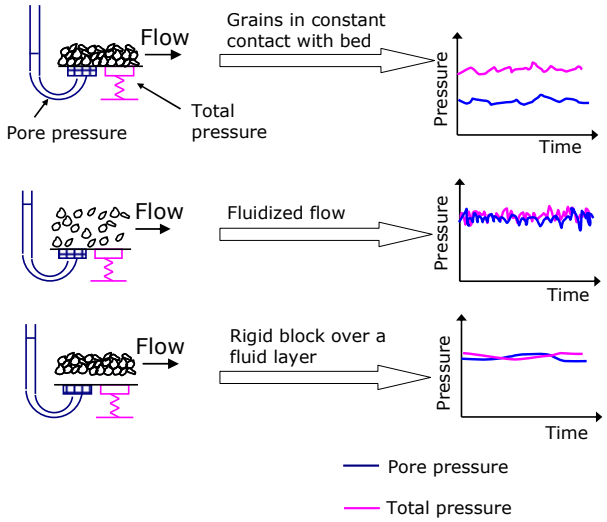

Figure 5.1 Different flow regimes as a function of total and pore pressure (modified from Ilstad et al., 2004c)

It has also been suggested that excess pore pressure at the interface between the flow and the bed results in a lubricating layer which reduces friction (Gee et al., 1999). Hampton (1972) had observed that, due to the combined action of pressure at the snout and underpressure above the head, a debris flow is able to hydroplane. More recently, the mechanism of hydroplaning has been directly observed in flume experiments (Mohrig et al., 1998; Ilstad et al., 2004a), where the debris flow rides on top of a thin lubricating water layer.

Values of pressure and velocity measured simultaneously in the same cross-sections are presented in this work, and provide important information about hydroplaning and its consequences for the flow regime. In particular, attention will be focused here on the development and sustainability of the hydroplaning.

5.2 Pressure data analysis

Measurements of both fluid pressure and total bed-normal stress were performed simultaneously at the chute base. Sensors were located in two cross-sections along the flow channel, at 3.5 and 7.6 metres from the head gate. For more details about the experimental setup, see Chapter 3.

5.2.1 Pressure measurements

Figure 5.2 shows the measured total and pore pressure for each of the mixtures. The sampling frequency was set at 1000 Hz in order to acquire the pressure peak at the front. The acquisition lasted 60 seconds - much longer than the debris flow wave duration - in order to also record the hydrostatic pressure in the deposited layer.

In the measured data that is presented here, a null value corresponds to the hydrostatic pressure at the particular transducer before the gate opening.

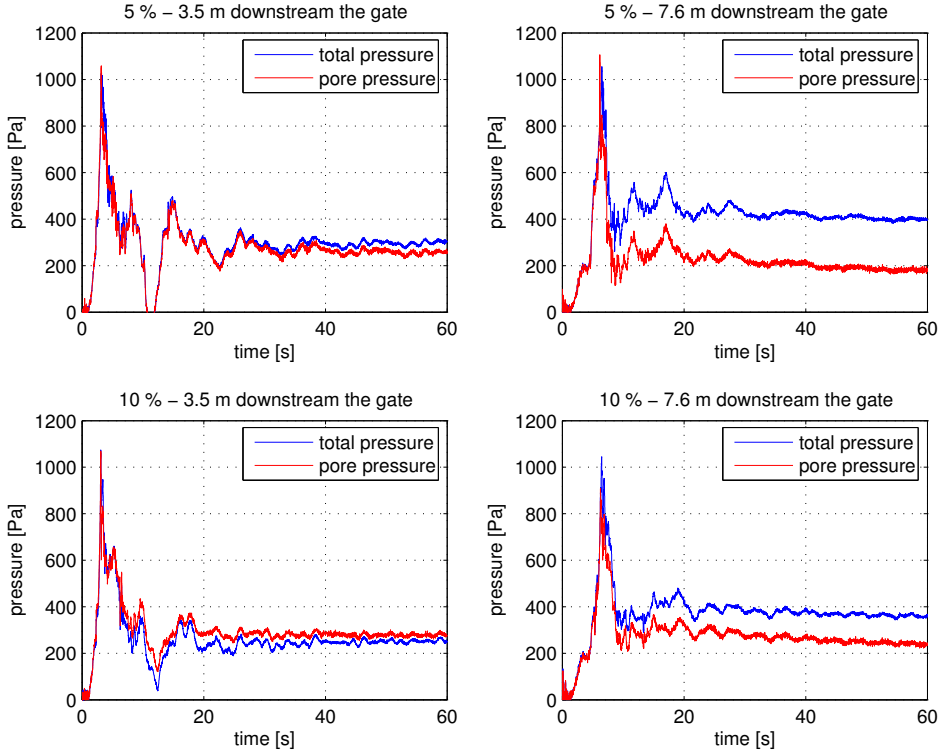
5 % – 3.5 m downstream the gate
5 % – 7.6 m downstream the gate
10 % – 3.5 m downstream the gate
10 % – 7.6 m downstream the gate
total pressure
pore pressure
pressure [Pa]
time [s]
0
200
400
600
800
1000
1200
0
20
40
60

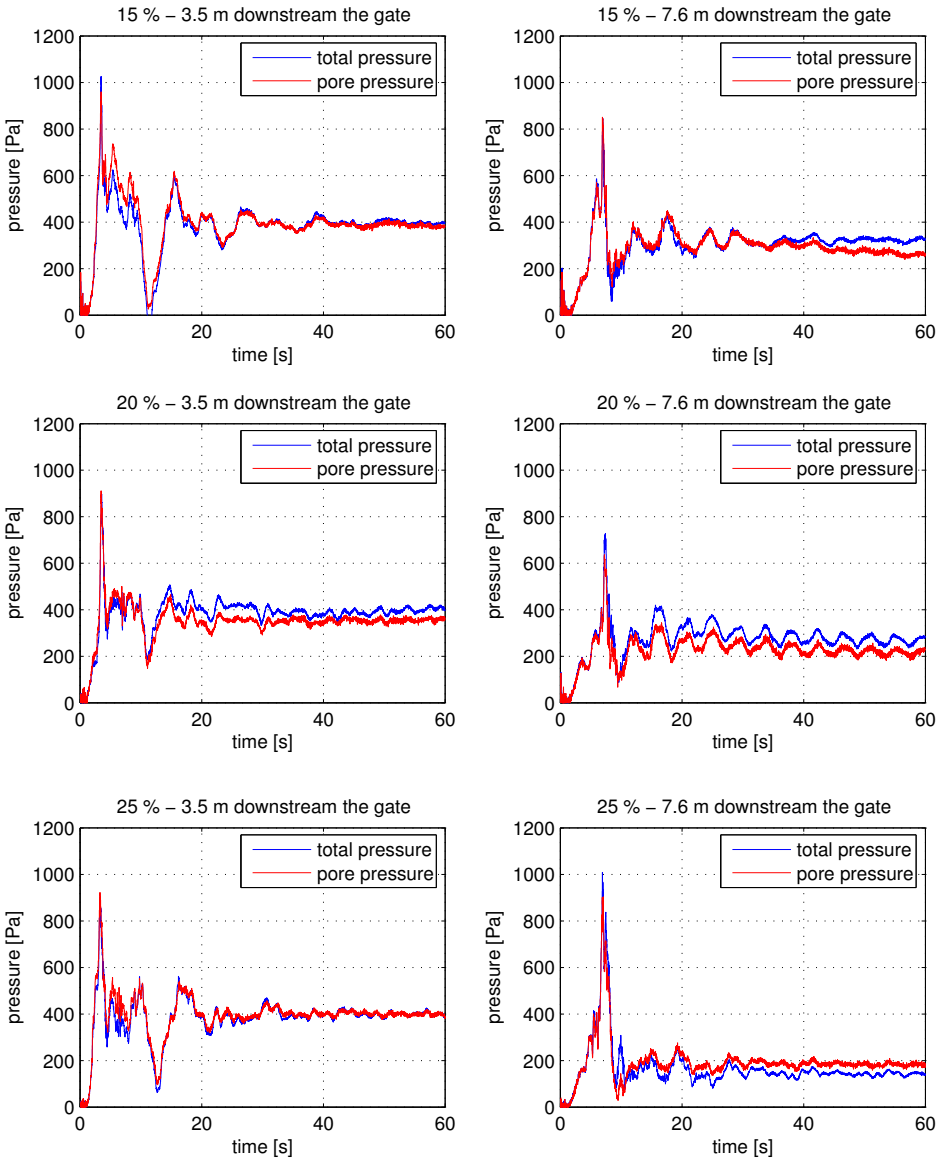

Figure 5.2 Measured pore and total pressure. Graphs refer to different chute cross section (the upstream one on the left and the downstream on the right) and different clay contents, 5%, 10% ,15%, 20%, 25% respectively.

As presented in Figure 5.2, pore pressure readings are often higher than total pressure but this would be a physically impossible situation. The deviant readings appear to be an artefact of the laboratory set-up, most likely connected to the pore pressure transducer mounting. While the total pressure transducers were flush mounted with the bed, the pore pressure sensors were separated from the chute bottom by a porous stone and a small reservoir (§ 2.2.2). The fact that the porous stone easily became clogged during the experiments is particulary relevant.

Some other authors have experienced this problem. Ilstad et al. (2004b) used a similar experimental apparatus to carry out short and longer duration measurements, involving an acquisition frequency of 500Hz during the flow event (20 seconds) and 10 Hz afterwards (1000 seconds). In many cases during the flow event - the dynamic phase - measured pore pressure was larger than the total pressure value, while in the subsequent "static phase" the pore pressure decreased, approaching the initial value.

Major and Iverson (1999) carried out experiments at the USGS debris-flow flume (Iverson et al. 1992) measuring the total normal stress and the pore pressure. In the case of loamy gravel debris flows, the pore pressure recorded after the debris flow front has passed exceeded the total pressure. In both these reported cases (Major and Iverson 1999; Ilstad et al., 2004b) no comments or explanations were offered concerning the discussed phenomenon.

Since the measurement of pore pressure seems to be beset with serious errors, in the present thesis the investigation of pressures conditions is mainly focused on measurements of total pressure.

5.2.2 Pressure data interpretation

Figure 5.3 shows a typical recording of total pressure. Various phases can be distinguished. Time zero corresponds to the gate opening. The initial wiggles (t< ~1s) are due to the vibrations, which are triggered by the gate opening, immediately propagating along the metallic part of the chute and subsequently being damped within about two seconds.

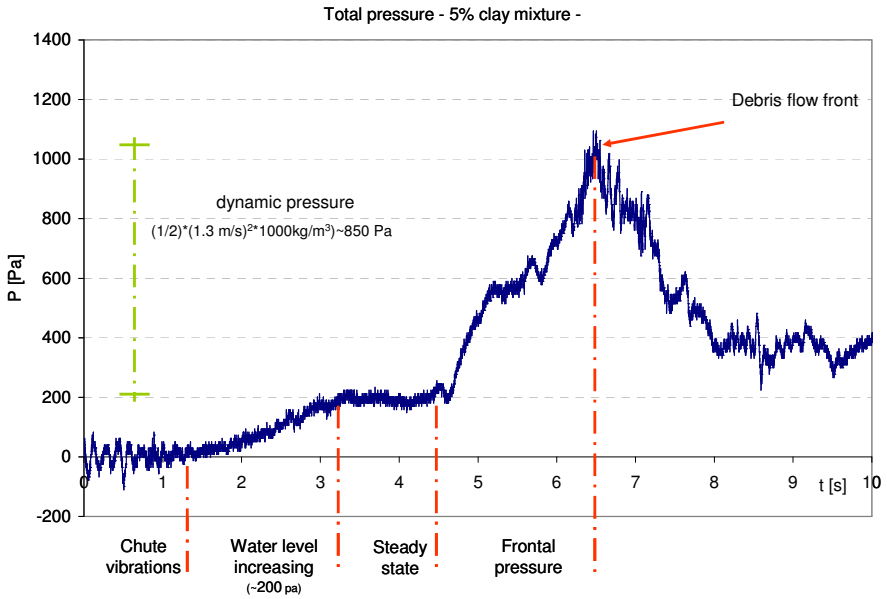

Figure 5.3 Time series of total pressure. It refers to the 5% slurry, downstream cross-section.

When the gate opens, 100 l of slurry is released into the fish tank. This causes the water level to rise 0.02 m ($0.1m^3/5m^2$), corresponding to a pressure increment of 200 Pa. The released volume generates a wave that propagates into the chute with a celerity c (Eq. [5.1]) function of the water depth h in the fish tank.

$$c = \sqrt{gh} \qquad [5.1]$$

Water depth h is about 1.8 m corresponding to a celerity of 4.2 m/s. Hence the wave generated by the slurry inlet takes 1.7 seconds to reach the cross section where the pressure transducer is installed (§ 2.2.2). In Figure 5.3 one may see that the pressure value increases almost linearly from 1.7 s to 3.2 s and to remain constant until t=4.5 s. As a debris flow pushes through the ambient water it experiences a dynamic pressure. This pressure propagates downstream ahead of the debris flow front (4.5 to 6.5 seconds in Figure 5.3). A pressure peak is recorded that corresponds to the debris flow head and is of the same order of magnitude of the dynamic pressure P_D (Eq.[5.2]).

$$P_D = \frac{1}{2}\rho_w U^2 \qquad [5.2]$$

where U is the average velocity and ρ_w is the water density. A more detailed explanation is given in § 5.3.3 where a CFD (computational flow dynamics) model has been used to reproduce the pressure field.

After the debris flow has passed, a prominent descendent peak is recorded in all the observed data. This is an *artificial* effect of the chute; the falling down of the material at the end of the chute produces a wave that propagates upstream with a velocity of c.

A precise evaluation of the peak magnitude is not possible using analytical formulas. However, arrival times to the pressure sensors have been calculated and agree with the measurements. An example is reported in Figure 5.4, where the arrival time of the wave in correspondence of the sensors has been drawn with a red dashed line. In the upstream section the effect of the wave is clearly recognizable because when it arrives the debris flow was already finished. In the downstream cross section the effect of the wave overlaps the debris flow pressure, hence it is note clearly visible.

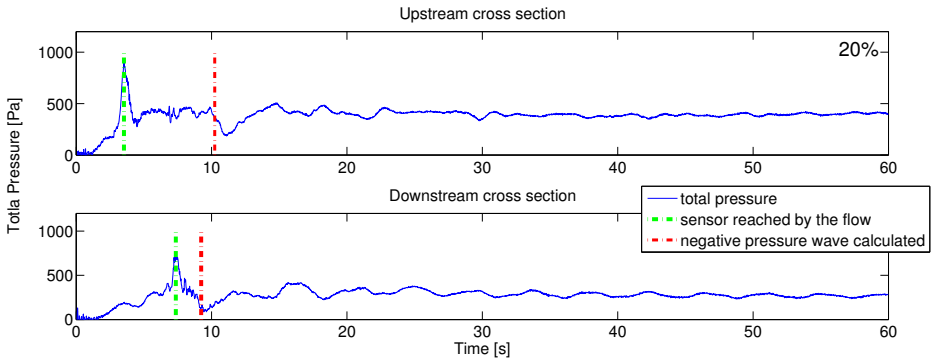

Figure 5.4 Comparison between the recorded pressure and the calculated arrival time to the sensors.

5.2.3 Relation between pressure and cameras data

All the secondary waves - described above, §5.2.2 - are damped before the end of the acquisition; hence it is possible to obtain a measurement of the static pressure P_{end} value when the debris flow is over. There is a marked difference between the data at upstream and downstream sensors. In the upstream ones the pore and total pressure readings at the end of the acquisition are almost identical while in the downstream ones the pore pressure tends to the value of 200 Pa as expected[15], while the total pressure is larger because it includes the weight of the deposited sediment layer. The problem of this difference was discussed above[16].

[15] If the initial pressure has to be zero, the final pressure has to be 200 Pa because the 100 l slurry initially released into the fish tank causes a 0.02 m. water level rise. Density variation of the ambient fluid due to the clay dispersion is negligible.

[16] The problem was recognised during the experiments and several tests were carried out to try to resolve it. The upstream and downstream pressure transducers were

High speed cameras allowed (§ 4.2.1) the depth of the deposited layer h_{dep} to be measured. The corresponding static pressure p_{hdep} (Eq. [5.3]) has been calculated and compared (Figure 5.5) with the value of the pressure recorded at the end of each experiment (*t=60 s.*)

$$p_h = \left(\gamma_{dep} - \gamma_w\right) h_{dep} \cos\theta \qquad [5.3]$$

where γ_{dep} and γ_w are the specific weight of the deposit and the water, respectively. Since no direct measurements of γ_{dep} were available, it has been approximated using γ_d, the slurry specific weight. The *arc effect* due to the sand presence in the deposit has been neglected.

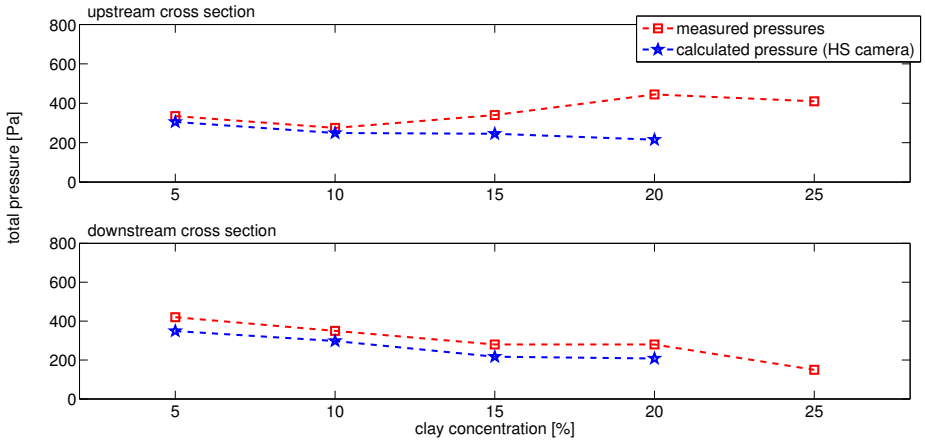

Figure 5.5 Comparison between measured pressures and ones calculated from deposit thickness.

switched, the calibration law double checked and brass filters replaced with new ones. The problem persisted, hence it is probably due to the mount as already mentioned.

Pressures calculated from deposit thickness recorded by the HS cameras are in accordance with the pressures measured with the transducers. With the exception of the upstream sensor in the case of high clay content mixtures, the differences are lower than 50 Pa, which is acceptable considering the approximation in the specific weight (Eq.[5.3]). In particular it is possible that the deposits are composed mainly of sand, as discussed in § 4.2.3, that has a specific weight (~24.5 N/cm^3) higher than the mixture one.

For a body moving in an fluid the relative fluid velocity at the front is zero. Here the pressure is highest with respect to the rest of the body (dynamic pressure, equation [1.1]). A comparison between the maximum pressure, measured in correspondence of the debris flow snout, and the dynamic pressure calculated using the front velocity (Eq. [5.3]) has been carried out.

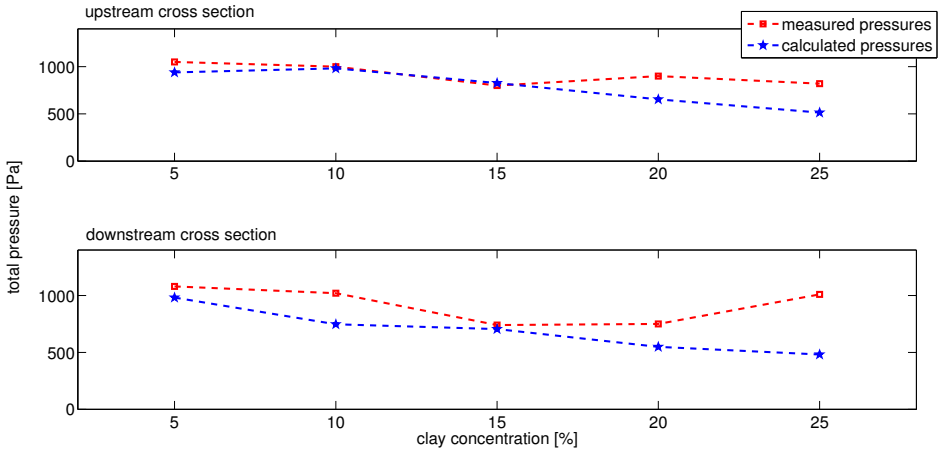

Figure 5.6 Comparison between the maximum pressure measured and the dynamic pressure calculated.

The maximum measured pressures (Figure 5.6) are quite close to the calculated dynamic pressure. Larger differences occur for the clay rich mixtures. No assured explanations have been found. The differences can be due to an effect of the shape on velocity distribution close to the debris flow snout.

Considerations reported in the present chapter, once again, show the capabilities of the application of the PIV technique to the study of subaqueous debris flows. In fact not only direct data about velocity are available, but derived quantities - like the deposition - can be subsequently calculated.

5.3 Computation fluid dynamic (CFD) computation

The long run-out distance of submarine debris flows on low angle fans represents an hydrodynamic enigma. Hampton (1972) observed that at certain velocities, due to the combined action of dynamic pressure at the snout and of dynamic underpressure above the head, the debris flow front is no longer capable of maintaining contact with the bed and a thin layer of water penetrates beneath the head and lubricates it. The same phenomena has been experimentally observed by other authors (Marr et al., 2001; Toniolo et al., 2004; Ilstad et al., 2004b).

The aim of the present chapter is to show how measured pressures, velocities and wave shapes are linked to the formation of a lubricating layer, i.e. to hydroplaning. In order to investigate this, a numerical model of the phenomenon was built to compute the pressure field during the flow. Numerical solutions were computed using STAR-CD.

The simulations have concentrated on the experiments with the 15% clay slurry. This case was considered to best represent the hydroplaning condition, and the shape and velocity differences with the higher clay contents were not marked enough for the model application.

5.3.1 Introduction to STAR-CD

STAR-CD is an integrated package containing both solver and advanced pre/post-processing tools. It is designed as a multi-physics simulation tool capable of modelling fluid flows. STAR-CD is a CFD code based on the finite volume method and can handle flows in steady or unsteady state.

Different turbulence models are available in STAR-CD. In the present case the standard k-ε model for high Reynolds numbers has been used.

5.3.2 Model implementation

The model has been built in order to reproduce the 15% clay slurry experiment (as mentioned above, § 5.3). The snout shape was obtained from a photograph (Figure 5.7) taken by the SLR digital camera at the upstream measurement cross-section.

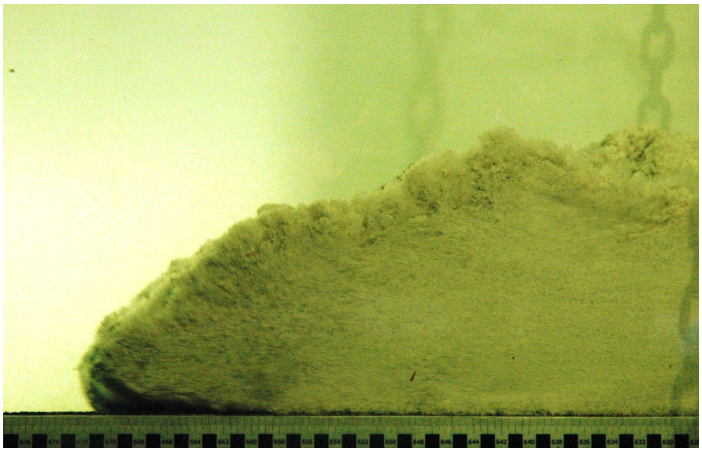

Figure 5.7 Image of the debris flow snout taken by the SLR digital camera. The picture refers to the 15% clay experiment.

As shown by the front and average velocity measurements (Figure 4.4 and Figure 4.5), as a first approximation the motion of the slurry can be considered steady after an initial acceleration phase (§ 4.1.1). This observation allowed us to simulate the flow in a steady state condition, modelling the motion as a stationary debris flow block with water flowing around it. In other words, instead of simulating the debris flow movement with respect to the static perimeter of the chute, the motion of the slurry was computed with respect to the ambient water.

Four different conditions have been investigated (Figure 5.8). For case "1" a very simplified shape was used to test the model and to assess the importance of the shape in the drag coefficient. Three models with the same shape of the frontal shape have been tested. The models differ in the zone close to the chute bed, in particular case "2" does not hydroplane, case "3" has only a small part of the snout raised from the bed, while case "4" is completely detached from the bottom. In cases "3" and "4" part of the ambient fluid can escape from below the debris flow snout.

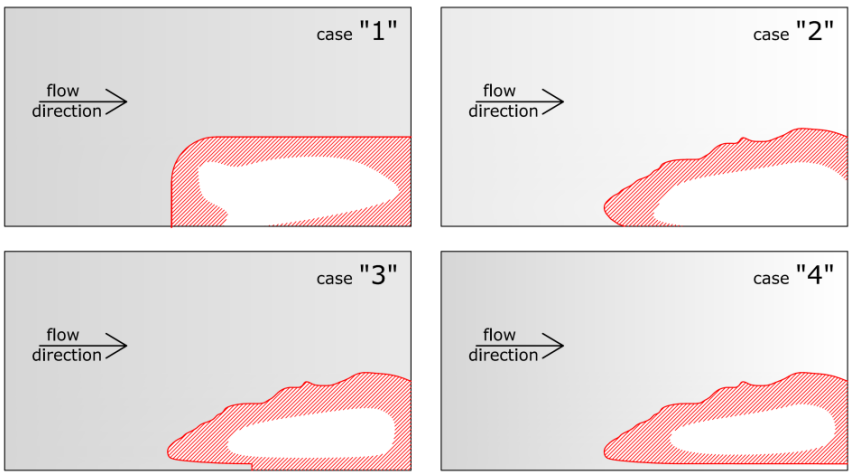

Figure 5.8 Schema of the four treated cases.

The boundary conditions have been chosen so as to properly model the relative motion of the debris flow with respect to the ambient fluid. With reference to Figure 5.9, boundary conditions can be summarised as follow:

A - *Inlet condition*. The inlet flow occupies the whole right part of the motion field. The inlet is assigned as a velocity, set equal to the measured frontal velocity ($v=1.237\ ms^{-1}$).

B - *Pressure condition*. The pressure in the upper P_b part has been set to be constant ($P_b=0$).

C - *Pressure condition*. The pressure in right part of the flow field has been set to be constant and equal to zero. This allows the ambient water to leave the computational field without set velocities.

D - *Outlet condition*. In the cases where the debris flow hydroplane an outlet condition below the debris flow has been set. The outlet condition consist of a constant mass flow rate (kg/s). In order to properly set this parameter a sensibility analysis has been carried out, for more details see § 5.3.3.

E - *Wall condition.* The debris flow has been represented as wall. This is a very simplified vision of the problem because all the interactions - mass exchanges, deformation of the debris flow shape, etc. - between the slurry and the ambient fluid have been neglected. Both the condition of slip and of no-slip have been tested and compared (§ 5.3.3).

F - *Wall condition.* The chute bottom has been represented as a wall moving at the same velocity as the inlet fluid ($v=1.237\ m/s^{-1}$). A no-slip condition has been used. In the simulation, the fluid behaviour close to the wall (near-wall zone) has been treated using a wall-function.

As a first approximation the velocity profile close to the wall has been described with a logarithmic function (Eq. [5.4])

$$U^+ = \frac{1}{\kappa} \ln\left(E\ y^+\right) \qquad [5.4]$$

where E is an empirical coefficient ($E=9$) and k the Von Karman's constant ($k=0.41$). y^+ is the normalized distance from the wall (Eq.[5.5]).

$$y^+ = \frac{y u_*}{\nu} \qquad [5.5]$$

where $u_* = \sqrt{\tau_u \rho^{-1}}$ is the wall stress. In the model, the dimensions of cells close to the wall have been iteratively refined in order to reach a value of Δy^+ in a range around 70~100.

The "F" condition allows the relative motion of the debris flow with respect to the chute and the ambient water to be correctly represented. In fact in this a way both the ambient fluid and the bottom are moving with respect to the debris flow with a velocity equal to the front velocity measured during the experiments. Once again it must be emphasised that the implemented model is an oversimplification of the real problem, which is the interaction of two different fluids (i.e. the debris flow and water). A two-phase approach to the problem was used by Gauer et al. (2006) in order to study the interaction between the slide and the ambient water. They show the development of a high-pressure wedge of ambient water beneath the debris flow and of underpressure along its upper surface, which, in agreement with the laboratory experiments, leads to a hydroplaning head. In addition, a velocity decrease could be observed from the head to the tail of the slide, which leads to stretching of the slide mass. Comparison is planned between the experimental data showed in this thesis and Gauer's numerical model.

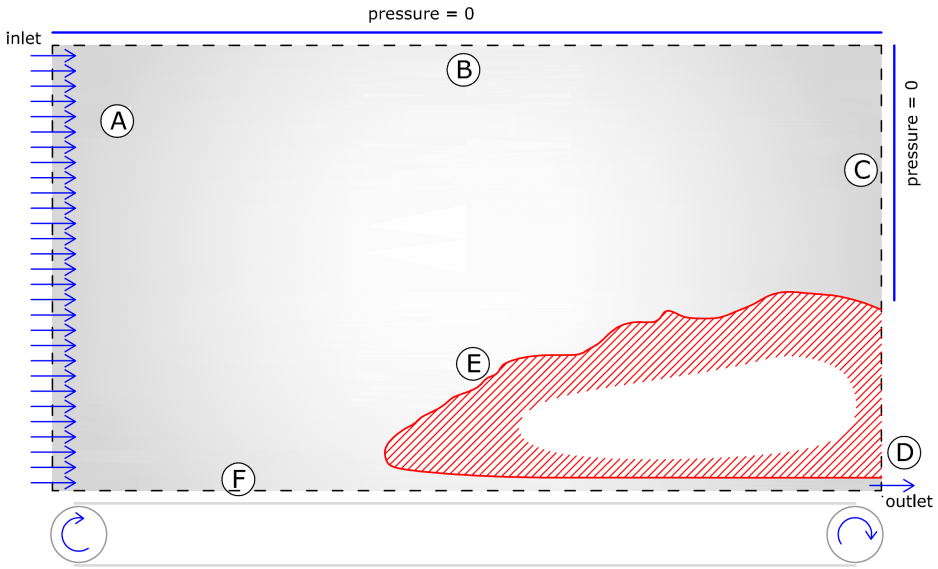

Figure 5.9 Boundary condition schematic.

The mesh definition is one of the most important phases of the model implementation. A tetrahedral non-structured mesh has been used. The cells have been thinned along the debris flow contour - in order to better represent the shape - and also where the flow quantities vary more. The cells thinning required an iterative refining of the mesh in order to evaluate correctly the zones where the velocity and pressure variations were more.

A linear upwind second order algorithm (*SIMPLE*) has been used. The tolerance for the algorithm convergence was set to 0.1 % for all the quantities from the moment and mass conservation equations.

5.3.3 Results and comparisons with experimental data

The *CDF* model provided the pressure and the velocity vector at each mesh joint. Models were run trying both the condition of slip and of no-slip for the debris flow body. From the point of view of pressures, no significant

differences have been noticed. An example of the same model with both conditions is shown in Figure 5.10, where the pressure at the base is plotted. For this reason all the results in the present work will refer to the "slip" case.

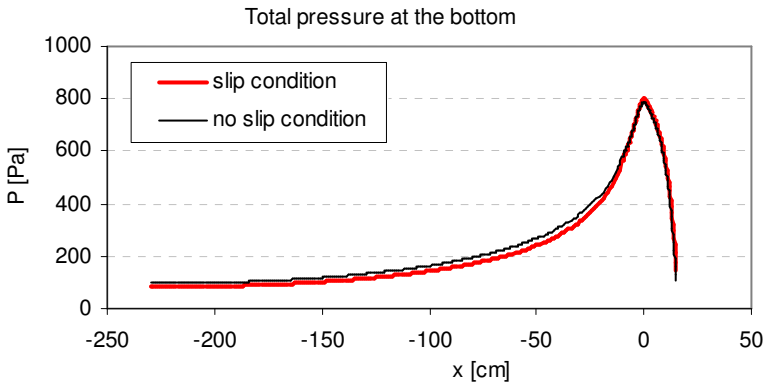

Figure 5.10 Comparison between slip and no-slip condition for the debris flow body. Pressures refer to case "3"- Figure 5.8.

Figure 5.11 shows the result of the *CFD* calculations[17]. All these cases display a similar behaviour. The pressure increases in front of the debris flow snout and reaches its maximum value at the stagnation point.

Over the debris flow body the relative pressure become negative. It should be noticed that it is in this part of the debris flow where clay particles entrainment into the overlaying water masses and the formation of turbidity currents have been observed. Similar hypothesis were formulated by Hampton (1970) based on the analytical solution of the Navier Stokes equations for a very simple geometry. The CFD model allows the use of a more complex geometry, in particular in this case the experimentally measured geometry has been used. This allows better identification of the zones where the pressure is lower and thus where the turbidity current is generated.

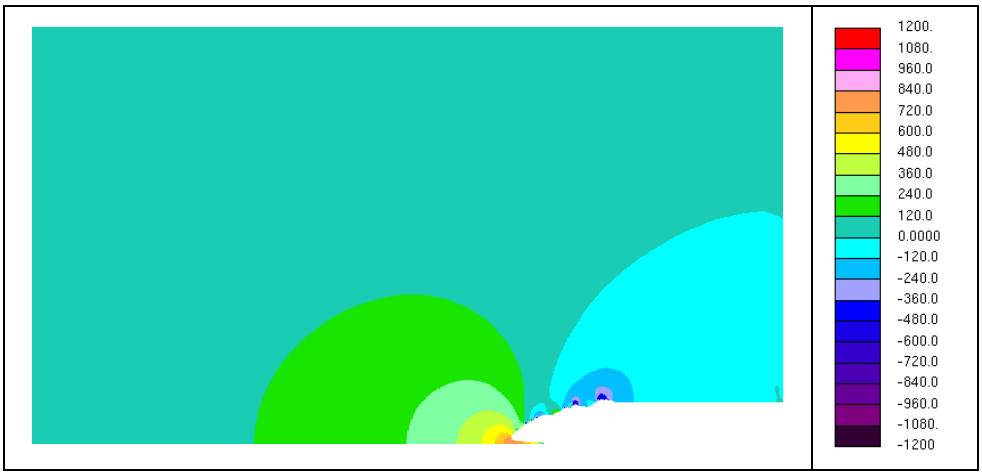

Figure 5.11 Case "C", outlet = 0.6185 kg/m^3 - Pressure field, pressures are in Pa.

Pressure values at the bottom have been compared with experimental data (Figure 5.12). Case "4" has not been plotted because, in the investigated part, the pressures are exactly the same of case "3".

The model that furnishes the best interpretation of the phenomena is case "3" with an outlet under the debris flow body (see boundary condition "D" in § 5.3.2). The maximum pressure value is very close to the measured one, and also the position corresponds. Small differences can be observed in the pressure increasing, but the general behaviour is similar.

[17] Pressure field for the sole case "3" (Figure 5.8) has been plotted because it is considered the most interesting case.

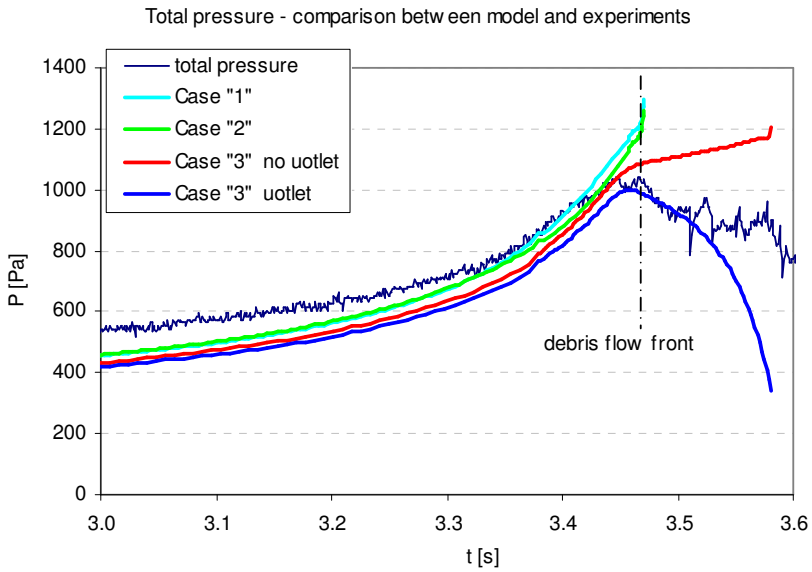

Figure 5.12 Pressure at the bottom. Comparison between experimental data and numerical simulation.

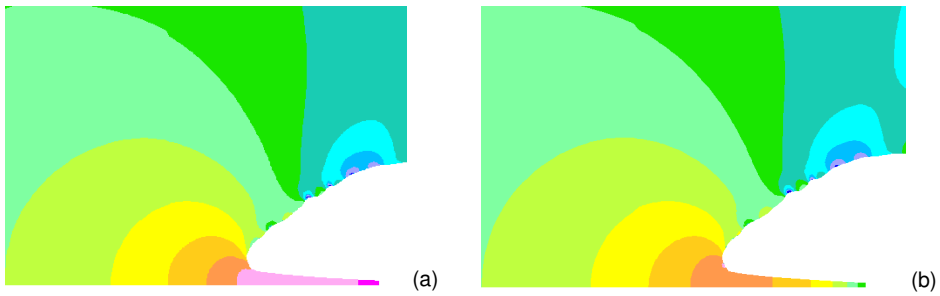

Figure 5.13 Comparison between Case "C", outlet = 0 kg/m^3 and outlet = 0.6185 kg/m^3. Close up of the debris flow snout. The colours are the same of Figure 5.12.

Case "3" has been tested both with and without the outflow condition (respectively Figure 5.13-b and Figure 5.13-a). The difference is evident in the hydroplaning part. In particular if there is a flow rate under the body the pressure decreases velocity increasing and this seems to agree the experimental results.

In order to verify the condition of hydroplaning in this case (case "3" with outflow), a force balance has been carried out on the lifted part. In particular lift force F_L due to the pressure has been calculated and compared with the weight F_g of the lifted part.

$$F_g = V_L(\gamma_d - \gamma_w)\cos\theta \qquad [5.6]$$

where V_L is the total volume of the lifted part and θ is the chute bed angle. F_L results equal to 9,5 N while F_g 11,9 N. Considering the strong simplification adopted in the calculation, the results can be considered promising. In particular, calculated pressures seem to allow the hydroplaning condition, postulated for the base of the submarine long run-out by different researchers (Hampton, 1972; Harbitz et al., 2003; Marr et al. 2001).

Conclusions

A particle image velocimetry (PIV) technology has been developed and a series of experiments were carried out using this technique. The PIV developed, combined to an advanced experimental apparatus, allowed to measure for the first time quantities like stretching and detailed velocity profiles as a function of the time and slurry properties.

Carried out experiments put in evidence the most relevant characteristics of the phenomenon. In particular velocity profiles, stretching and average flow velocity have been analysed and the differences between sandy and clay rich slurries have been underlined.

The measurement data showed that very different types of flow behaviour can be distinguished as a function of the clay content of the slurries. These observations drive to hint for flow modelling. In low clay content mixtures, shear effects are prevalent. Models that take into account the visco-plastic nature of the slurry should be able to interpret it correctly. The rheology used in visco-plastic models has to be variable as a function of the deposition rate in order to take into account the rheology changes due to the mixture composition variations. On the other hand, the velocity profile in high clay content slurries presents a constant value, i.e. the debris flows behave like a plug except at the base, where a lubricating layer - that causes hydroplaning - forms. For those flows, the hydro-dynamical forces on the debris flow surface will be dominant. The phenomenon is probably interpretable like a rigid body moving in a viscous fluid. Similar observations can be made concerning out-runner blocks.

The experiments also provide some insight into the transport capacity of the different slurries. The sand in low clay content mixtures is sedimented faster than the clay in the clay rich ones. This has an important effects on the deposited layer. Whit the low clay content mixtures, deposition starts close to the release area, so consequently only a limited amount of the initial sand is able to reach the end of the chute. In high clay content slurries, the sand remains trapped within the mixture and a considerable amount of sand reaches the end of the chute. This fundamental difference will similarly affect sediment transport from the shelf to the oceans.

Further analysis of the deposit samples collected during the experiments and the combining of the results with PIV measurements will give more details about the composition of the deposit and about the debris flow efficiency.

As well as the velocity data, pressure have been examined and interpreted with the help of a *CFD* model. The computed pressure field is consistent with the experimental data. Under hydroplaning condition the force due to pressure field is capable to sustain the debris flow snout weight.

A challenge in the coming years will be to develop a dynamical model that captures the dynamical properties of subaqueous debris flows and accurately predicts their run-out distances and velocities. This thesis, thank to the accurate measure of the velocity, highlights some of the features that need to be taken into account in such a model.

References

1. Aksu A.E., Hiscott R.N. (1992). “Shingled Quaternary debris flow lenses on the northeast Newfoundland slope”, *Sedimentology*, vol.39, 193-206.
2. Barbolini M., Biancardi A., Natale L., Pagliardi M. (2005). “A low cost system for the estimation of concentration and velocity profiles in rapid dry granular flows”*, Cold Regions Science and Technology*, vol.43, no.1-2, 49-61.
3. Best J., Kirkbride A. and Peakall J. (2001). “Mean flow and turbulence structure of sediment-laden gravity currents: new insights using ultrasonic Doppler velocity profiling”, *Particulate Gravity Currents, IAS Spec*. Vol. 31, 159-172.
4. Biancardi A, Ghilardi P., Pagliardi M. (2005a). “Automatic Mask Extraction for PIV-Based Dam-Break Analysis”, *Lecture Notes in Computer Science*, vol. 3523, Proceedings Second Iberian Conference, IbPRIA 2005, Estoril, Portugal, June 7-9, 2005.
5. Biancardi A., Ghilardi P., Pagliardi M. (2005b). “Dry Granular Flows Need Special Tools”, *Proceedings “The 2nd Canadian Conference on Computer and Robot Vision”* pp. 514-520.
6. Breien H., Pagliardi M., Elverhøi A., De Blasio F.V., Issler D. (2007). “Experimental studies of subaqueous vs. subaerial debris flows – velocity characteristics as a function of the ambient fluid”, *Proceeding Third International Symposium on Submarine Mass Movements and Their Consequences. Santorini,1-3rd October 2007.*

7. Chen C.L. (1988). "Generalized viscoplastic modeling of debris flows", *Journal of Hydraulic Engineering*, vol. 114, 237-258.

8. Chen R.H., Lin M.L., Chen H. (1993). "Preliminary study of the material properties of the debris flow at Tong-Mang", *Journal of Chinese Soil and Water Conservation,* vol. 24, no.1, 65-73.

9. Clift R., Grace J.R., Weber M.E. (1978). "Bubbles, drops and particles", *Academic Press, London*.

10. Coussot P., Meunier M. (1996). "Recognition, classification and mechanical description of debris flows", *Earth-Science Reviews*, vol. 40, 209–227.

11. Coussot P. (1997). "Mudflow rheology and dynamics", *Rotterdam, Netherlands, A.A. Balkema*.

12. Coussot P., Piau J.M. (1994). "On the behaviour of fine mud suspensions", *Rheologica Acta*, vol. 33, 175-184.

13. Cowen, E.A., Monismith S.G. (1997). "A hybrid digital particle tracking velocimetry technique", *Experiments in Fluids*, vol.22, 199-211.

14. Davies T.R.H. (1986). "Large debris flows: a macro-viscous phenomenon", *Acta Mech*., vol. 63, 161-178.

15. De Blasio F. V., Elverhøi A., Issler D., Harbitz C. B., Bryn P., Lien R. (2004a). "Flow models of natural debris flows originating from overconsolidated clay materials", *Marine Geology*, vol. 213, 439-455.

16. De Blasio F. V., Engvik L., Harbitz C. B., Elverhøi A. (2004b). "Hydroplaning and submarine debris flows", *Journal of Geophysical Research*, vol. 109, C01002.

17. De Blasio F.V., Elverhøi A., Issler D., Harbitz C.B., Bryn P., Lien, R. (2005). "On the dynamics of subaqueous clay rich gravity mass flow – the giant Storegga slide, Norway", *Marine and Petroleum Geology*, vol. 22, 179-186.

18. De Blasio F.V., Elverhøi A., Engvik L., Issler D., Gauer P., Harbitz C. (2006). "Understanding the high mobility of subaqueous debris flows", *Norwegian Journal of Geology*, special issue: second international symposium on submarine mass movements and their consequences, A. Solheim (editor), vol. 86, 275-284.

19. Edgers L., Karlsrud K. (1981). "Viscous analysis of submarine flows", *Report 52207-3, Norwegian Geotechnical Institute.*

20. Elverhøi A., Hooke R.L., Solheim A. (1998). "Late Cenozoic erosion and sediment yield from the Svalbard–Barents Sea region: implications for understanding erosion of glacierized basins", *Quat. Sci. Rev*., vol.17, 209-241.

21. Elverhøi A., Harbiz C.B., Dimakir P., Morig D., Marr J., Parker G. (2000). "On the dynamic of subaqueous debris flows", *Oceanography*, vol. 13, no. 3, 109-117.

22. Elverhøi A., De Blasio F. V., Butt F. A., Issler D., Harbitz C. B., Engvik L., Solheim A., Marr, J. (2002). "Submarine mass-wasting on glacially influenced continental slopes – processes and dynamics, in Glacier-Influenced Sedimentation on High-Latitude Continental Margins" edited by J. A. Dowdeswell and C. ´O Cofaigh, *Geological Society of London*, London, UK, 73–87.

23. Elverhøi A., Issler D., De Blasio F.V., Ilstad T., Harbitz C.B., Gauer, P. (2005). "Emerging insights into dynamics of submarine debris flows", *Natural Hazards and Earth System Sciences*, vol.5, 633-648.

24. Felix M., Peakall J. (2006). "Transformation of debris flows into turbidity currents: mechanisms inferred from laboratory experiments", *Sedimentology*, vol.53, 107-123.

25. Gauer P., Elverhøi A., Issler D., De Blasio F. V. (2006). "On numerical simulations of subaqueous slides: Back-calculations of laboratory experiments of clay rich slides", *Norwegian Journal of Geology*, special issue on submarine landslides, vol. 86, 295-300.

26. Gee M.J.R., Masson D.G., Watts A.B., Allen P.A. (1999). "The Saharan debris flow: an insight into the mechanics of long run-out submarine debris flows", *Sedimentology*, vol.46, 317-335.

27. Graf, W. H. (1971). *Hydraulics of Sediment Transport*, New York: McGraw-Hill Book Company.

28. Hampton M.A. (1970). *Subaqueous debris flow and generation of turbidity currents*, Ph.D. thesis, Stanford University, Stanford, California, USA.

29. Hampton M.A. (1972). "The role of subaqueous debris flows in generating turbidity currents", *Journal of Sedimentary petrology*, vol. 42, 775-793.

30. Hampton M.A., Lee H.J., Locat J. (1996). "Submarine landslides", *Review of Geophysics*, vol. 34, p. 33-59.

31. Harbitz C.B., Parker G., Elverhøi A., Marr J., Mohrig D., Harff P. (2003). "Hydroplaning of subaqueous debris flows and glide blocks: Analytical solutions and discussion", *Journal of Geophysics Research*, vol. 108, B7.

32. Hobson G.D., Tiratsoo E.N. (1981). *Introduction to Petroleum Geology*, Gulf Publishing Company, Houston.

33. Huang X., Garcia M. H. (1998). "A Herschel-Bulkley model for mud flow down a slope", *Journal of Fluid Mechanic*, vol. 374, 305-333.

34. Huang X., Garcia M.H. (1999). "Modeling of non-hydroplaning mudflows on continental slopes", *Marine Geology*, vol. 154, 131-142.

35. Hungr O. (1988). *Dynamics of rock avalanches and types of slope movements*, Ph.D. thesis, University of Alberta, Edmonton, AB.

36. Hutchinso J. N. (1986). "A sliding-consolidation model for flow slides", *Can. Geotech. J.*, vol. 23, 115-126.

37. Hutter K., Savage S. B. (1988). "Avalanche dynamics: the motion of a finite mass of gravel down a mountain side", *5th International Symposium on Landslides*, 10–15 July, Lausanne, Switzerland, vol.1, 691-697.

38. Ilstad T., De Blasio F. V., Elverhøi A., Harbitz C. B., Engvik L., Longva O., Marr J. G. (2004a). "On the frontal dynamics and morphology of submarine debris flows", *Marine Geol.*, vol. 213, 481-497.

39. Ilstad T., Elverhøi A., Issler D., Marr, J. (2004b). "Subaqueous debris flow behaviour and its dependence on the sand/clay ratio: a laboratory study using particle tracking", *Marine Geol.*, vol. 213, 415-438.

40. Ilstad T., Marr J. G., Elverhøi A., Harbitz C. B. (2004c). "Laboratory studies of subaqueous debris flows by measurements of pore-fluid pressure and total stress", *Marine Geol.*, vol. 213, 403-414.

41. Imran J., Harff P., Parker G. (2001). "A numerical model of submarine debris flows with graphical user interface", *Computers and Geosciences*, vol. 27, no.6, 721-733.

42. Issler D., De Blasio F. V., Elverhøi A., Bryn P., Lien R. (2005). "Scaling behaviour of clay-rich submarine debris flows", *J. Marine Petrol. Geol.*, vol.22, 187-194.

43. Iverson R. M., Reid M. E. (1992). "Gravity-driven groundwater flow and slope failure potential elastic effective-stress model", *Water Resour. Res*., vol. 28, 925-938.

44. Iverson R.M. (1997). "The physics of debris flows", *Reviews of Geophysics*, vol. 35, 245-296.

45. Iverson R. M., Denlinger R. P. (2001). "Flow of variably fluidized granular masses across three-dimensional terrain, Coulomb mixture theory", *J. Geophys. Res*., vol. 106, 537-552.

46. Johnson A. M. (1970). "*Physical Processes in Geology"*, Freeman, San Francisco, California.

47. Keane R. D., Adrian R. J. (1990). "Optimization of particle image velocimeters. Part I: double pulse system", *Meas. Sci. Technol*., vol.1, 1202-1215.

48. Keane R. D., Adrian R. J. (1992). "Theory of cross-correlation analysis of PIV images", *Meas. Sci.Technol.,* vol. 2, 191-215.

49. Kuenen Ph.H. (1948). "The formation of beach cusps", Journal of Geology, vol. 56, 34-40.

50. Kuenen, Ph.H. (1950). "Turbidity currents of high density", *18th International Geological Congress*, part 8, 44-52.

51. Kuenen Ph.H, Migliorini C.I. (1950). "Turbidity currents as a cause of graded bedding", *The Journal of Geology*, vol.58, 91-107

52. Kuenen, Ph.H. (1951). "Properties of turbidity currents of high density", *Turbidity Currents and the Transportation of Coarse Sediments to Deep Water-a Symposium.* Vol. 2, 14-33.

53. Locat J. (1997). "Normalized rheological behavior of fine mud and their flow properties in a pseudoplastic regime", *Debris-Flow Hazards, Mitigation, Mechanics, Prediction, and Assessment,* American society of Civil engineers, New York, 260-269.

54. Locat J., Lee H. J. (2001). "Submarine landslides: advances and challenges", *Can. Geotech. J.*, vol. 39, 193-212.

55. Major,J. J. (1993). "Rheometry of natural sediment slurries", *Proc.,1993 Conf. on Hydraulic Engineering* , vol. 2, 1415-1421.

56. Major J.J., Pierson T.C. (1992). "Debris flow rheology: Experimental analysis of finegrained slurries", *Water Resources Research*, vol. 28, 841-857.

57. Major J.J., Iverson R.M. (1999). "Debris-flow deposition: effect of pore-fluid pressure and friction concentrated at flow margins", *Geol. Soc. Am. Bull.*, vol.111, no. 9, 1424-1434.

58. Marr J. G., Harff P. A., Shanmugam G., Parker G. (2001). "Experiments on subaqueous sandy gravity flows: the role of clay and water content in flow dynamics and depositional structures", *Geological Society of America Bulletin*, vol. 113, 1377-1386.

59. McGregor B. A., Bennett R. H., Lambert D. N., (1979). "Bottom processes, morphology and geotechnical properties of the continental slope south of Baltimore Canyon", *Applied Ocean Research*, vol. 1, 177–187.

60. Mohrig D., Whipple K. X., Hondzo M., Ellis C., Parker G. (1998). "Hydroplaning of subaqueous debris flow", *Geological Society of America Bulletin*, vol.110, no.3, 387-394.

61. Mohrig D., Marr J.G. (2003). "Constraining the efficiency of turbidity current generation from submarine debris flows and slides using laboratory experiments", *Marine and Petroleum Geology,* vol. 20, 883-899.

62. Morgenstern N.R. (1967). "Submarine slumping and the initiation of turbidity currents", *Marine Geotechnique* (Ed. A.F. Richards), University of Illinois press, 189–220.

63. Mutti E., Tinterri R., Benevelli G., Di Biase D., Cavanna G. (2003). "Deltaic, mixed and turbidite sedimentation of ancient foreland basins", *Marine and Petroleum Geology*, vol. 20, 733-755.

64. Nissen S. E., Haskell N. L., Steiner C. T., Coterill K. L. (1999). "Debris flow outrunner blocks, glide tracks, and pressure ridges identified in the Nigerian continental slope using 3-D seismic coherency", *Leading Edge*, vol. 18, no. 5, 595-599.

65. Nogueira J., Lecuona A., Rodríguez P.A. (1997). "Data validation, false vectors correction and derived magnitudes calculation on PIV data", *Measurement Science and Technology*, vol. 8, no. 12, 1493-1501.

66. Norem H., Locat J., Schieldrop B. (1990). "An approach to the physics and the modelling of submarine flowslides", *Marine Geotechnology*, vol. 9, 93-111.

67. O'Brien J. S, Julien P. Y. (1988). "Laboratory analysis of mudflow properties", *J. Hydrol. Eng*., vol. 114, 877-887.

68. Parker G. (2000). "Hydroplaning outrunner blocks from auto-acephalated subaqueous debris flows and landslides", *Eos Trans. AGU*, vol. 81, 48 (Fall Meeting). Suppl., Abstract OS51D-08.

69. Pouliquen O. (2004). "Velocity correlations in dense granular flows", *Phys. Rev. Lett.*, vol. 93, 248001.

70. Pierson T.C., Costa J.E. (1987). "A rheological classification of subaerial sediment-water flows", *Debris flows/avalanches: Geological Society of America Reviews in Engineering Geology*, vol. 7, 1-12.

71. Prior D.B., Coleman J.M. (1979). "Submarine landslides Geometry and nomenclature", *Zeitschrift fur Geomorphologie*, vol. 23, 415-426.

72. Prior D. B., Bornhold B. D., Johns M. W. (1984). "Depositional characteristics of a submarine debris flow", *J. Geol.,* 92, 707-727.

73. Raffel M., Willert C., Kompenhans J. (1998), *Particle image velocimetry - a practical guide*, Springer-Verlag Berlin Heidelberg.

74. Ravenne C., Beghin P. (1983). "Apport des experiences en canal a l'interpretation sedimentologique des depots de cones detritiques sous-marine", Reveu de L'IFP, vol. 38, no. 3, 279-297.

75. Savage S.B., Dai R. (1992). "Some aspects of bounded and unbounded shear flows of granular materials", *Advances in Micromechanics of Granular Materials*, Elsevier, Amsterdam.

76. Shanmugam G. (1996). "High-density turbidity currents: are they sandy debris flows?", *J. Sediment. Res.* Vol. 66, no.1, 2-10.

77. Schlichting H. (1968). *Boundary-Layer Theory*, McGraw-Hill Book Co. New York.

78. Schwab W.C., Lee H.J., Twichell D.C., Locat J., Nelson C.H., McArthur W.G., Kenyon N.H. (1996). "Sediment mass flow processes on a depositional lobe, outer Mississippi Fan", *Journal of Sedimentary Research*, vol. 66, 916-927.

79. Spinewine B., Chapar H., Larcher M., Zech Y. (2003). “Three-dimensiona Voronoi imaging methods for the measurement of near-wall particulate flows”, *Exp Fluids*, vol. 34, 227-241.

80. Sveen J.K., Cowen E. A. (2003). "Quantitative imaging techniques and their application to wavy flows", *PIV and Water Waves*, World Scientific.

81. Sveen. J. K. (2004). “An introduction to MatPIV”, Eprint no. 2, Department of Mathematics, University of Oslo.

82. Takahashi T. (1991). *Debris flow*, IAHR Monograph series. Balkema, Rotterdam.

83. Toniolo H., Harff P. A., Marr J. G., Paola C., Parker G. (2004). “Experiments on reworking by successive unconfined subaqueous and subaerial muddy debris flows”, *J. Hydraul. Eng.*, vol. 130, no.1, 38-48.

84. Tyrach J. (2000). *Rheologische charaktersierung von zementaren Baustoffsystemen*, PhD Thesis, Fakultat der Univ. Erlangen-nurnberg, Erlangen (in German).

85. Press W.H., Teukolsky S.A., Vetterling W.T., Flannery B.P. (1992). *Numerical Recipes in C: the art of scientific computing*, Cambridge University Press.

86. Wan Z., Wang, Z. (1994). *Hyperconcentrated flow*, IAHR monograph series, Balkema, Rotterdam, The Netherlands.

87. Wesser 0 . E. (1977). “Deep-water oil sand reservoirs - ancient case histories and modern concepts”, *AAPG Continuing Education Course Notes* Series 6.

88. Westerweel J. (1997). “Fundamentals of digital particle image velocimetry”, *Meas. Sci. Technol*. vol. 8, 1379-1392.

89. Westerweel J. (1993). *Digital particle image velocimetry: theory and application*, Ph.D. Dissertation, University Press, Delft.

90. Westerweel J., (1994). “Efficient detection of spurious vectors in particle image velocimetry data”, *Exp. in Fluids*, vol. 16, 236-247.

91. Wildemuth C.R., Williams M.C. (1985). “A new interpretation of viscosity and yield stress in dense slurries-coal and other irregular particles”, *Rheologica Acta,* vol.24. 75–91.

Acknowledgements

This work was carried out as part of a project funded by the VISTA, the cooperation between The Norwegian Academy of Science and Statoil, project 6249. Additional funds were also provided by International Centre for Geohazards (ICG).

The first person I would like to thank is my advisor Anders for his confidence in me and his enthusiasm.

I thank professor Paolo Ghilardi and professor Luigi Natale for the daily discussions and for the freedom they gave me in conducting this research.

I would like to thank the staff at the St. Anthony Falls Laboratory, in particular Jeff and Ben, and the ICG researchers for their technical as well as their scientific support.

Takk! Hedda, Dieter, Fabio and Peter for the fruitful discussion and for the unforgivable adventures I had in Norway with you.

A travel is easier when you are not alone… Thank you Alice, Carla, Ga, Gauss, and Simon ("the clEb+2.95"), Cecco, Jenny, Zampo, Ful and all my friend *ad Graja*, Luca, Mat, Sara and Roberto (my family in the Mid West), Massi and Francesco (the Flow-Ing), Roger, Fede, Chiara, Joanna, Boti, Stefano, Carla and all the other guys of the Department of Hydraulics Engineering of the University of Pavia.

A special thank is due to Beatrice, my irrational and indispensable counterpart.

This thesis is finally dedicated to my mother Rosanna and my father Franco, for their support, advice and patience.

Appendix A

St. Anthony Falls Laboratory

St. Anthony Falls Laboratory (SAFL) is part of the University of Minnesota. The laboratory was established in 1938 mainly through the efforts and dedication of Lorenz G. Straub, its founder and first director. The structure is located on Hennepin Island at the head of St. Anthony Falls in the heart of Minneapolis. Improvements and expansions have evolved the building into five floors, two of which are above the headwater pool of the Mississippi River. The laboratory is designed to operate by diversion of water from the Mississippi River headpool. This arrangement is unique in that virtually all of the laboratory space for experimental purposes is below the headwater level of the river in order to use the natural power of the falls.

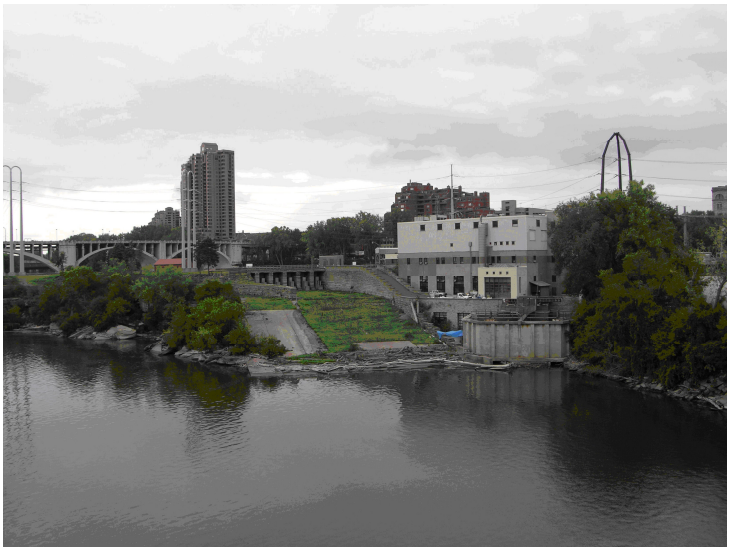

Figure A.1 View of the Saint Anthony Falls Lab.

Researchers at SAFL have been developing solutions to the major problems in hydraulic engineering and water resources for well over 60 years. Early research included model studies of some of the world's largest engineering feats of the twentieth century, such as Mangla Dam in West Pakistan, Priest Rapids and Wanapum Dams on the Columbia River and Guri Dam in Venezuela.

Appendix B

The ball rheometer system

The ball rheometer system (hence referred as BRS) consists of a cylindrical container with radius *Rs* = 57.5 mm and height *Hs* = 48 mm. An sample fluid of 0.5 l volume was placed in the container. An eccentrically rotating sphere with a given diameter *D* (*D*=8, 12 or 15 mm) fixed on to a 0.6 mm thin holder was dragged through the sample with a prescribed angular velocity *w* (Figure B.1).

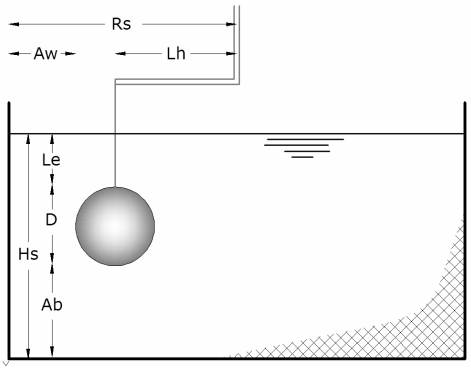

Figure B.1 Scheme of the ball rheometer system.

According to Tyrach (2000) a linear relationship can be derived between the shear stress τ and the torque M as well as between the shear rate and the angular velocity w for a sphere moving in a laminar flow field, assuming the validity of the Stokes equations (Clif et al., 1978).

The general resistance formula for a sphere dragged into a fluid is (Eq.[B.1]):

$$F = C_D \frac{\rho v^2}{2} \left(\frac{D}{2} \right)^2 \pi \qquad [B.1]$$

in which F is the drag force on the sphere and C_D is the drag coefficient (Eq.[B.2]).

$$C_D = \frac{24}{\mathrm{Re}} \qquad [B.2]$$

The Reynolds number Re in equation [B.2] is defined as ([B.3]):

$$\mathrm{Re} = \frac{v D \rho}{\mu} \qquad [B.3]$$

where v is the sphere velocity, D is the sphere diameter, r is the fluid density and m the dynamic viscosity of the fluid. Equation [B.1] on substitution of equations [B.2] and [B.3] yields an alternative expression of the Stokes equations as follows:

$$F = 3\pi v \eta D \qquad [B.4]$$

The torque M of the BMS is then expressed as (Eq [B.5]):

$$M = 3\pi \eta \omega D L_h^2 \qquad [B.5]$$

Due to the self-rotation of the sphere an additional torque M_2 is generated (Flügge,1963) as (Eq.[B.6]):

$$M_2 = \pi\eta\omega D^3 \qquad [B.6]$$

The viscosity for a Newtonian fluid $\mu = \tau/\dot{\gamma}$ can be derived from equations [B.5] and [B.6].

$$\tau = \frac{\dot{\gamma}}{\pi\omega} \cdot \frac{1}{\left(3DL_h^2 + D^3\right)} \cdot M \qquad [B.7]$$

Tytach (2000) assumed a linear relationship between the shear rate $\dot{\gamma}$ and the angular velocity ω (Eq. [B.8]) and therefore between τ and M (Eq.[B.9]).

$$\dot{\gamma} = K_{\dot{\gamma}} \cdot \omega \qquad [B.8]$$

$$\tau = K_{\tau} \cdot M \qquad [B.9]$$

where:

$$K_{\tau} = \frac{K_{\dot{\gamma}}}{\left[\pi\left(3DL_h^2 + D^3\right)\right]} \qquad [B.10]$$

BMS is based on Stokes equations for laminar flow around a sphere which were originally derived for unconfined Newtonian fluids. However, the BMS is actually applied to Newtonian and non-Newtonian fluids in a confined container. As a first approximation the effect of the container boundaries can be considered merging into the constants $K_{\dot{\gamma}}$ and K_{τ}.